Experimental and Numerical Investigations of the Flow Development over Cylinders with Stepwise Discontinuities in Diameter

by

Christopher R. Morton

A thesis
presented to the University of Waterloo
in fulfillment of the
thesis requirement for the degree of
Master of Applied Science
in
Mechanical Engineering

Waterloo, Ontario, Canada, 2010

I hereby declare that I am the sole author of this thesis. This is a true copy of the thesis, including any final revisions required from my examiners.

I understand that my thesis may be made electronically available to the public.

Abstract

Flow past circular cylinders with stepwise discontinuities in diameter was investigated experimentally and numerically for the diameter ratio D/d = 2 and three Reynolds numbers, Re_D = 150, 300, and 1050. The investigation was focused on the vortex shedding phenomena occurring in the wake of the cylinders.

In the first series of experimental and numerical studies, the flow development past a single step cylinder was investigated. The single step cylinder model is comprised of a small diameter cylinder (d) attached coaxially to a large diameter cylinder (D). The results show that three distinct spanwise vortex cells form in the step cylinder wake: a single vortex shedding cell in the wake of the small cylinder (the S-cell) and two vortex shedding cells in the wake of the large cylinder, one in the region downstream of the step (the N-cell) and the other away from the step (the L-cell). Due to the differences in vortex shedding frequencies between the three cells, complex vortex connections occur in two vortex-interaction regions located between the adjacent cells. The region at the boundary between the S-cell and the N-cell is relatively narrow and its spanwise extent does not fluctuate significantly. In this region, vortex dislocations manifested as half-loop connections between two S-cell vortices of opposite sign. In contrast, the region at the boundary between the N-cell and the L-cell exhibits a transient behavior, with large scale vortex dislocations causing cyclic variation in the extent of N-cell vortices. For Re_D = 300 and 1050, small scale streamwise vortices forming in the wake complicate the vortex dynamics within the adjacent S-cell and L-cell. There is no significant Reynolds number effect on the average spanwise extent of the vortex cells and the two transition regions between neighboring cells. Finally, formation of N-cell vortices is linked to downwash fluctuations near the step.

The flow development past a dual step cylinder was studied experimentally for Re_D = 1050. The dual step cylinder model is comprised of a small diameter cylinder (d) and a large diameter cylinder (D) mounted at the mid-span of the small cylinder. The experiments were completed for a range of large cylinder aspect ratios $0.2 \leq L/D \leq 17$. The flow development is highly dependent on the aspect ratio of the large cylinder, L/D. The results identify four distinct flow regimes: (i) for L/D = 17, three vortex shedding cells form in the wake of the large cylinder, one central cell and two cells of lower frequency extending over about 4.5D from the large cylinder ends, (ii) for $7 < L/D \leq 14$, a single vortex shedding cell forms in the wake of the large cylinder, whose shedding frequency decreases with decreasing L/D, (iii) for $2 \leq L/D \leq 7$, vortex shedding in the wake of the large cylinder is highly three-dimensional, with vortices deforming in the near wake, (iv) for $0.2 \leq L/D \leq 1$, only small cylinder vortices are shed in the wake and can form vortex connections across the wake of the large cylinder.

Acknowledgments

I would like to thank my supervisor, Professor Serhiy Yarusevych. Your expertise and dedication have been invaluable.

I appreciate all the help the machine shop personnel provided in the manufacturing of turbulence reducing screens, and endplates.

I would also like to thank my fellow graduate students, specifically, Sina Kheirkhah, Ryan Gerakopulos, Mike Bishop, Mike Boutilier, and Stephen Orlando, thank you for always being available to lend a helping hand.

I am thankful to Professor Ignacio Carvajal Mariscal, for his aid and expertise through the first year of my graduate studies.

Finally, thank you to the Natural Sciences and Engineering Research Council, Babcock and Wilcox Canada, and the University of Waterloo for their financial support required for my research.

Table of Contents

List of Figures

List of Tables

Nomenclature

CFL	Courant Friedrichs Lewy number
D	large cylinder diameter [mm]
d	small cylinder diameter [mm]
dx, dy, dz	LDV measurement volume dimensions
E_{uu}	normalized energy spectrum of u
E_{vv}	normalized energy spectrum of v
E_{ww}	normalized energy spectrum of w
f	vortex shedding frequency [Hz]
f_{EL}	vortex shedding frequency of the EL-cell [Hz]
f_{ES}	vortex shedding frequency of the ES-cell [Hz]
f_L	vortex shedding frequency of the L-cell [Hz]
f_N	vortex shedding frequency of the N-cell [Hz]
f_{N1}	vortex shedding frequency of the N1-cell [Hz]
f_{N2}	vortex shedding frequency of the N2-cell [Hz]
f_S	vortex shedding frequency of the S-cell [Hz]
f_{S1}	vortex shedding frequency of the S1-cell [Hz]
f_{S2}	vortex shedding frequency of the S2-cell [Hz]
L	cylinder length [mm]
MeanConf	95% confidence limit for mean velocity
N	number of samples
p	pressure [Pa]
Q	second invariant of the velocity gradient tensor
r	mesh refinement factor
Re_D	Reynolds number based on cylinder diameter, UD/ν
Re_d	Reynolds number based on small cylinder, Ud/ν
RMS	Root Mean Square
St	Strouhal number, fd/U
t	experiment or simulation time [s]
t*	dimensionless time, tf_S
T	data acquisition period

T_N	N-cell cycle period, $1/(f_L-f_N)$
T_u	turbulence intensity, 100u'/U
U	free stream velocity [mm/s]
u	streamwise velocity [mm/s]
$\bar{u}$	streamwise mean velocity [mm/s]
u'	RMS of streamwise velocity [mm/s]
V	DC voltage
v	transverse velocity [mm/s]
$\bar{v}$	transverse mean velocity [mm/s]
v'	RMS of transverse velocity [mm/s]
W	power in watts
w	spanwise velocity [mm/s]
$\bar{w}$	spanwise mean velocity [mm/s]
w'	RMS of spanwise velocity [mm/s]
x-y cells	number of cells in planar x-y mesh
x, y, z	streamwise, transverse, and spanwise coordinates, respectively [mm]
Δf	frequency resolution of velocity spectra [Hz]
Δt	time step size in numerical simulations
Δz	spanwise extent of the uniform flow region
Δz cells	number of spanwise cells in the computational domain
β	screen open area ratio
ρ	density of water [kg/m^3]
θ	maximum angle of deflection of the cylinder models [°]
ν	kinematic viscosity of water [m^2/s]

1 Introduction

Cross-flow around cylindrical bodies is encountered in a variety of industrial applications, e.g., mechanical devices and civil structures, where understanding the flow development is often of critical importance in engineering design. Thus, it is not surprising that the flow over cylindrical structures has been studied extensively over the past several decades, e.g., Berger & Willie (1972), Gerrard (1978), Roshko (1993).

The flow around a circular cylinder involves the formation and development of a boundary layer, a separated shear layer, and a wake. Figure 1.1 shows a conceptual sketch of the flow past a circular cylinder. As fluid approaches the cylindrical body, the fluid is diverted around the cylinder, and boundary layers develop on both the upper and the lower surfaces of the body (Fig. 1.1). The presence of an adverse pressure gradient causes the boundary layer to separate from the cylinder surface (Fig. 1.1), forming a separated shear layer. The shear layers formed on the upper and lower surfaces roll-up into vortices behind the cylinder. The process is periodic; vortices are shed from both sides of the cylinder in an alternating fashion. The continuous pattern of vortex shedding forms what is known as a vortex street in the cylinder wake. For the case of a uniform cross-flow over a uniform circular cylinder, vortices are shed at a nearly constant frequency (f), which is commonly expressed in non-dimensional form as the Strouhal number, $St = fD/U$.

The alternating shedding of vortices exerts oscillating forces on the body, which is the principal reason for its significance in engineering design. As a defining feature of the overall flow development, vortex shedding in the wake of a uniform circular cylinder has been the topic of hundreds of investigations (e.g., Gerrard, 1978; Williamson, 1996). Such investigations have identified how the vortex shedding characteristics change with Reynolds

number ($Re_D = \rho UD/\mu$), cylinder length (L), cylinder roughness, flow conditions, and other parameters.

In contrast, there are far fewer investigations on vortex shedding from more complex cylindrical geometries (e.g., tapered cylinders, cantilevered cylinders, cylinders with discontinuities in diameter, or cylinders with a non-circular cross-section). These geometries are common in many applications, e.g., off-shore oil risers, bridge supports, heat exchangers, towers. However, due to the lack of investigations for these geometries, the flow development is not fully understood.

The geometry of interest in this study is a circular cylinder with discontinuities in its diameter along the cylinder span (Fig. 1.2), which is common in such engineering applications as heat exchangers and airport control towers. When immersed in a uniform flow, vortex shedding is observed in the cylinder wake. However, the frequency of vortex shedding varies along the cylinder span, so that cells of vortices associated with a constant shedding frequency form in the wake. For example, in the wake of a single step cylinder (Fig. 1.2a), three vortex shedding cells may develop across the span (Dunn & Tavoularis, 2006). Previous experimental studies of the flow over single step cylinders, e.g., Dunn & Tavoularis (2006), Lewis & Gharib (1992), Norberg (1992), have provided insight into the vortex shedding and vortex dynamics in the wake of a single step cylinder, but the mechanism behind how the cells form and how they interact is still unknown. It should be noted that there have been no comprehensive experimental or numerical investigations completed on circular cylinders with multiple discontinuities in diameter (Fig. 1.2b).

This investigation is motivated by the need for insight into vortex shedding and vortex interactions occurring in the wakes of uniform cylinders with stepwise discontinuities in

diameter. The main objective of the thesis is to investigate the effects of the cylinder geometry as well as the Reynolds number on the flow development past (i) a single step cylinder (Fig. 1.2a), and (ii) a dual step cylinder (Fig. 1.2b). Both experimental and numerical techniques are utilized to develop an understanding of vortex shedding and associated phenomena occurring in the wake.

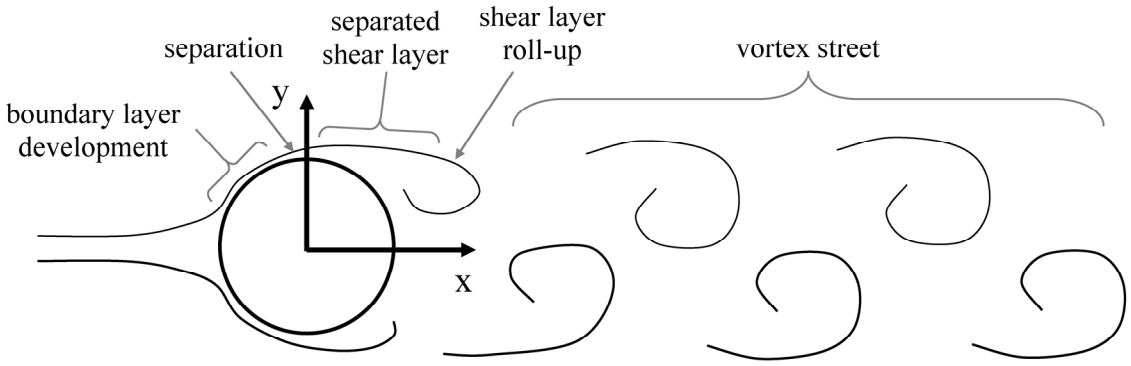

Figure 1.1 Vortex shedding from a circular cylinder.

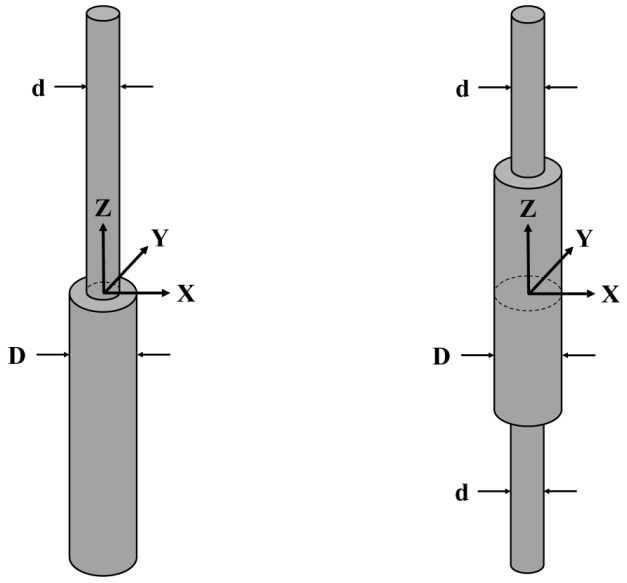

(a) (b)

Figure 1.2 Cylindrical geometries with discontinuities in diameter: (a) Single Step Cylinder, (b) Dual Step Cylinder.

2 Literature Review

The purpose of this section is to provide background on the flow topology in the wakes of cylindrical geometries which produce vortex shedding. The flows discussed here are closely related to the main topic of this investigation, namely, the flow development over circular cylinders with discontinuities in diameter. It is instructive to first focus on a uniform circular cylinder.

2.1 Vortex Shedding in the Wake of Uniform Circular Cylinders

Hundreds of research investigations on the flow over uniform circular cylinders have been completed over the past century (e.g., Weiselberger, 1921; Roshko, 1954; Gerrard, 1978; Williamson, 1996; Norberg, 2003). A review of the flow development is given by Williamson (1996). In his review, distinct flow regimes are identified based on the Reynolds number (e.g., Figs. 2.1a-c). As the Reynolds number approaches $Re_D \approx 50$, a global instability in the cylinder wake leads to a vortex shedding phenomenon (Williamson, 1996). As depicted in Fig. 2.1a, spanwise oriented vortices are shed parallel to the cylinder axis in a single cell of constant frequency. This type of vortex shedding is considered to be two dimensional, since the flow development is invariant in the spanwise direction. Vortex shedding remains two-dimensional for about $50 < Re_D < 190$. However, as the Reynolds number increases, a transition to Mode A vortex shedding takes place (Williamson, 1996). Mode A vortex shedding occurs for about $190 < Re_D < 240$ and is characterized by the deformation of spanwise vortices. The deformation of vortices causes the formation of streamwise vortex pairs, which appear in an organized fashion with a spanwise spacing of about 3-4 diameters (Fig. 2.1b). However, it has been reported that transition to turbulence

can occur in the far wake (Zdravkovich, 1997). The transition to Mode B vortex shedding occurs for $Re_D \approx 240$. This mode of shedding persists for Reynolds numbers up to about 1000 and is characterized by the formation of smaller scale streamwise vortices in the wake. These vortices have a spanwise spacing on the order of one cylinder diameter (Fig. 2.1c), significantly smaller than that found in Mode A shedding. As the Reynolds number increases from 240 to 1000, the formation and arrangement of the streamwise vortices becomes less organized, and the laminar-to-turbulent transition point moves into the near wake of the circular cylinder. For $Re_D \approx 1000$, the laminar shear layers forming due to boundary layer separation on the upper and lower surfaces of the cylinder become unstable and undergo transition to turbulence (Williamson, 1996). With increasing Reynolds number, the transition point moves upstream but remains in the shear layer for about $1000 \leq Re_D \leq 200{,}000$, which encompasses a Reynolds number range common to a large number of industrial flows. In the range of about $200{,}000 < Re_D < 1{,}000{,}000$ turbulent transition remains in the separated shear layer; however, it causes shear layer re-attachment and the formation of a separation bubble. The re-attached turbulent boundary layer then separates near the aft of the cylinder. For about $1{,}000{,}000 < Re_D < 6{,}000{,}000$, the turbulent transition occurs near the point of laminar separation, causing an irregular bursting of the separation bubbles and an absence of periodic vortex shedding. Periodic shedding remains for $Re_D \approx 6{,}000{,}000$ and beyond, when the laminar boundary layers on the surface of the cylinder undergo turbulent transition prior to flow separation.

Complimenting experimental studies, numerical investigations have modeled the flow past uniform circular cylinders and the associated wake vortex shedding phenomenon. In

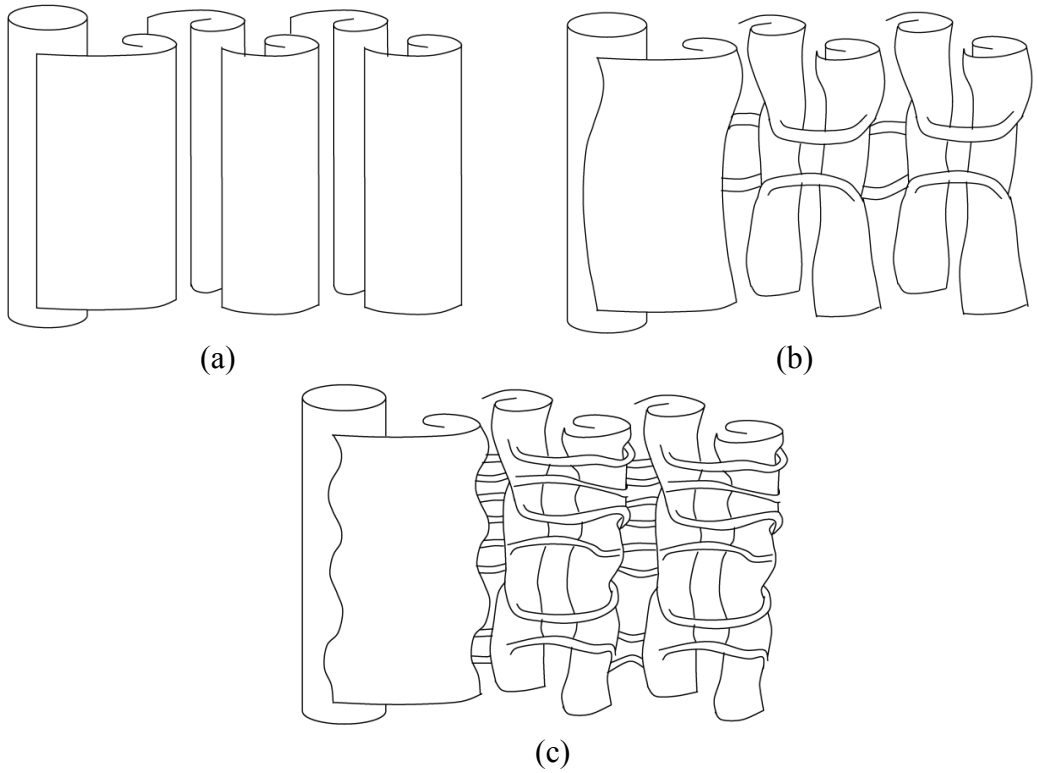

Figure 2.1 Selected vortex shedding regimes in the wake of a uniform circular cylinder: (a) Laminar vortex shedding, $50 < Re_D < 190$, (b) Mode A vortex shedding, $190 < Re_D < 240$, (c) Mode B vortex shedding, $240 < Re_D < 1000$.

particular, Direct Numerical Simulations (DNS) have been used to model the flow development for relatively low Reynolds numbers (e.g., Zhang et al., 1995; Persillion & Braza, 1998). DNS predictions of the onset of vortex shedding, as well as the transition to Mode A and Mode B vortex shedding are shown to be in excellent agreement with experimental results. Due to the computational demands of DNS, few studies have been completed for Reynolds numbers within the shear layer transition regime (e.g., Wissink & Rodi, 2008). For higher Reynolds numbers, most numerical investigations of the flow past uniform circular cylinders are performed with alternative simulation methods, for example, Large Eddy Simulation (LES) and Reynolds Averaged Navier Stokes (RANS) simulation (Xiyun & Guocan, 2002; Breuer, 1998; Singh & Mittal, 2005). Both RANS and LES results

are able to reproduce many of the key aspects of the flow development, but generally deviate from experimental results due to modeling assumptions.

Vortex shedding characteristics can be affected by blockage, flow uniformity, cylinder span, and cylinder end conditions (e.g., Okamoto & Takeuchi, 1975; Balasubramanian et al., 1998; West & Fox, 1990; Gerich & Eckelmann, 1982). In the context of the present investigation, the most important factors are the cylinder end conditions and the cylinder aspect ratio. These factors can influence the vortex shedding in the wake and are discussed in detail in the following section.

2.1.1 Influence of end conditions and aspect ratio (L/D) on vortex shedding from a uniform circular cylinder

The end conditions of a uniform circular cylinder in a uniform cross-flow can affect the flow development across the entire span of the cylinder (e.g., Prasad & Williamson, 1997; West & Fox, 1990). However, with certain end conditions, adverse effects can be minimized to only a few cylinder diameters from each end. This is commonly done by mounting circular or rectangular thin plates, otherwise known as endplates, to the cylinder ends (Fig. 2.2).

With the use of endplates at cylinder boundaries, the flow field is not uniform across the entire cylinder span. Boundary layers will develop along the endplate surfaces and result in reduced flow velocity near the cylinder ends (Fig. 2.2). The convective velocity of the shed vortices near the cylinder ends is also reduced leading to a decrease in the frequency of vortex shedding when compared to that at the mid-span. Thus, it can be expected that distinct vortex shedding cells will develop near the ends of a large aspect ratio circular cylinder mounted between two identical endplates. Figure 2.2 shows two end cells of low frequency

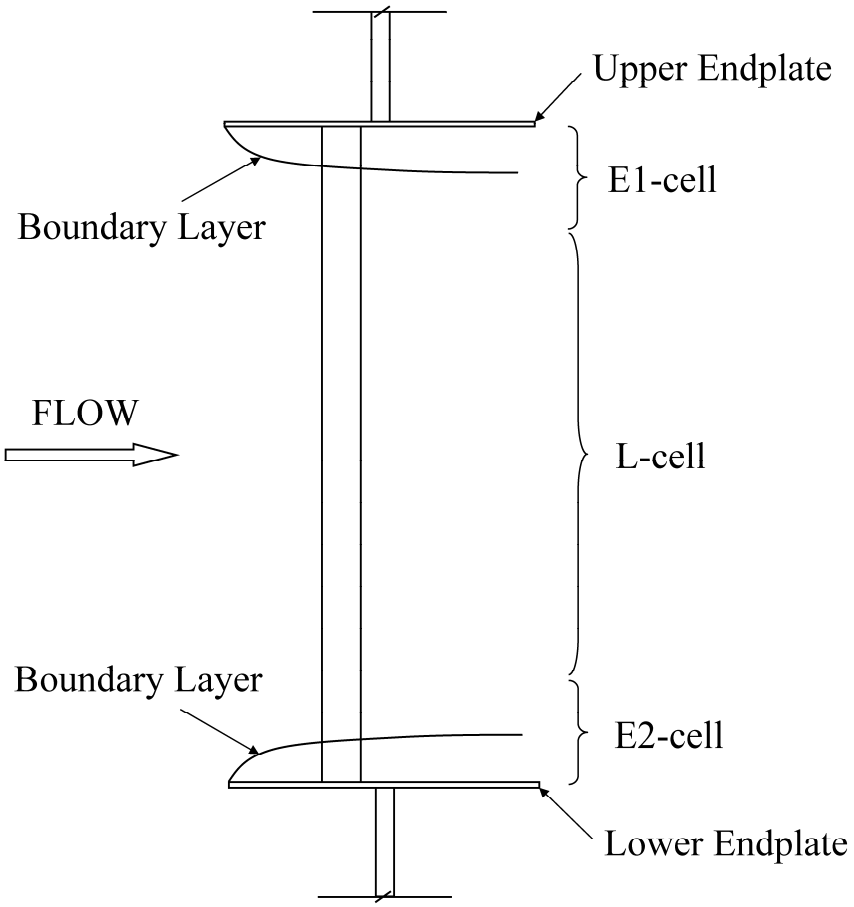

Figure 2.2 Flow past a uniform circular cylinder mounted between two identical endplates.

(E1 and E2) forming near the endplates, and one central cell (L) that is representative of flow past an infinite cylinder.

The spanwise size of the end cells and the central cell has been shown to be dependent on the endplate dimensions and the aspect ratio of the cylinder (e.g., Stansby, 1974; Mair & Stansby, 1975; West & Fox, 1990). Pioneering work on the use of endplates was completed by Stansby (1974) and Mair & Stansby (1975). Stansby (1974) showed that for endplates of a fixed size, the spanwise size of the end cells depends on the mounting location of the cylinder on the endplates. Stansby (1974) found an optimum cylinder position which resulted

in the smallest possible end cells, however, the effect of cylinder aspect ratio was not investigated.

West & Fox (1990) investigated the effect of cylinder aspect ratio on the flow development past a uniform cylinder mounted between endplates. West and Fox used the same endplate size and installed the cylinder between the endplates at the same location as that used by Stansby (1974). For aspect ratios greater than L/D ≈ 7, West & Fox (1990) suggest that each of the two end cells forming near the cylinder boundaries has a spanwise extent of about 3.5D. Hence, a central cell exists near the mid-span with a span of about (L/D – 7). West & Fox (1990) recommend that, to achieve nominally two-dimensional vortex shedding conditions at the mid-span of a uniform circular cylinder, the cylinder aspect ratio must be significantly larger than 7.

2.2 Vortex Shedding in the Wake of Non-Uniform Cylinders

In contrast with a significant number of extensive investigations on the flow development over a uniform circular cylinder, far fewer studies have been performed on more complex cylindrical geometries. Despite differences in geometries, it has been shown that, in uniform flows, spanwise vortices are shed in constant-frequency cells in the wakes of tapered, free-end, and step cylinders (Fig. 2.4a-c). The arrangement of the vortex cells and wake vortex interactions, however, have been shown to depend significantly on the geometry and Reynolds number.

2.2.1 Linearly Tapered Cylinders

The tapered cylinder geometry (Fig. 2.3a) causes vortex shedding to occur at an angle to the cylinder axis. Multiple spanwise vortex cells form in the wake, each associated with a

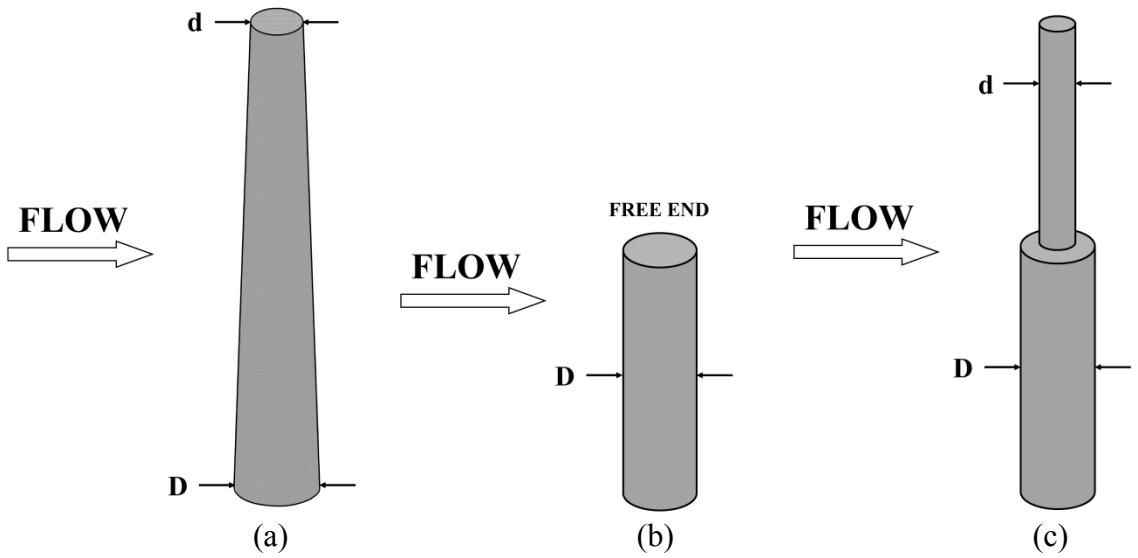

Figure 2.3 (a) Tapered, (b) Free-end, and (c) Step-cylinder geometries.

distinct shedding frequency (e.g., Piccirillo & Van Atta, 1993). The shedding frequency of each cell is lower than that expected for a uniform cylinder with the diameter equal to the local diameter of a tapered cylinder at the mid-span of the spanwise vortex cell. At the boundaries between adjacent cells, vortex interactions occur, involving vortex splitting and vortex dislocations (e.g., Piccirillo & Van Atta, 1993). As a result, velocity signals measured near the boundaries between vortex cells exhibit a low frequency modulation that is equal to the difference of vortex shedding frequencies of the adjacent cells (Gaster, 1969; Van Atta & Piccirillo, 1990). The spanwise extent of the vortex cells in the wake of a tapered cylinder has been found to increase with increasing local Reynolds number and increasing taper ratio (i.e., decreasing the amount of taper).

In addition to experimental investigations, several numerical studies have successfully modeled the flow development in the wake of a tapered cylinder, e.g., Noack et al. (1991), Valles et al. (2002), and Narasimhamurthy et al. (2009). The numerical results have reproduced the cellular vortex shedding pattern in the wake and have uncovered three-

dimensional shedding features similar to those observed for a uniform circular cylinder, e.g., small-scale streamwise vortices, vortex splitting, and vortex dislocations.

2.2.2 Cantilevered or Free-End Cylinders

Previous studies focused on the flow over cantilevered cylinders (Fig. 2.4b) have shown that the flow development is influenced primarily by the cylinder aspect ratio (L/D) and the Reynolds number (Re_D) (e.g., Farivar, 1981; Gerich & Eckelmann, 1982; Ayoub & Karamecheti, 1982; Ko & Chan, 1984; Zdravkovich, 1989; Roh & Park, 2003). Uniform flow past large aspect ratio cantilevered cylinders, L/D ≥ 20-30, produces a minimum of three vortex shedding cells in the wake: one central cell, and two end cells forming near the cylinder boundaries (Gerich & Eckelmann, 1982). Zdravkovich (1989) attributes the end cell formation near the free-end to downwash, which may affect the vortex formation. Smaller aspect ratio cantilevered cylinders (6<L/D<20) produce a single vortex shedding cell across the cylinder span (Gerich & Eckelmann, 1982). The shedding frequency of the single cell decreases with decreasing aspect ratio. The alternate shedding of vortices stops completely at about L/D ≈ 6 and is replaced by a symmetric shedding of vortices (Okamoto & Yagita, 1973). The symmetric shedding was confirmed through both flow visualization and experimental measurements for L/D as small as 1.5 (Sakamoto & Arie, 1983). It should be noted that the bounds of L/D values associated with the identified cellular shedding patterns have been shown to vary with Re_D (e.g., Farivar, 1981; Gerich & Eckelmann, 1982).

Numerical simulations of the flow past a cantilevered cylinder have been performed for various aspect ratios and Reynolds numbers and have reproduced the main features of the cellular vortex shedding (e.g., Afgan et al., 2007; Pattenden et al., 2007; Frohlich & Rodi, 2004).

2.2.3 Cylinders with Two Free Ends

Under laminar vortex shedding conditions, multiple vortex shedding cells have been shown to develop in the wake of a cylinder with two free ends for L/D > 20-30 (Inoue & Sakuragi, 2008; Norberg, 1994). Specifically, a central vortex shedding cell forms near the mid-span of the cylinder, and end cells of lower frequency form near each of the two free-ends. For 10 < L/D < 20-30, a single vortex shedding cell is observed in the wake. The shedding frequency of this single cell decreases with decreasing L/D and is less than that expected for a uniform circular cylinder of equivalent diameter. For L/D < 10, the flow development becomes dependent on the Reynolds number. For Reynolds numbers in the laminar vortex shedding regime for a uniform circular cylinder, a distorted three-dimensional vortex shedding is observed for 2 < L/D < 10 (Inoue & Sakuragi, 2008). For Reynolds numbers corresponding to the shear layer transition regime for a uniform circular cylinder, quasi-periodic vortex shedding is observed in the wake for 2 < L/D < 8 (Zdravkovich, 1989). In particular, vortex shedding is intermittent, with vortex shedding frequency varying with time. At smaller L/D in the laminar shedding regime, steady counter-rotating vortex pairs or the alternate shedding of counter-rotating vortex pairs is observed, with the type of shedding being dependent on the Reynolds number for 0.5 < L/D < 2, (Inoue & Sakuragi, 2008).

2.2.4 Single Step Cylinders

A single step cylinder consists of a large cylinder (diameter D) and a small cylinder (diameter d) joined co-axially (Fig. 2.3c). Thus, there is a discontinuity at the edge of the large cylinder where a step change in diameter occurs. For a single step cylinder, vortex shedding occurs in the wakes of the larger diameter cylinder (D) and the smaller diameter cylinder (d) and vortices interact in the wake region downstream of the step (e.g., Dunn &

Tavoularis, 2006; Lewis & Gharib, 1992). The flow development over a step cylinder is of particular interest in this study, as this relatively simple geometry allows modeling complex vortex interactions and is common in various engineering structures, e.g., towers and supporting struts. Lewis & Gharib (1992) showed that the flow development in the wake of a step cylinder is dependent primarily on the Reynolds number (Re_D) and the ratio of the large cylinder diameter (D) to the small cylinder diameter (d), referred to as the diameter ratio (D/d). Previous experimental studies, most relevant of which are listed in Table 1, suggest that due to a mismatch between the shedding frequencies of the small and the large cylinders, vortex interactions take place in the wake region downstream of the step. Ko, Leung, and Au (1982) identified such an interaction region of non-uniform shedding downstream of the step which was offset towards the large cylinder. Vortex interactions within this region were the topic of several subsequent investigations, e.g., Lewis & Gharib (1992), Norberg (1992), and Dunn & Tavoularis (2006). Lewis & Gharib (1992) identified two different modes of vortex shedding interaction, namely, the 'direct mode' and the 'indirect mode'. In the direct mode, the vortex interaction region is relatively narrow, with vortex connections occurring between vortices shed from the large and the small cylinders and vortex dislocations involving connections between vortices in the same cell (Fig. 2.5a). In the indirect mode, a distinct vortex shedding cell, different from the dominant vortex shedding cells in the wakes of the large and the small cylinders, forms within the interaction region (Lewis & Gharib, 1992) (Fig. 2.5b). The shedding frequency of this cell was found to be the lowest of the three cells. Complex vortex connections and vortex dislocations occur at the two cell boundaries, one located directly downstream of the step, and the other, offset to the large cylinder side. According to the results of Lewis & Gharib (1992), for $35 \leq Re_D \leq 200$, the indirect mode

vortex shedding occurs for diameter ratios (D/d) greater than 1.55. In the range of 1.25 < D/d < 1.55, the mode of vortex shedding is dependent on the Reynolds number; whereas, for D/d < 1.25, direct mode vortex shedding prevails for all Reynolds numbers studied by Lewis & Gharib (1992).

Adopting the terminology introduced by Dunn & Tavoularis (2006), three types of wake vortex shedding cells can be identified for indirect mode shedding in the wake of a step cylinder: (i) the S-cell – vortex shedding from the small cylinder; (ii) the L-cell – vortex shedding from the large cylinder; (iii) the N-cell – distinct vortex shedding in the region between the S-cell and the L-cell. Based on flow visualization results, Lewis & Gharib (1992) and Dunn & Tavoularis (2006) suggest that the N-cell is a cyclic phenomenon. That is, the formation of N-cell vortices interrupts periodically and then resumes after a few L-cell shedding cycles. However, the mechanism behind the N-cell formation and its cyclical nature remains unexplained. Lewis & Gharib (1992) have suggested that the frequency of occurrence of N-cell cycles is related to the growth rate of the N-cell, and the occurrence of a secondary instability, initiating the N-cell cycle. Dunn & Tavoularis (2006) suggest that the mechanism responsible for N-cell formation is related to that due to which the low frequency cell is believed to form near the end of a cantilevered cylinder (Zdravkovich et al., 1989). Specifically, Dunn & Tavoularis (2006) speculate that downwash past the step may lead to an increase in base pressure in the region near the step. This causes the vortex formation region to elongate and results in a lower shedding frequency.

Table 1 Previous experimental investigations of flow over step cylinders.

Study	Re_D	D/d
Ko, Leung, & Au (1982)	8×10^4	2
Yagita, Kojima, & Matsuzaki (1984)	8×10^2 - 10^4	1.25 - 5
Lewis & Gharib (1992)	67 - 200	1.14 - 1.76
Dunn & Tavoularis (2006)	62 - 1230	2
Norberg (1992)	3×10^3-13×10^3	1.25 - 2
Ko & Chan (1984, 1990, 1992)	8×10^4	1.33 - 2.78
Chua, Liu, & Chan (1998)	4.72×10^3	3

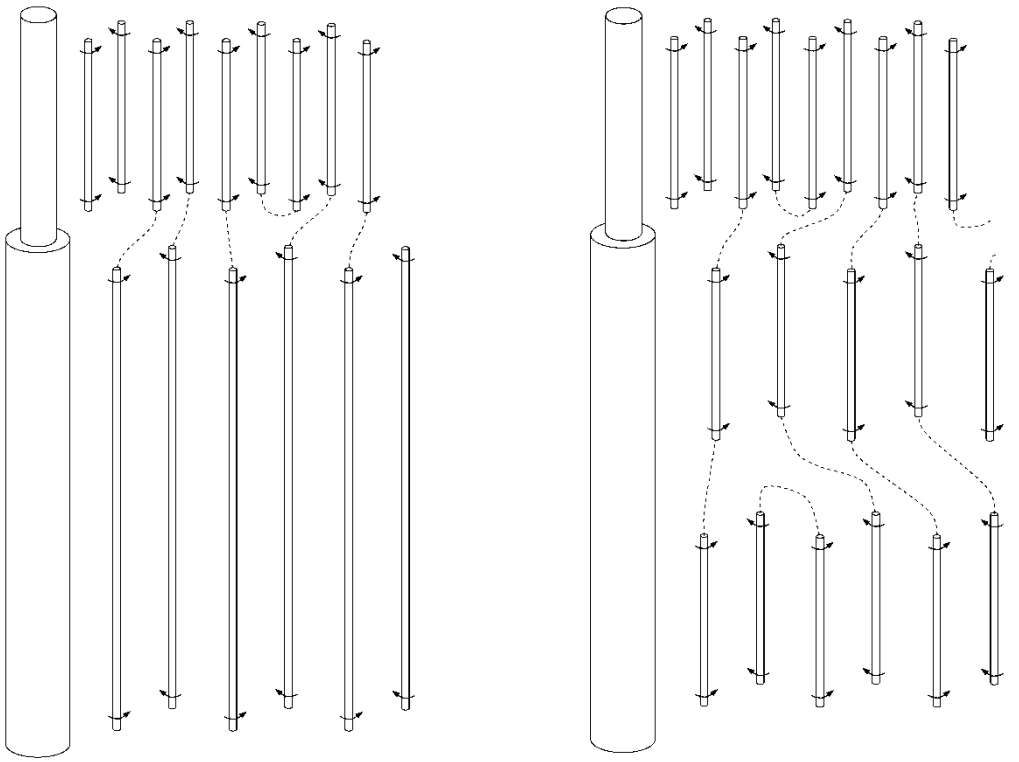

(a) (b)

Figure 2.4 Vortex shedding in the wake of a single step cylinder: (a) direct mode vortex shedding and (b) indirect mode vortex shedding. Dashed lines represent intricate vortex connections between spanwise vortices of the same sign.

2.2.5 Dual Step Cylinders

A dual step cylinder consists of two small cylinders (diameter d) attached co-axially to the ends of a large cylinder (diameter D). Thus, there are two discontinuities in diameter

along the span (Fig. 1.2b). To the best of the author's knowledge, a comprehensive study of the flow development over a dual step cylinder has not been completed to date. There are two experimental studies which involved a dual step cylinder. Williamson (1992) investigated the flow past dual step cylinders of small aspect ratio at Reynolds numbers pertaining to the laminar shedding regime. Nakamura & Igarashi (2008) investigated dual step cylinders of varying aspect ratio in the turbulent shedding regime.

Williamson (1992) used a dual step cylinder with D/d = 1.5 and L/D = 0.5 to investigate the formation and development of vortex dislocations. The presence of the larger cylinder (referred to as a ring in their study) caused the formation of periodic vortex dislocations on both sides of the large cylinder. The dislocations were synchronized only when the flow conditions on either side of the large cylinder were carefully matched (i.e., the shedding frequencies of the small cylinders were nearly identical). It can be inferred from the results that the frequency of dislocations and the influence of the dislocations on the wake development depend on the diameter ratio, D/d. In particular, under identical flow conditions, dual step cylinders with D/d = 1.1 & D/d = 1.5 induce vortex dislocations at a different frequency (Williamson, 1992).

In an effort to reduce the overall drag force, Nakamura & Igarashi (2008) attached multiple cylinders (diameter D) to a uniform cylinder (diameter d). The attached cylinders were referred to as rings in their study. Each ring was separated by a fixed spanwise distance. Nakamura & Igarashi (2008) varied the ring aspect ratio (L/D), the spanwise spacing between each ring, the diameter ratio (D/d), and Reynolds number (Re_d) to reduce the overall drag force. A range of parameters was determined for which the drag force was reduced by as much as 18% compared to a circular cylinder without rings. To aid in their analysis of the

flow development, Nakamura & Igarashi (2008) completed a flow visualization study. Their flow visualization indicates that the flow separation on the ring surfaces is delayed when compared to a uniform circular cylinder. The delayed separation was speculated to be associated with streamwise vortices which are generated at each of the step discontinuities in diameter.

3 Experimental Setup

3.1 University of Waterloo Water Flume Facility

All experiments were conducted in the University of Waterloo Water Flume Facility (Fig. 3.1). The flume has a 2.4 m long rectangular test section with a width of 1.2 m and a height of 1.0 m. The test section walls are made of 19 mm thick glass to allow optical access. The flume is supplied by an elevated tank, where a steady water level is maintained. At the exit of the flume, a perforated plate is installed to maintain the water level in the test section at 0.8m.

In the past, the facility was primarily used for modelling atmospheric boundary layer flows (e.g., Macdonald et al., 2002). Significant modifications and upgrades have been implemented to the facility to improve the flow uniformity and reduce turbulence intensity in the test section. A detailed description of all the modifications and upgrades is presented in Appendix A. Following the modifications and upgrades, the mean turbulence intensity in the test section was reduced from 3% to less than 1%, comparable to other research grade water flumes and water tunnels (e.g., Dunn, 2004; Morse & Williamson, 2006). In addition, the flow uniformity was improved from 17% to within 3%, with the deviation in the flow speed primarily attributable to a minor gradual increase of velocity with height.

Spectral analysis of free stream velocity data revealed low frequency oscillations in the velocity signal on the order of 0.1 Hz. These fluctuations did not have a significant impact on the vortex shedding (see Appendix D). To ensure that the LDV measurements included only particles that follow the mean flow, a technique proposed by Srikantaih & Coleman (1985)

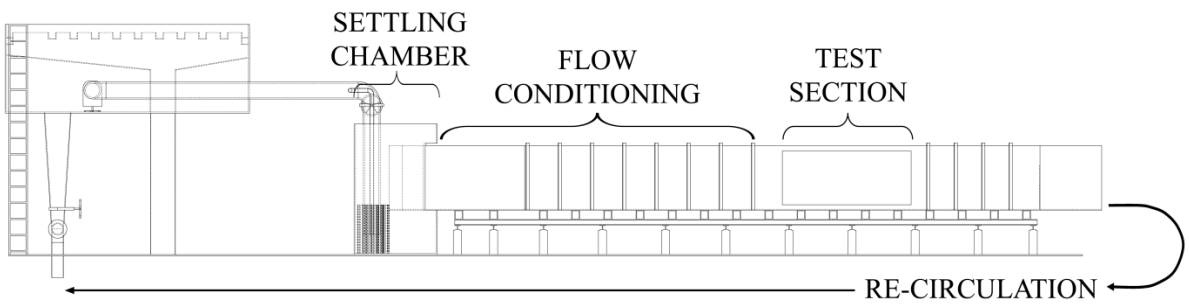

Figure 3.1 University of Waterloo Water Flume.

was employed to remove erroneous data. This causes less than 0.5% of the data to be removed and has no effect on the data interpretation (Srikantaih & Coleman, 1985).

3.2 Cylinder Mounting

A rigid support structure was built to enable cylinders to be mounted vertically in the test section (Fig. 3.2a). A simplified diagram of the cylinder model mounting arrangement is shown in Fig. 3.2b. The cylinders were positioned vertically, perpendicular to the water flow, with the alignment verified using a laser mounted on a high precision automated traverse to within 0.1°. The origin of the coordinate system is placed equidistant from each endplate on the axis of the cylinder model (Fig. 3.2b), with the x, y, and z coordinates corresponding to streamwise, transverse, and spanwise directions, respectively.

3.3 Models

Circular cylinders with single and dual step discontinuities in diameter were investigated. For both configurations, the smaller diameter cylinder (d) was made of stainless steel and the larger diameter cylinder (D) was made of aluminum. Several large diameter cylinders of different aspect ratios (L/D) were manufactured. Holes were bored through the center of each large cylinder to create a sliding fit over the stainless steel cylinder. The friction produced from the sliding fit was sufficient to hold the large cylinder in a fixed

position. In this way, single step cylinders and dual step cylinders of varying aspect ratio could be made using the same stainless steel small cylinder. All cylinders were sanded uniformly with 600 grit sand paper and finished with aluminum polish. All the model configurations investigated are detailed in Table 2.

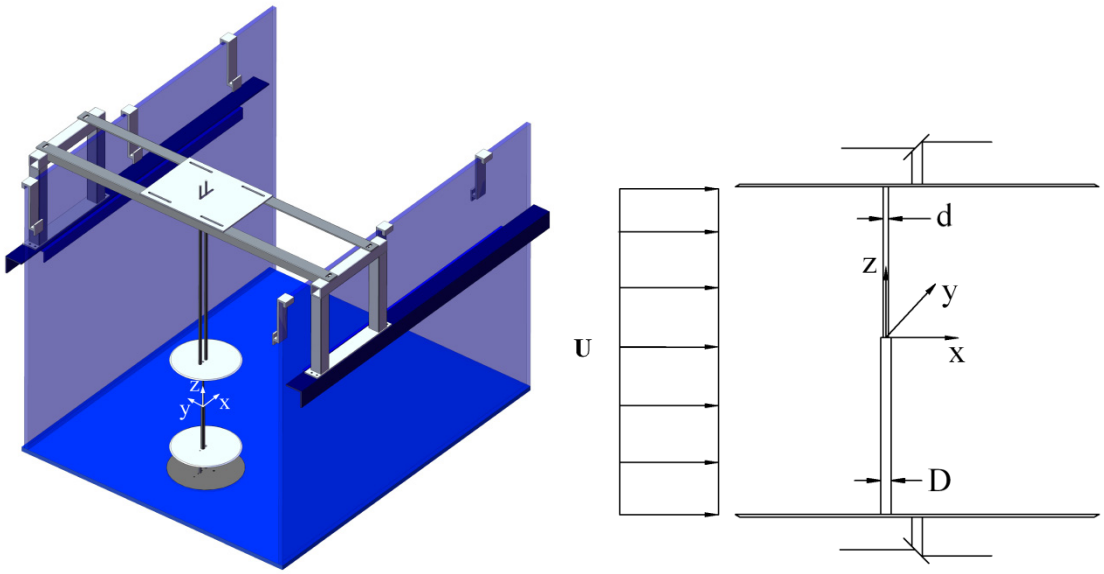

(a) (b)

Figure 3.2 Support structure and cylinder mounting within the test section: (a) assembly of test section, (b) simplified sketch.

Table 2 Cylinder model geometries under investigation. 'L/D' represents the aspect ratio of the large cylinder, whereas 'L/d' represents the aspect ratio of the small cylinder.

Configuration	Diameter (mm)	Aspect Ratio Investigated
Uniform Large Cylinder	D = 12.7	L/D = 33
Uniform Small Cylinder	d = 6.35	L/d = 66
Single Step Cylinder	D = 12.7 d = 6.35	L/D = 17 L/d = 32
Dual Step Cylinder	D = 12.7 d = 6.35	L/D = 0.2, 1, 2, 3, 5, 7, 10, 14, 17 L/d ≈ 33, 32, 31, 30, 28, 26, 23, 19, 16,

3.4 Endplates

Circular Lexan endplates, designed following recommendations by Mair & Stansby (1974), were fastened to the ends of each cylinder model (Fig. 3.2b) and positioned in the uniform region of the flow (Appendix A). The endplates have a diameter of 150mm and a 60^0 chamfered edge, similar to the endplates used by Dunn (2004) in his experimental investigation on single step cylinders. The water flow in the region between the endplates is considered to be nearly uniform and spans approximately $\Delta z = 450$mm (see Appendix A). Each model was attached to the endplate upstream of the endplate centerline, in accordance with the recommendations by Mair & Stansby (1975).

3.5 Flow visualization

Two flow visualization methods were utilized to visualize wake vortex shedding: hydrogen bubble technique, and planar Laser Induced Fluorescence (LIF). Both methods enabled the visualization of wake vortex shedding.

3.5.1 Hydrogen bubble technique

Hydrogen bubbles were produced along a thin (0.09 mm in diameter) stainless steel wire mounted approximately 0.2D upstream of the model along its entire span (Fig. 3.3), similar to the arrangement employed by Kappler et al. (2005) for a uniform circular cylinder. The flow was illuminated with a laser sheet positioned in either the x-y plane or the x-z plane. The size of the hydrogen bubbles and, hence, their buoyancy depend on the wire diameter and the applied voltage (Lian & Su, 1996). An experimental study was conducted to determine a range of DC voltage which produced a sheet of hydrogen bubbles with negligible buoyancy effects (see Appendix B). A DC voltage of less than about 40 V was found to produce a continuous sheet of bubbles that can be considered neutrally buoyant within the

flow region of interest. For all hydrogen bubble flow visualization experiments, a DC voltage of 30 V was used.

3.5.2 Laser Induced Fluorescence (LIF)

For planar LIF visualization, Rhodamine dye was injected from a 2.5 mm diameter probe placed approximately 20D upstream of the model axis (Fig. 3.3). In order to produce a stable dye jet, the dye injection speed was adjusted to match the free stream velocity. The probe position was adjustable so that dye could be injected at different locations along the models span. The Reynolds number based on probe diameter is about Re = 200. Therefore, vortex shedding is expected to occur in the wake of the probe. Thus, to reduce the effect of

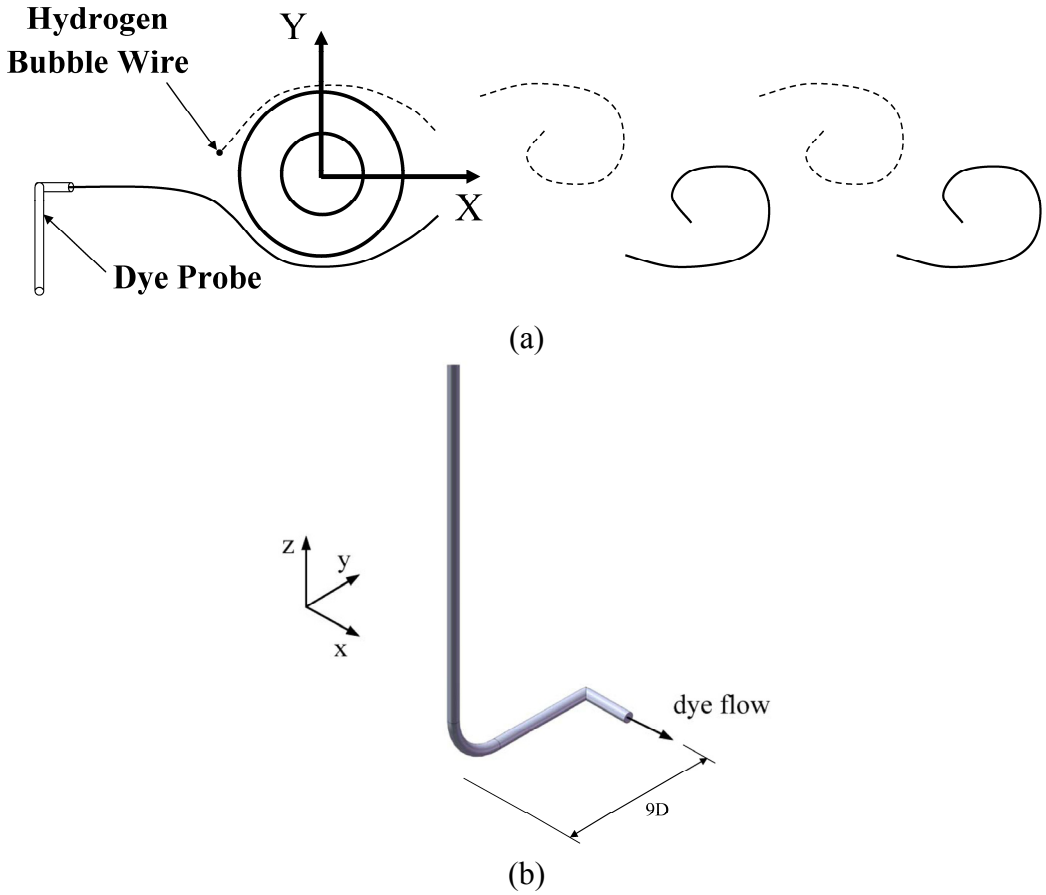

Figure 3.3 Flow visualization setup: (a) dye probe and hydrogen bubble wire arrangement, (b) dye probe design. The actual location of the dye probe is 20D upstream of the model axis.

the probe on the flow development, a bent probe was utilized (Fig. 3.3b). The end of the probe is aligned with the wake centerline as shown in Fig. 3.3.

3.5.3 Flow illumination and imaging

A laser beam was generated by a 2 W continuous wave Argon-Ion laser, and passed through a Plano-concave cylindrical lens to generate a thin laser sheet. The laser sheet was used to illuminate the hydrogen bubbles and Rhodamine dye. The laser sheet was positioned to illuminate the flow in either the x-y or x-z planes.

For planar LIF visualization, the dye was illuminated with the laser sheet positioned in the x-y plane to visualize wake vortex shedding, and with the laser sheet positioned in the x-z plane to visualize flow near the step. When visualizing vortex shedding in the x-y plane, the dye injection and hydrogen bubble systems were used simultaneously (Fig. 3.3a). This allowed correlating the planar LIF images obtained in the x-y plane to the spanwise development of wake vortices monitored in the x-z plane. In addition, vortex cores were easier to identify in the planar images. For hydrogen bubble visualizations, spanwise vortices on one side of the wake were illuminated with the laser sheet positioned in the x-z plane at $y/D \approx 0.375$ or -0.375.

Flow visualization images were obtained with a Nikon D300 camera. The camera was controlled remotely. In addition, another camera was used to record videos simultaneously with sequences of still images to aid in the identification of periodic phenomena in the wake. The digital video recording was completed at a fixed frame rate of approximately 15 Hz.

3.6 Velocity measurements

A two component Dantec LDV system was used to measure the streamwise velocity component. The output of a 5 W Argon-Ion laser is split into four nearly equal intensity

beams (two blue at 488 nm, and two green at 514.5 nm). Two of the four beams (one blue and one green) are frequency-shifted by 40 Mhz to enable resolving flow direction in a measurement volume (Tavoularis, 2005). The four beams are transmitted through fibre optic cables to a laser probe. A 600 mm focal length lens is fixed to the end of the laser probe to allow measurements across at least half of the test section width. This lens results in a measurement volume size of approximately dx = 0.15 mm, dy = 1.24 mm, dz = 0.15 mm. The Doppler signals are analyzed by a burst processor (Dantec BSA F50), with a velocity resolution on the order of 7.5×10^{-3} mm/s. The uncertainty in the mean velocity was estimated to be within 0.45% (see Appendix C). The water used for the experiments contains natural seeding particles, which produce data acquisition rates in the range of 15-100 Hz. For the experiments conducted in this investigation, the mean acquisition rate was always greater than 30 Hz.

3.7 Frequency analysis

Estimates of the vortex shedding frequency at various locations in the wakes of uniform, single, and dual step cylinders were completed through analysis of flow visualization videos. In order to validate these estimates, spectral analysis of wake velocity measurements was performed for uniform circular cylinders. Wake velocity data acquired for spectral analysis were re-sampled at a fixed frequency using the sample-hold technique developed by Adrian & Yao (1987). Figure 3.4 shows a segment of original and re-sampled data acquired in the wake of a uniform cylinder of diameter D. Each re-sampled velocity signal was divided into 32 non-overlapping blocks, each containing 512 data points. The Discrete Fourier Transform (DFT) was used to compute the 32 spectra, which were averaged. The resulting frequency resolution was approximately ±0.0025 fD/U. As shown in Appendix

C, the maximum discrepancy between the vortex shedding frequency estimates from velocity measurements and video analysis is within the frequency resolution of the velocity spectra.

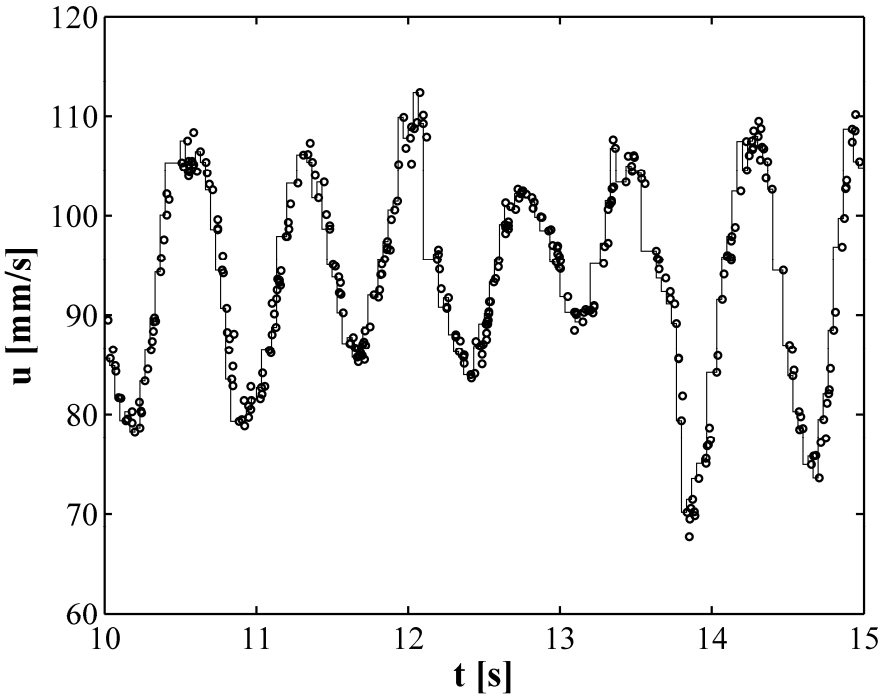

Figure 3.4 Re-sampled and original velocity data obtained by LDV. o raw velocity data, — re-sampled velocity data. The mean sampling frequency was 65 Hz and the re-sampled data were acquired at 30 Hz.

4 Computational Setup

All computational studies were performed on a custom built workstation with two Intel Xeon E5520 processors and 12 GB of RAM. Each Intel Xeon E5520 processor contains four physical cores with each core capable of running two virtual threads. Hence, when running at full capacity, sixteen threads are employed.

A finite-volume based solver (ANSYS CFX 12.0) was used with the pressure-velocity coupling handled by the Rhie-Chow interpolation scheme. For spatial discretization, a second-order high resolution scheme was employed (Barth & Jespersen, 1989). A second-order implicit backward Euler scheme was used, with a fixed time step selected based on preliminary mesh independence studies discussed in the following sections. Numerical simulations of the flow past a uniform cylinder and a single step cylinder have been completed for Re_D = 150, 300, and 1050. The Reynolds numbers selected pertain to three different flow regimes based on flow past a uniform circular cylinder: laminar shedding regime ($50 < Re_D < 190$), wake transition regime ($190 < Re_D < 1000$), and shear layer transition regime ($1000 < Re_D < 200{,}000$). Simulations were performed for Re_D = 150 and 300 to enable comparison of the results with experiments by Dunn (2004) completed at the matching Reynolds numbers. Simulations performed for Re_D = 1050 were designed to complement the flow visualization experiments completed at the matching Reynolds number and discussed in Chapter 5.

4.1 Laminar Simulations

For the simulations performed at Re_D = 150 and 300, the Laminar Navier-Stokes equations (Eq. 4.1) were discretized and solved. The same approach has been utilized to

successfully model flow past uniform circular cylinders for about $Re_D \leq 300$ (e.g., Persillon & Braza, 1998; Henderson, 1997; Zhang et al., 1995).

$$\rho \frac{\partial \vec{u}}{\partial t} + \rho(\vec{\nabla} \cdot \vec{u})\vec{u} = -\vec{\nabla}p + \mu\nabla^2\vec{u} \tag{4.1}$$

The computational domain for the laminar simulations is depicted in Fig. 4.1. The inlet boundary is placed 10D upstream and the outlet boundary is placed 20D downstream from the centre of the cylinder. The boundaries in the y-direction are placed 8D from the cylinder centre. The depth of the domain in the z-direction was selected based on the experimental results presented by Dunn & Tavoularis (2006). For $Re_D = 300$, the spanwise depth of the domain is 20D, with the large and the small cylinders occupying 15D and 5D, respectively. This domain size is comparable to that used by Narasimhamurthy et al. (2009) for modeling flow over a tapered cylinder. For $Re_D = 150$, the spanwise depth of the domain is 30D, with the large and the small cylinders occupying 25D and 5D, respectively. A free-slip wall boundary condition is applied at the left, right, top, and bottom surfaces of the domain and a no-slip condition is applied at the model surface. At the inlet boundary, a uniform velocity profile, (u, v, w) = (U, 0, 0), and a Neumann boundary condition for the pressure are used; whereas, at the outlet, a Neumann condition for the velocity and a constant (zero) pressure are applied.

A structured O-grid type mesh was employed (Fig. 4.1), with mesh refinement carried out in two phases. First, to ensure adequate mesh density for the large and the small cylinders away from the step, mesh independence was investigated for a three-dimensional uniform circular cylinder in a computational domain with the same planar (x-z) dimensions as those in Fig. 4.1 and a span of 6D. Several mesh configurations, selected based on previous numerical simulations (e.g., Narasimhamurthy et al., 2009; Mittal, 2001), were investigated

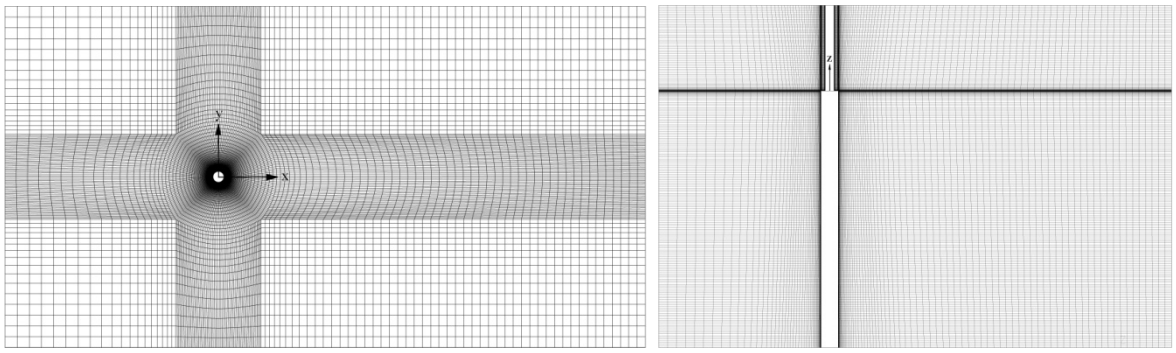

(a) (b)

Figure 4.1 Computational mesh for laminar simulations.

for three Reynolds numbers, Re_D = 75, 150, and 300 (Table 3). For each mesh configuration, the drag coefficient and the Strouhal number were computed based on the analysis of more than 30 vortex shedding cycles, with selected results shown in Table 3. Using the results presented in Table 3, the following mesh configurations were selected: (i) mesh configuration 3 for Re_D = 75 and 150, and (ii) mesh configuration 6 for Re_D = 300. The two-dimensional planar mesh density of the selected meshes is comparable to that used by Mittal (2001) for modeling flow development over a uniform circular cylinder. Agreeing with previous numerical simulations (e.g., Zhang et al., 1995; Henderson, 1995; Henderson, 1997; Persillon & Braza, 1998), the numerical results pertaining to the selected mesh configurations (Table 3) show a slight over-prediction of the drag coefficient and the Strouhal number compared to experimental data. This is attributed primarily to blockage and upstream boundary effects, as discussed by Persillon & Braza (1998).

Similar to numerical studies on free-end cylinders (e.g., Afgan et al., 2007), the second phase of mesh refinement involved the region near the step. The spanwise mesh spacing at the step location and its gradual relaxation away from the step matches the corresponding radial mesh spacing at the cylinder surfaces and the relaxation in the radial direction away

from the cylinder. The resulting final meshes contain approximately $3.5x10^6$ and $4.5x10^6$ elements for $Re_D = 150$ and $Re_D = 300$, respectively.

All numerical data presented were acquired when steady spanwise vortex shedding in the wakes of both the large and the small cylinders was attained in the simulations. A fixed time step was used for all laminar simulations so that the resulting CFL number was less than 2 for the entire computational domain. The duration of velocity data segments acquired for spectral analysis provided a dimensionless frequency resolution of ±0.0045 fD/U, adequate to resolve narrow peaks in the spectra. Each velocity spectrum presented is normalized by the variance of the corresponding velocity signal.

It should be noted that the two Reynolds numbers investigated in this study are associated with the laminar shedding regime ($Re_D = 150$) and the wake transition regime ($Re_D = 300$) in the wake of the large cylinder. In the wake transition regime, which starts at $Re_D \approx 190$, the transition to turbulence in the wake advances upstream with an increase of the Reynolds number. However, similar to other transient regimes, the critical Reynolds number at which the transition reaches the vortex formation region varies in the range of about $260 < Re_D < 500$ (Karniadakis & Triantafyllou, 1992; Williamson, 1996b; Unal & Rockwell, 1988; Norberg, 2001). Based on velocity spectra presented by Dunn & Tavoularis (2006), there is no indication of flow transition in the wake of the large cylinder within $0 \leq x/D \leq 5$ for $Re_D \approx 300$. As suggested by Williamson (1996), vortex shedding in this regime is similar to that in the laminar mode except for the small-scale streamwise vortices forming in the wake, which, similar to previous numerical investigations (e.g., Zhang et al., 1995; Persillon & Braza, 1998), were resolved in the present study. Unsteady Reynolds Averaged Navier-Stokes (URANS) based simulations were conducted as part of the present investigation. A

comparative analysis of the URANS results and those from laminar Navier-Stokes simulations, presented in Appendix E, did not reveal any significant deviation in the characteristics of the main spanwise vortex cells. In light of this, laminar Navier-Stokes simulation results are presented in this investigation for both Re_D = 150 and 300.

Table 3 Mesh refinement results for flow over a uniform circular cylinder with a span of 6D.

Configuration	x-y cells*	Δz cells**	Re_D = 75		Re_D = 150		Re_D = 300	
			C_D	St	C_D	St	C_D	St
1	7136	30	1.37	0.153	1.32	0.189	-	-
2	10704	30	1.40	0.154	1.34	0.190	1.27	0.189
3	16056	30	1.41	0.155	1.35	0.190	-	-
4	10704	48	-	-	-	-	1.29	0.203
5	16056	48	-	-	-	-	1.32	0.205
6	16056	60	1.41	0.156	1.35	0.190	1.36	0.210
7	16056	80	-	-	-	-	1.37	0.211
Norberg (2003)	-	-	-	0.149	-	0.184	-	0.203
Wieselberger (1921)	-	-	1.36	-	1.30	-	1.21	-
Zhang et al. (1995), Henderson (1995, 1997), Persillon & Braza (1998)	-	-	1.38-1.5	0.151-0.156	1.27-1.42	0.181-0.191	1.28-1.37	0.206-0.212

*The total number of cells in each x-y planar mesh
**The total number of spanwise cells in the computational domain

4.2 DES Method

For Re_D = 1050, a Large Eddy and Reynolds Averaged Navier-Stokes hybrid simulation (LES-RANS), commonly known as Detached Eddy Simulation (DES), is employed in order to model turbulent wake development. For DES, a RANS approach is used upstream of the cylinder and within the boundary layers on the cylinder surface. The wake region is solved with an LES approach. Between these two regions, i.e., within the separated shear layers and surrounding area, a blending function is used to smoothly

transition between RANS and LES. Detailed information on individual RANS and LES solution methods can be found in Pope (2008), and a comprehensive review of the DES method is given by Spalart (2009).

DES has been applied to model flow development over uniform circular cylinders and the results have shown an improved agreement with experiments compared to RANS-based models, e.g., Nishino et al. (2008), Mockett et al. (2009). In this study, the SST-DES model developed by Menter and Kuntz[1] was employed using the ANSYS CFX 12.0 solver.

The computational domain is shown in Fig 4.2, with the origin of the coordinate system located on the cylinder axis at the step. The inlet boundary is placed 10D upstream and the outlet boundary is placed 20D downstream from the centre of the cylinder. The transverse boundaries are placed 8D from the cylinder centre. The spanwise depth of the domain is 19D, with the large and small cylinders occupying 15D and 4D, respectively. The domain size is comparable to that used by Narasimhamurthy et al. (2009) for modeling flow over a tapered cylinder.

A free-slip wall boundary condition is applied at the left, right, top, and bottom surfaces of the domain and a no-slip condition is applied at the model surface. At the inlet boundary, a uniform velocity profile, (u, v, w) = (U, 0, 0), and a Neumann boundary condition for the pressure are used; whereas, at the outlet, a Neumann condition for the velocity and a constant (zero) pressure are applied.

A structured O-grid mesh was employed, with mesh refinement carried out in two phases. First, the mesh for the regions away from the step was selected based on a mesh independence study completed for a three-dimensional uniform cylinder with an in-plane depth of 3D and the same planar (x-y) dimensions as those in Fig. 4.2a. Mesh configurations

[1] Menter, F. R., and Kuntz, M., CFX validation report CFX-VAL17/0503

were investigated for Re_D = 1050, corresponding to flow past the large cylinder, since the results would be applicable to the small cylinder at Re_D = 525. To ensure convergence of the numerical results, each configuration was run for more than 30 vortex shedding cycles. Based on the drag coefficient and Strouhal number results presented in Table 4, mesh configuration 2 was selected for both the large and the small cylinder. The corresponding two-dimensional mesh density and spanwise mesh spacing is comparable to that used by Nishino et al. (2008) for modeling flow development past a uniform circular cylinder in ground effect.

In the second phase of mesh refinement, the spanwise mesh density in a region surrounding the step was increased to resolve boundary layer and shear layer development. Specifically, the spanwise mesh spacing at the step and its gradual relaxation away from the step matches the corresponding radial mesh spacing at the cylinder surfaces and the relaxation in the radial direction away from the cylinder. As a result, on the large cylinder side, 34 spanwise cells were located within $-0.75 \leq z/D \leq 0$. On the small cylinder side, 29 spanwise cells were located within $0 \leq z/D \leq 0.375$. The final mesh contained approximately 5.6×10^6 elements.

All numerical data presented were acquired after steady spanwise vortex shedding in the wakes of the large and small cylinders was attained in the simulations. A fixed time step was used in all DES simulations so that the CFL number was less than 1 in the LES region of the flow, and less than 2 in the remainder of the domain.

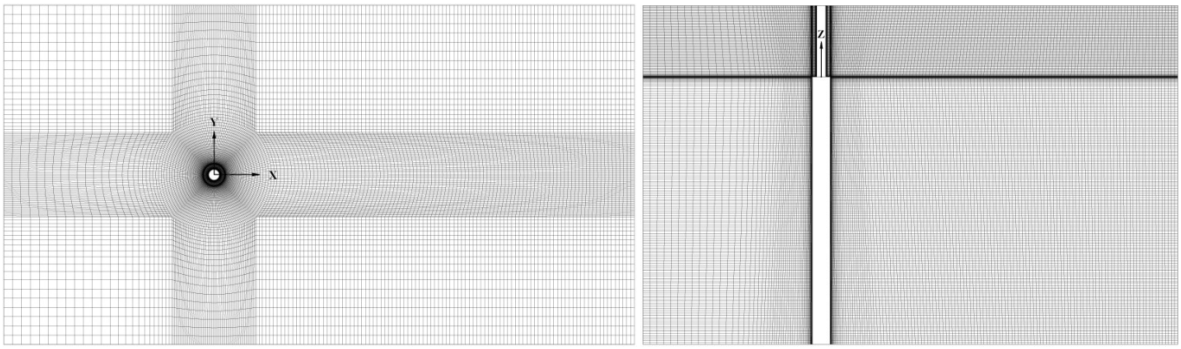

(a) (b)

Figure 4.2 Computational mesh for SST-DES simulations.

Table 4 Mesh refinement results for flow over a uniform circular cylinder with a span of 3D.

Mesh Config.	x-y Cells*	Δz Cells**	Time Step, ΔtU/D	Re_D	C_D	St
1	25000	20	0.006	1050	1.199	0.22
1	25000	20	0.012	1050	1.199	0.223
2	25000	30	0.012	1050	1.179	0.221
3	25000	60	0.012	1050	1.174	0.22
4	50000	60	0.012	1050	1.160	0.22
2	25000	30	0.012	525	1.227	0.228
Norberg (2003) and Wieselberger (1921)	-	-	-	1050	0.97	0.210
	-	-	-	525	1.02	0.205

*The total number of cells in each x-y planar mesh
**The total number of spanwise cells in the computational domain

4.3 Numerical Data Analysis

Velocity signals were acquired in the simulations for spectral analysis. The duration of velocity signals ensured a frequency resolution of approximately ±0.0045fD/U. With this frequency resolution small differences in the shedding frequency between adjacent vortex cells can be resolved.

4.4 Visualization methods

Wake vortex shedding can be visualized through a number of methods, e.g., Q-Criterion (Hunt et al., 1988), λ_2 definition (Jeong & Hussain, 1995), or total vorticity data. Figure 4.3 shows a visualization of vortex shedding in the wake of a uniform circular cylinder for $Re_D = 300$ using the abovementioned visualization methods. As can be seen in Figs. 4.3a-c, these methods of vortex identification yield similar results for the spanwise vortices. In the next section, both Q-criterion and total vorticity data are presented.

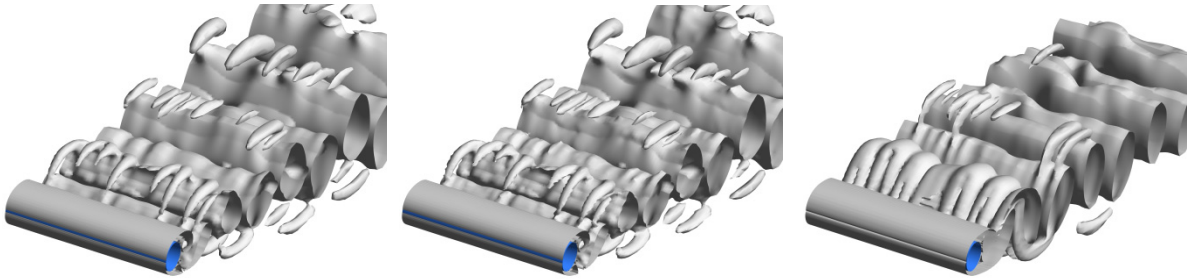

(a) Q-criterion (b) λ_2 definition (c) total vorticity

Figure 4.3 Laminar Navier Stokes visualization of vortex shedding in the wake of a uniform cylinder at $Re_D = 300$: (a) Q-criterion, (b) λ_2 definition, and (c) total vorticity.

5 Results and Discussion

Experimental and numerical results obtained for a uniform cylinder, a single step cylinder, and a dual step cylinder are presented in this section. To establish a baseline for comparison, results pertaining to a uniform cylinder are presented first. Then, the single step cylinder results are discussed. These include laminar flow simulations for Re_D = 150 and 300, followed by experimental flow visualization and turbulent flow simulations for Re_D = 1050. Finally, dual step cylinder results are presented and include experimental flow visualization for Re_D = 1050 and $0.2 \leq L/D \leq 17$.

5.1 Flow development over uniform circular cylinders

For the single and dual step cylinder geometries with D/d = 2, the Reynolds numbers investigated, i.e., Re_D = 150, 300, and 1050, correspond to 75, 150, and 525 (based on the small cylinder diameter). Thus, flow past uniform cylinders for Re_D = 75, 150, 300, 525, and 1050 were investigated, and the results are presented in this section.

5.1.1 Laminar flow simulations on the flow past uniform cylinders

Numerical results depicting vortex shedding in the wake of a uniform cylinder for Re_D = 75, 150, and 300 are presented in Figs. 5.1a-c using instantaneous isosurfaces of $Q \approx 3x10^{-4}$. The results show vortices shed in a single cell of constant frequency across the entire cylinder span. For Re_D = 75 and 150, the vortex shedding is two dimensional (Fig. 5.1a-b). However, for Re_D = 300, Mode B vortex shedding is observed in the cylinder wake (Fig. 5.1c), with the development of vortex deformations and small-scale streamwise vortices. The small-scale streamwise vortices are characteristic of this mode of shedding, and their spanwise spacing is in agreement with experimental observations (e.g., Williamson, 1996).

The three-dimensional numerical flow visualizations, like those presented in Fig. 5.1, are beneficial for understanding flow development since such visualizations are currently impossible to obtain with experimental methods. It is also useful to directly compare numerical and experimental flow visualizations. To enable such a comparison, Figs. 5.2a-f show planar images of total vorticity magnitude contours in the cylinder wake for Re_D = 75, 150, and 300. The position of selected planes for which vorticity contours are generated are approximately matching those used for the experimental flow visualizations discussed in section 3.5. The vorticity contours in Figs. 5.2b, 5.2d, and 5.2f are in good qualitative agreement with experimental flow visualizations (for example, Fig. 1, Williamson, 1996). In particular, the numerical results show that increasing the Reynolds number leads to a decrease in the vortex formation length and increase in the dimensionless vortex shedding frequency (Figs. 5.2b, 5.2d, and 5.2f). Vorticity contours in Figs. 5.2a, 5.2c, and 5.2e illustrate the change from two-dimensional vortex shedding (Re_D = 75 and 150) to three-dimensional vortex shedding (Re_D = 300). The streamwise vortices forming for Re_D = 300 leave a distinct signature in the vorticity contours (Fig. 5.2e), which has been observed in experimental flow visualizations at comparable Reynolds numbers (e.g., Wu et al., 1996).

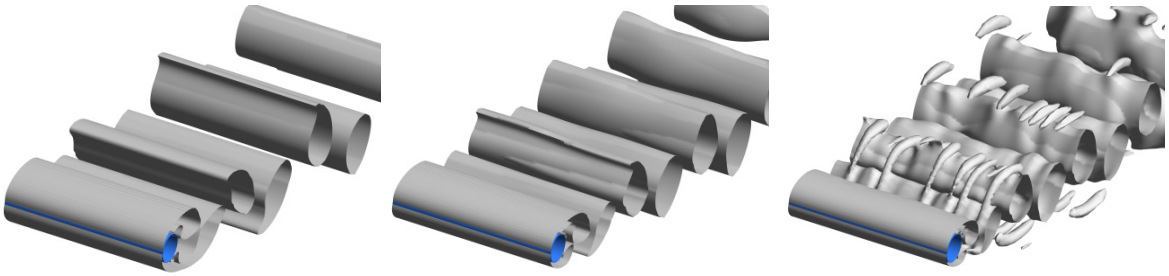

(a) Re_D = 75 (b) Re_D = 150 (c) Re_D = 300

Figure 5.1 Laminar vortex shedding in the wake of a uniform cylinder visualized with isosurfaces of $Q \approx 3x10^{-4}$: (a) Re_D = 75, (b) Re_D = 150, and (c) Re_D = 300.

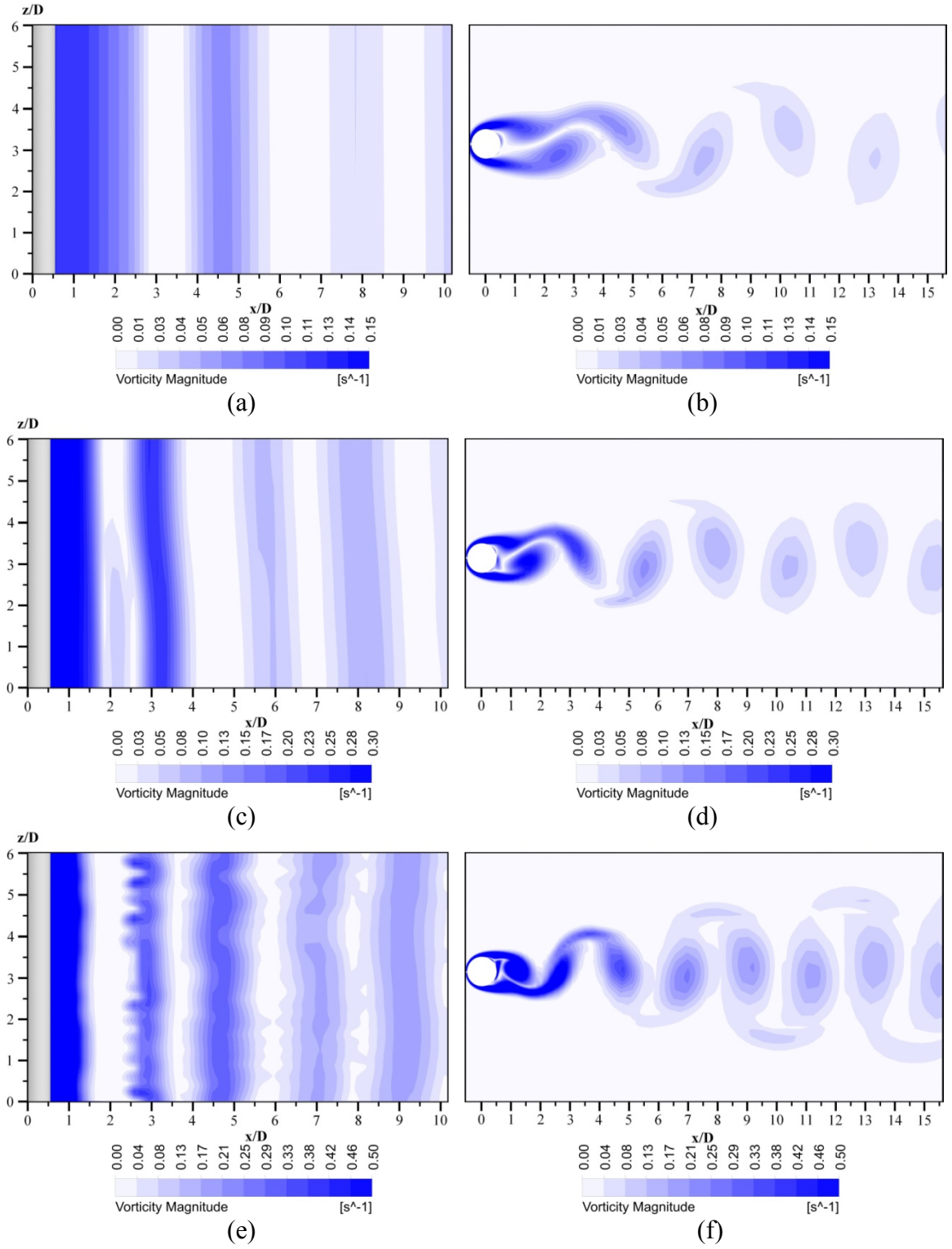

Figure 5.2 Laminar vortex shedding in the wake of a uniform circular cylinder visualized with vorticity magnitude contours: (a) Re_D = 75, y/D = 0.55, (b) Re_D = 75, z/D = 3, (c) Re_D = 150, y/D = 0.55, (d) Re_D = 150, z/D = 3, (e) Re_D = 300, y/D = 0.55, (f) Re_D = 300, z/D = 3.

Normalized spectra of streamwise velocity data for Re_D = 75, 150, and 300, are shown in Figs. 5.3a-c. The predicted dimensionless shedding frequencies, St = 0.156, 0.190, and 0.210, are in good agreement with previous experimental and numerical results for Re_D = 75, 150, and 300, respectively (Table 3). For Re_D = 300 (Fig. 5.3c) the small-scale streamwise vortices induce random perturbations in the velocity signal, resulting in minor peaks in the spectrum in addition to the dominant peak at the shedding frequency.

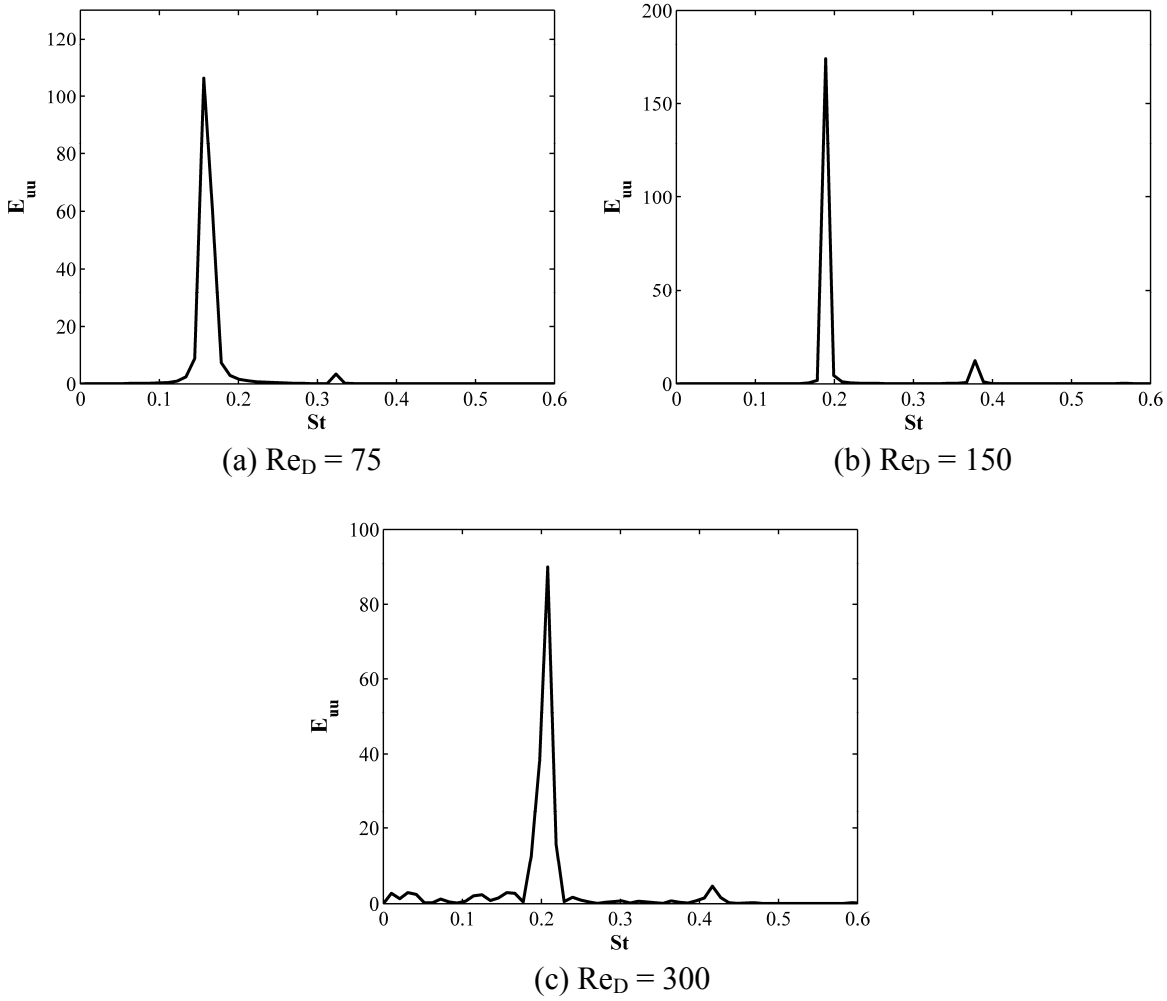

(a) Re_D = 75

(b) Re_D = 150

(c) Re_D = 300

Figure 5.3 Velocity spectra in the wake of a uniform circular cylinder: (a) Re_D = 75, (b) Re_D = 150, (c) Re_D = 300.

5.1.2 Experimental and SST-DES results for the flow past a uniform cylinder

Experimental flow visualization of vortex shedding in the wake of a uniform circular cylinder for Re_D = 525 and 1050 is presented in Figs. 5.4a-d. The results pertain to a region away from the end plates, showing nearly parallel vortex shedding (Figs. 5.4a and 5.4c). Planar LIF images (Figs. 5.4b and 5.4d) visualize a vortex street. Similar to previous experimental studies, e.g., Stansby (1974) and Gerich & Eckelmann (1982), vortex shedding was affected near endplates, with end cells forming within about 4-5 diameters from each endplate. An analysis of video records revealed that, apart from the end cells, the shedding frequency is constant along the span of the cylinders, with St = 0.198 and St = 0.203 for Re_D = 525 and 1050, respectively. These values of the Strouhal number are in agreement with previous experimental results reported by Norberg (2003) for the corresponding Reynolds number.

Flow visualization images in Figs. 5.4a and 5.4c reveal three-dimensional structures known to occur in the wake of a uniform cylinder at the investigated Reynolds numbers (Wu et al., 1996). Based on flow visualization results similar to those shown in Figs. 5.4a and 5.4c, Wu et al. (1996) noted three-dimensional “mushroom-type structures” appearing along the cylinder axis in the near wake region. These structures are caused by streamwise vortices forming in the near wake region and intersecting the visualization plane. Such structures can be seen, for example, in Fig. 5.4a at x/D = 3.25 and z/D = 3.5, and in Fig. 5.4c at x/D = 5.0 and z/D = 7.25.

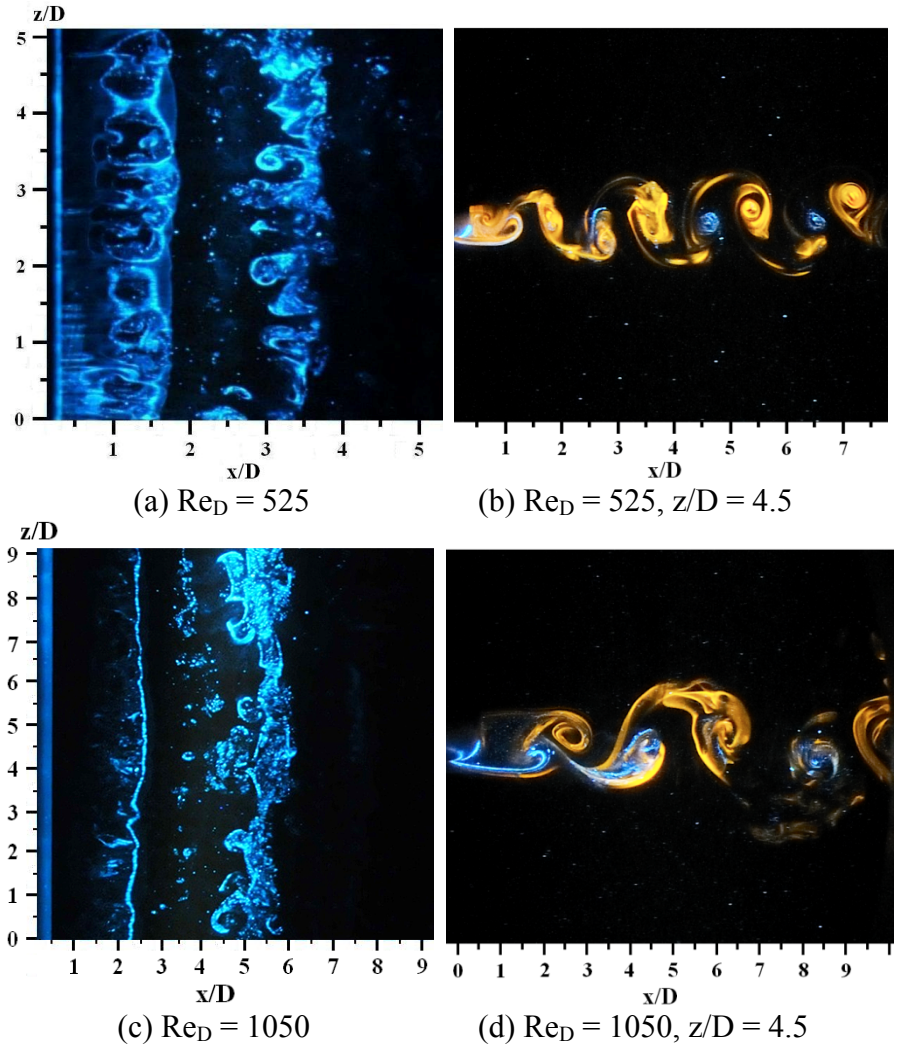

Figure 5.4 Experimental visualization of vortex shedding in the wake of a uniform circular cylinder at Re_D = 525 and 1050.

Numerical results for Re_D = 1050 are presented in Figs. 5.5a-c, all of which pertain to the same instant in the simulation. Numerical flow visualization with isosurfaces of Q ≈ $2x10^{-3}$ is shown in Fig. 5.5a. The resolved structures in the wake are in agreement with previous DES studies on uniform circular cylinders (Nishino et al., 2008; Mockett et al., 2009). The SST-DES results (Table 4) give St = 0.228 and St = 0.221 for Re_D = 525 and 1050, respectively, with the Strouhal number values being within about 10% of the

experimental results reported by Norberg (2003) and agreeing with previous SST-DES simulations (e.g., Mockett et al., 2009; Revell et al., 2008).

Similar to experimental results (Wu et al., 1996), numerical results reveal the formation of streamwise vortices in the near wake. For comparison, contours of total vorticity magnitude are shown in Figs. 5.5b and 5.5c at x-z and x-y planes matching the position of the laser sheets in the flow visualization images presented in Figs. 5.4c and 5.4d. The numerical results are in good agreement with the corresponding flow visualization results in Fig. 5.4c and 5.4d. Comparing Figs. 5.5a and 5.5b, it can be seen that the three-dimensional

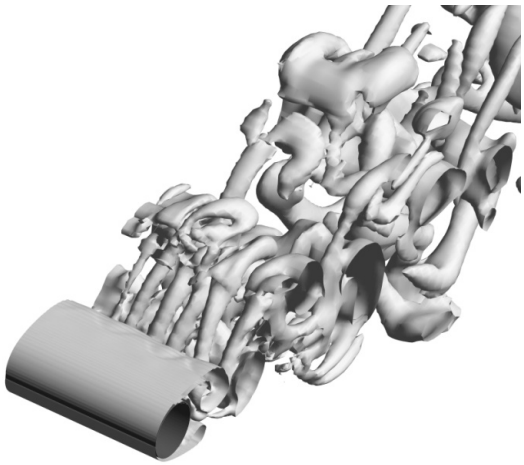

(a) $Re_D = 1050$, isosurfaces of $Q \approx 2x10^{-3}$

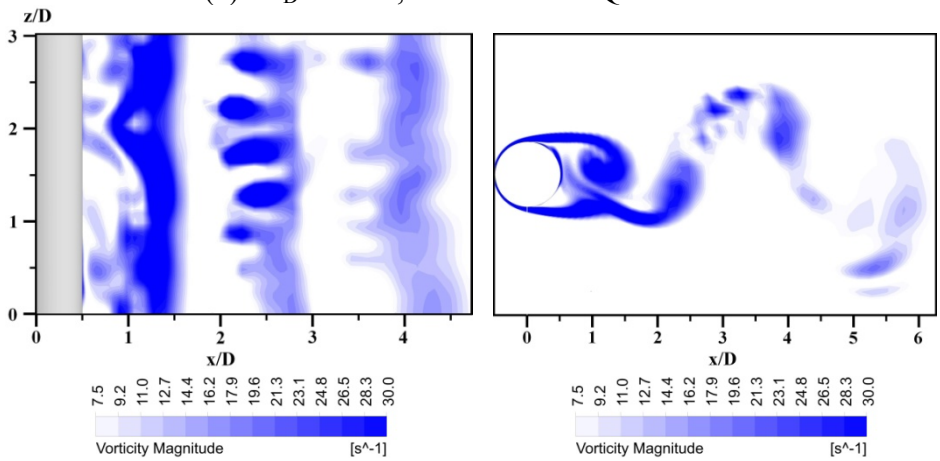

(b) $Re_D = 1050$, y/D = 0.375 (c) $Re_D = 1050$, z/D = 1.5

Figure 5.5 DES results depicting vortex shedding in the wake of a uniform circular cylinder at $Re_D = 1050$.

streamwise vortices leave distinct footprints on a planar vorticity plot, for example, at x/D = 2.5 and z/D = 1.25, 1.75, 2.25 and 2.75. These footprints are representative of the mushroom-type structures seen in experimental flow visualization images (Figs. 5.4a and 5.4c).

It was discussed previously that spanwise vortex deformations no longer appear in a periodic fashion as the Reynolds number increases from about Re_D = 240-1000. This leads to a less ordered distribution of streamwise vortices along the span. Evidence of this can be seen by comparing the DES results for Re_D = 1050 in Fig. 5.5a with the laminar Navier-Stokes results for Re_D = 300 in Fig. 5.1c. A comparison of the experimental flow visualization images in Fig. 5.4a and 5.4c with the numerical flow visualization image in Fig. 5.2e illustrates the similar trend.

Streamwise velocity data were obtained experimentally in the wake of a uniform circular cylinder for Re_D = 525 and 1050. The normalized spectra are plotted in Figs. 5.6a and 5.6b for Re_D = 525 and 1050, respectively. The dominant peaks in the spectra attributable to vortex shedding, are located at St = 0.199 for Re_D = 525 and at St = 0.203 for Re_D = 1050. These values are in excellent agreement with previously published experimental results (Norberg, 2003). In addition to the dominant peak at the vortex shedding frequency, smaller magnitude peaks can be seen in the spectra at the first and second harmonics of the shedding frequency (Fig. 5.3). The above estimates of the Strouhal number for Re_D = 525 and 1050 were used to validate estimates obtained through analysis of flow visualization video records (Appendix C).

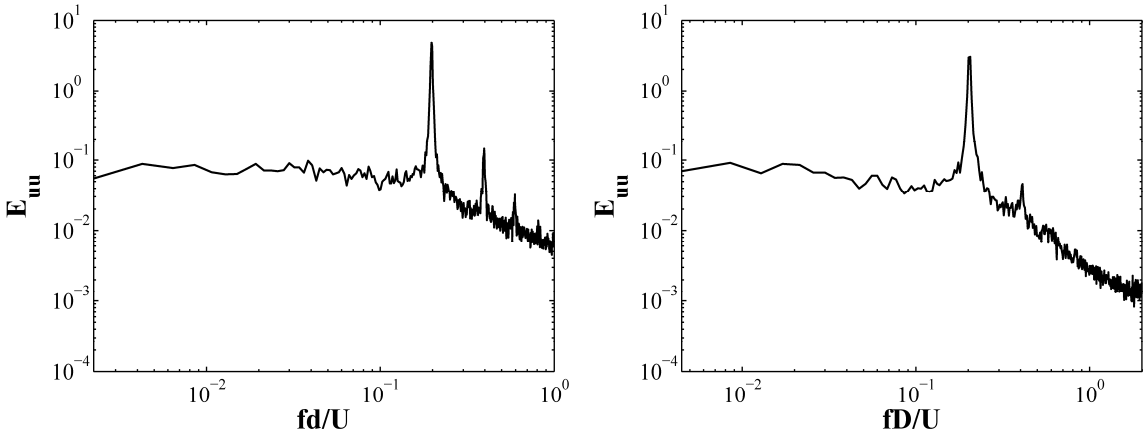

(a) (b)

Figure 5.6 Experimental velocity spectra in the wake of a uniform circular cylinder: (a) Re_D = 525 and (b) Re_D = 1050.

5.2 Flow development over a single step cylinder

The results of experimental and numerical studies completed on the single step cylinder geometry are discussed in this section. The flow development in the wake of a step cylinder is first investigated for Re_D = 150 and 300 using laminar Navier-Stokes simulation results. Then, the experimental flow visualization and SST-DES simulation results are presented.

5.2.1 Laminar Navier-Stokes simulations of the flow past a single step cylinder

The numerical results for Re_D = 150 are presented in Fig. 5.7a using instantaneous isosurfaces of Q ≈ $2x10^{-3}$. Agreeing with previous experimental findings of Dunn & Tavoularis (2006) and Lewis & Gharib (1992), three distinct vortex shedding cells can be identified in the wake, namely, the N-cell, the L-cell, and the S-cell. As expected, the vortex shedding frequency of the S-cell is higher than the L-cell and N-cell shedding frequencies, which is evidenced by a higher number of vortices in the S-cell region compared to that in

either the L-cell or the N-cell region. The development of the wake vortices obtained from the numerical simulations agrees well with experimental results. Similar to the results of Dunn & Tavoularis (2006), formation of a horseshoe vortex and edge vortices at the step was also observed in the simulations. The edge vortices are weaker in comparison with the horseshoe vortices, making them difficult to detect in experimental flow visualization (Dunn & Tavoularis, 2006). Streamwise vortices forming at the step are depicted in Fig. 5.8 using instantaneous isosurfaces of positive and negative streamwise vorticity. Downstream of the step, the streamwise vortices are affected by the vortex shedding. This can be seen by comparing Fig. 5.8a with 5.8b, which show that the downstream extent of the horseshoe vortex varies with time. It should be noted that for clarity, the near wake development of spanwise vortices is not shown in Fig. 5.8.

The numerical results for Re_D = 300 (Fig. 5.7b) also show three distinct vortex shedding cells in the step cylinder wake. However, as expected based on experimental

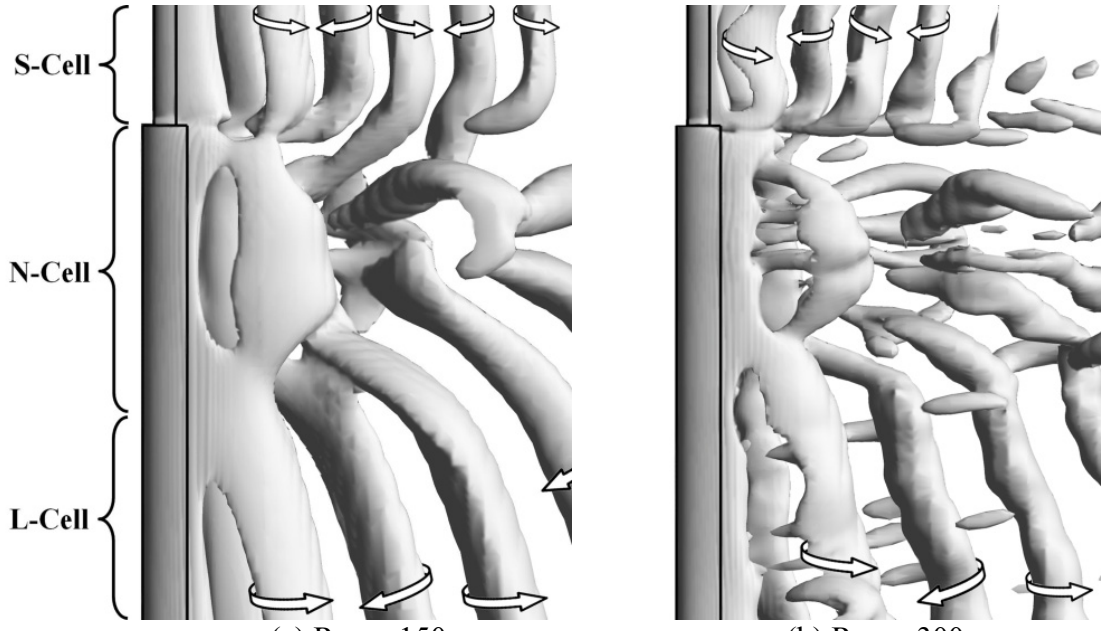

(a) Re_D = 150 (b) Re_D = 300

Figure 5.7 Vortex shedding in the wake of a step cylinder: (a) isosurfaces of Q ≈ $2x10^{-3}$ for Re_D = 150 and D/d = 2, (b) isosurfaces of Q ≈ $2x10^{-3}$ for Re_D = 300 and D/d = 2.

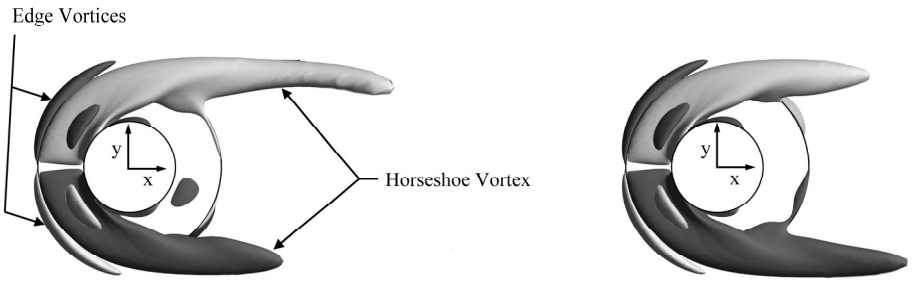

(a) t* = 0 (b) t* = 1.72

Figure 5.8 Visualization of the horseshoe vortex and edge vortices forming at the step junction at Re_D = 150 using isosurfaces of streamwise vorticity. ■ negative streamwise vorticity, ■ positive streamwise vorticity. t* is the simulation time multiplied by the S-cell shedding frequency.

observations for a uniform circular cylinder at a matching Reynolds number (Williamson, 1996), small-scale streamwise vorticies can be seen in the wake of the large cylinder for Re_D = 300 (Fig. 5.7b and more clearly in Fig. 5.9c). An increase in streamwise circulation due to these small-scale structures is associated with the weakening of the spanwise vortices in the N-cell and the L-cell, similar to the trend observed for uniform circular cylinders (Norberg, 2001).

As can be seen in Fig. 5.7, intricate vortex interactions take place at the cell boundaries for both Reynolds numbers investigated. The vortex interactions and the N-cell development will be discussed in more detail in the following sections.

Vortex interactions between the S-cell and the N-cell

Interactions between N-cell and S-cell vortices in the near wake are illustrated in Fig. 5.9. It is instructive to focus first on the results pertaining to Re_D = 150, shown in Fig. 5.9a. The difference in shedding frequencies in the wakes of the large and the small cylinders results in complex connections between wake vortices. Analysis of the numerical results showed that, at the boundary between the N-cell and S-cell, N-cell vortices split into at least

two filaments. One of these filaments forms a direct connection with an S-cell vortex of the same sign. To accommodate for the difference in strengths between the N-cell and the S-cell vortices, the other filament forms a looped connection with a subsequent N-cell vortex of the opposite sign, for example, vortex N1 connects to vortices S1 and N2 (Fig. 5.9a). S-cell vortices that do not connect with N-cell counterparts form half-loop connections, for instance, counter-rotating vortices S2 and S3 form such a connection in Fig. 5.9a. Figure 5.9b shows an experimental flow visualization image by Dunn & Tavoularis (2006). To allow adequate comparison, the numerical results in Fig. 5.9a were selected to match the shedding cycle phase of the experimental results in Fig. 5.9b. The image in Fig. 5.9b features vortex connections analogous to those deduced from the numerical results, and both images agree with flow visualization results of Lewis & Gharib (1992). For Re_D = 300, the numerical results reveal similar connections between N-cell and S-cell vortices (Fig. 5.8c). For example, vortex N1 connects with vortices S2 and N2, while vortices S3 and S4 form a half loop connection. On the other hand, the presence of small-scale streamwise vortices

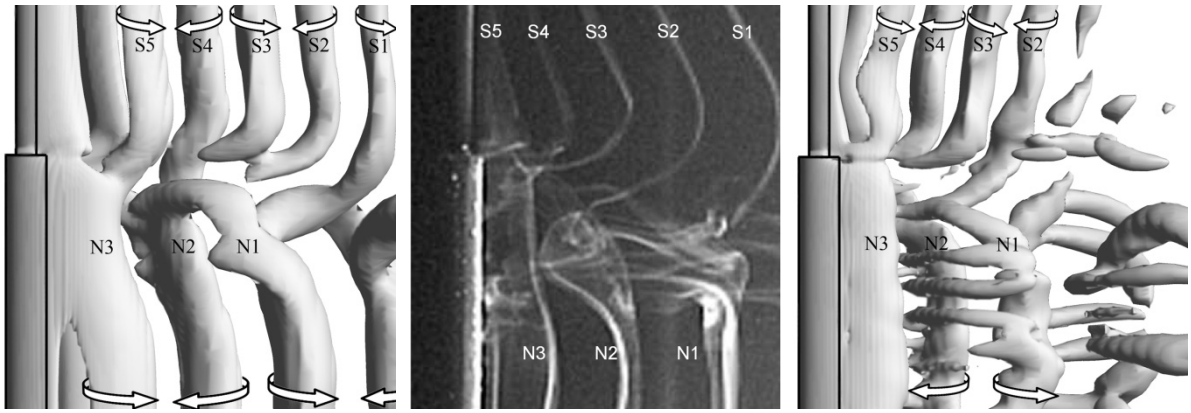

(a) Re_D = 150 (b) Re_D = 152 (c) Re_D = 300

Figure 5.9 Vortex interactions occurring at the N-S cell boundary: (a) isosurfaces of Q ≈ $2x10^{-3}$ for Re_D = 150 and D/d = 2, (b) flow visualization image by Dunn & Tavoularis (2006) for Re_D = 152 and D/d = 1.98, (c) isosurfaces of Q ≈ $2x10^{-3}$ for Re_D = 300 and D/d = 2.

complicates significantly the wake development and vortex interactions between the neighboring cells for this Reynolds number. As was noted earlier, the formation of streamwise vortices for $Re_D = 300$ is linked to the decrease of the primary circulation in the N-cell. Thus, weaker vortex connections occur across the cell boundaries and between the primary N-cell vortices. Also, comparing Figs. 5.7c and 5.9c, it can be noted that the strength of streamwise vortices in the wake of the large cylinder varies during the N-cell cycle.

The results in Fig. 5.9 indicate that vortex dislocations along the N-S cell boundary, caused by the difference in the shedding frequencies of the two cells, occur in the form of half-loop connections between small cylinder vortices (e.g., vortices S3 and S4 in Fig. 5.9a). Over any given time period (T_1), the difference between the number of vortices shed in the S-cell and N-cell is given by $2T_1(f_S - f_N)$. Since each N-cell vortex always connects to one S-cell vortex, the half-loop connections between two S-cell vortices shed without N-cell counterparts are expected to occur at the beat frequency of $(f_S - f_N)$, i.e., the frequency of vortex dislocations at the N-S boundary.

Development of N-cell vortices and their interaction with L-cell vortices

A detailed analysis of numerical results showed that the spanwise extent of the N-cell varies cyclically with time for both Reynolds numbers investigated. Using the results for $Re_D = 150$, this is illustrated by consecutive images in Figs. 5.10a-h, where selected S-cell, N-cell, and L-cell vortices are numbered to facilitate the discussion. Figure 5.10a corresponds to an arbitrary time in the N-cell cycle, with the N-cell cycle referring to the cyclic changes in the N-cell extent rather than the N-cell vortex shedding. The results show vortex N1 forming direct connections with vortices L1 and S1. As can be seen in Fig. 5.10b, the spanwise extent of the subsequent N-cell vortices N3 and N5 increases, while they continue to maintain

connections with the corresponding L-cell vortices L3 and L5. The growth of the spanwise extent of the N-cell vortices at formation continues in Fig. 5.10c. However, due to a phase lag between the N-cell and the L-cell vortices, caused by a mismatch of the shedding frequencies, newly formed vortex N7 connects primarily to vortex L9 and not L7 (Figs. 5.10c

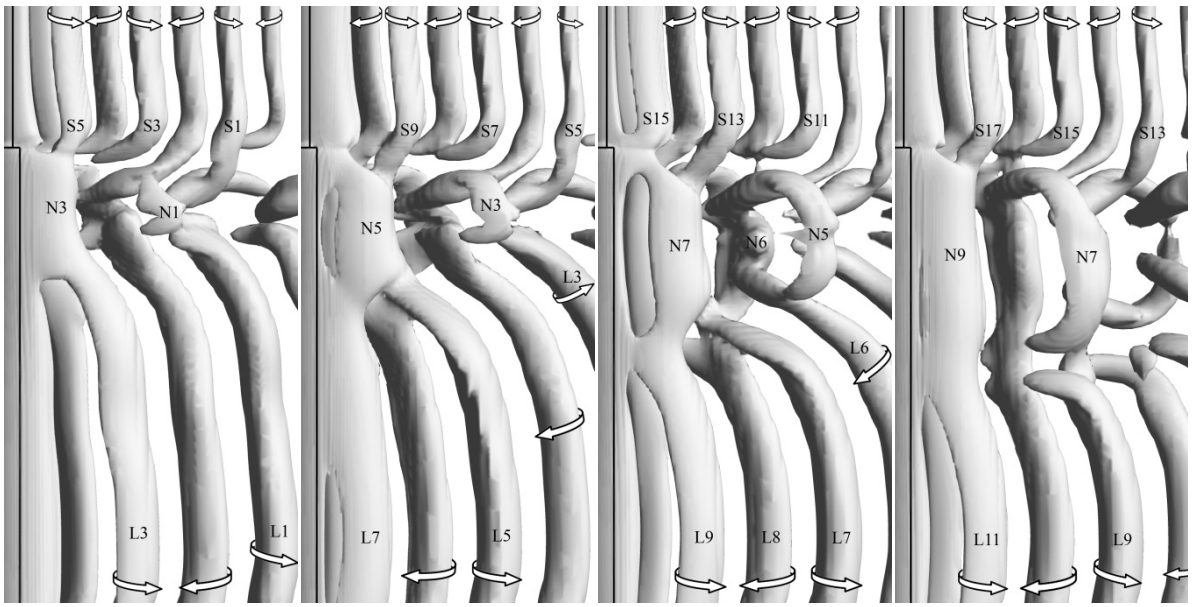

(a) $t/T_N = 0.41$ (b) $t/T_N = 0.58$ (c) $t/T_N = 0.74$ (d) $t/T_N = 0.84$

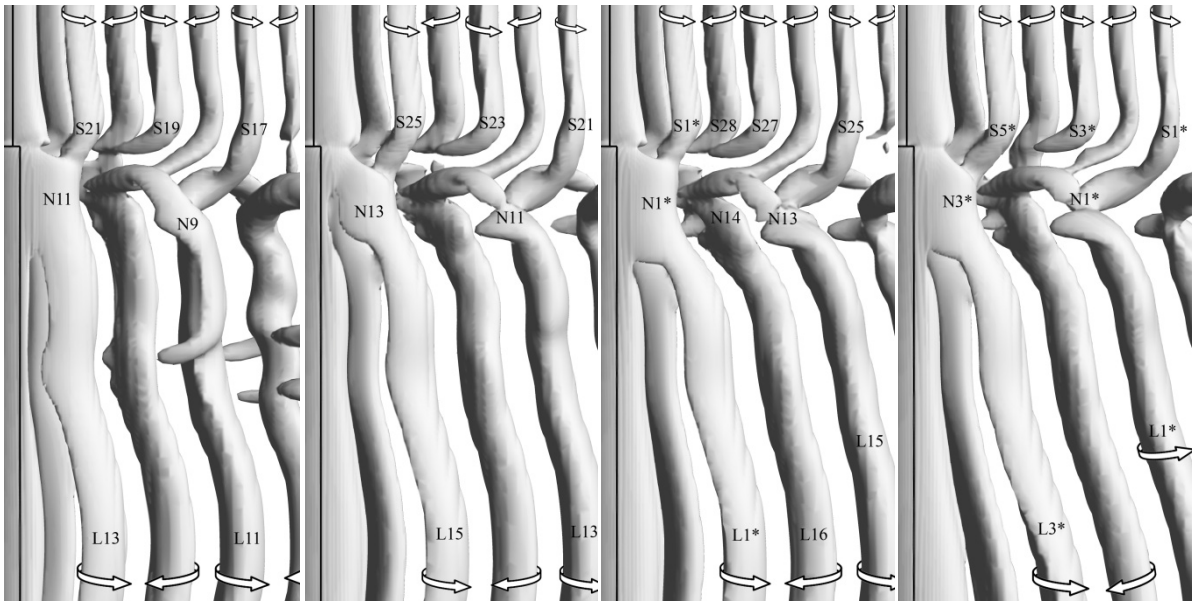

(e) $t/T_N = 0.97$ (f) $t/T_N = 1.13$ (g) $t/T_N = 1.25$ (h) $t/T_N = 1.39$

Figure 5.10 Isosurfaces of $Q \approx 2x10^{-3}$ showing N-cell development. T_N is the period of one N-cell cycle.

and 5.10d). This vortex realignment process is followed by a significant decrease in the spanwise extent of the N-cell, e.g., vortex N11 in Fig. 5.10e. Then, the spanwise extent of the subsequent vortices N13, N1*, and N3* starts to increase again (Figs. 5.10f – 5.10h), and these vortices connect with L-cell vortices L15, L1*, and L3*, respectively. Finally, comparing Figs. 5.10a and 5.10h, it is evident that the two figures approximately correspond to the same phase of the N-cell cycle. Thus, the time elapsed between Figs. 5.10a and 5.10h approximately equals to the period of the N-cell cycle (T_N). The observed cyclical nature of the N-cell is in agreement with the flow visualization results in Dunn & Tavoularis (2006) and Lewis & Gharib (1992). However, Dunn & Tavoularis (2006) suggest that the N-cell formation is interrupted between two consecutive N-cell cycles; whereas, the present results imply that a sudden decrease in N-cell extent occurs instead. Indeed, as the N-cell vortices align in phase with their L-cell counterparts (e.g., N11 and L13), the presence of N-cell vortices could have been difficult to detect during a few L-cell cycles using experimental flow visualization.

Figures 5.10a-h can be used to quantify the differences in the shedding frequencies of the three vortex cells for $Re_D = 150$. Specifically, during the time corresponding to the period of the N-cell cycle, there are 28 S-cell vortices, 14 N-cell vortices, and 16 L-cell vortices shed in the wake. This gives the ratio of N-cell to L-cell vortices of 14/16, corresponding to the ratio of the shedding frequencies $f_N/f_L \approx 0.88$, and the ratio of N-cell to S-cell vortices of 14/28, corresponding to the ratio of the shedding frequencies $f_N/f_S \approx 0.5$. These estimates are in good agreement with those reported in Dunn & Tavoularis (2006) based on flow visualization experiments for the matching Reynolds number and D/d.

As seen in Fig. 5.10, the difference in vortex shedding frequencies of the N-cell and the L-cell vortices results in vortex interactions at the N-L cell boundary. Each L-cell vortex forms a direct connection across the cell boundary with one N-cell vortex (Fig. 5.10). However, in the entire N-cell cycle, there are less N-cell vortices than L-cell vortices, e.g., 14 N-cell vortices and 16 L-cell vortices for $Re_D = 150$ (Fig. 5.10). As N-cell vortices gradually move out of phase with their L-cell counterparts, a vortex dislocation occurs. In fact, unlike dislocations at the N-S boundary, such a dislocation is accompanied by significant fluctuations of the N-L cell boundary position and the associated changes in the spanwise extent of the N-cell. The process of phase readjustment involves complex vortex connections and continues over more than one L-cell vortex shedding cycle. For example, four consecutive L-cell vortices (L5, L6, L7, and L8) form vortex connections with two N-cell vortices (N5 and N6) in Figs. 5.10b and 5.10c. Each of the four L-cell vortices splits into at least two vortex filaments, forming a half-loop vortex connection with a subsequent L-cell vortex and a direct connection with an N-cell vortex. Eventually, L-cell vortices re-align in phase with N-cell vortices (Fig. 5.10e), and direct cross boundary vortex connections are observed at the N-L cell boundary until the next vortex dislocation occurs. During the period of an N-cell cycle (T_N), the difference in the number of shed L-cell vortices and N-cell vortices is $2T_N(f_L - f_N)$, which equals to two vortices for $Re_D = 150$ (e.g., Fig. 5.10). Consequently, the frequency of the N-cell cycle ($1/T_N$) can be estimated as the beat frequency ($f_L - f_N$), which is also the frequency of vortex dislocations occurring at the N-L cell boundary. The numerical results for $Re_D = 300$ showed a similar cyclic N-cell development and the main cross-cell vortex connections occurring during dislocations at the N-L cell boundary. However, as was seen at the N-S cell boundary, the development of

small-scale streamwise vortices result in more complex and weaker cross-boundary connections for $Re_D = 300$.

It should be noted that, assuming a constant rate of vorticity production along the span of the large cylinder, N-cell vortices are expected to have slightly higher strength than their L-cell counterparts for both Reynolds numbers investigated. Therefore, in order to account for this, weak cross-boundary or half-loop N-cell vortex connections may persist throughout each N-cell vortex shedding cycle but would be difficult to identify either numerically or experimentally due to their relatively low strength.

Frequency analysis

To investigate further the development of the identified vortex cells, spectral analysis of streamwise velocity data was performed. The obtained streamwise (E_{uu}) velocity spectra for $Re_D = 150$ and $Re_D = 300$ are presented in Figs. 5.11a and 5.11b, respectively. The results reveal three well-defined peaks in the spectra, pertaining to S-cell, N-cell and L-cell vortices. Evidently, the dominant frequency changes across the span of the step cylinder. In particular, the S-cell is the principal frequency-centred activity over the entire span of the small cylinder, with the corresponding dimensionless frequency $f_SD/U \approx 0.320$ for $Re_D = 150$ (Fig. 5.11a) and $f_SD/U \approx 0.353$ for $Re_D = 300$ (Fig. 5.11b). Near the step, at $z/D \approx -0.5$, a second peak appears in the spectra at $f_ND/U \approx 0.157$ and $f_ND/U \approx 0.168$ in Figs 5.11a and 5.11b, respectively. This new spectral peak is attributed to N-cell vortex shedding. Within a spanwise region of approximately $-1 < z/D < -0.5$, the N-cell frequency-centred activity becomes dominant, while the energy of the S-cell frequency-centred activity diminishes for both Reynolds numbers investigated. Eventually, for both Reynolds numbers, only peaks pertaining to the N-cell are detectable in the spectra for $-3.5 < z/D < -1$, supporting the earlier conclusion that there are no interruptions in N-cell vortex shedding. At $z/D \approx -3.5$,

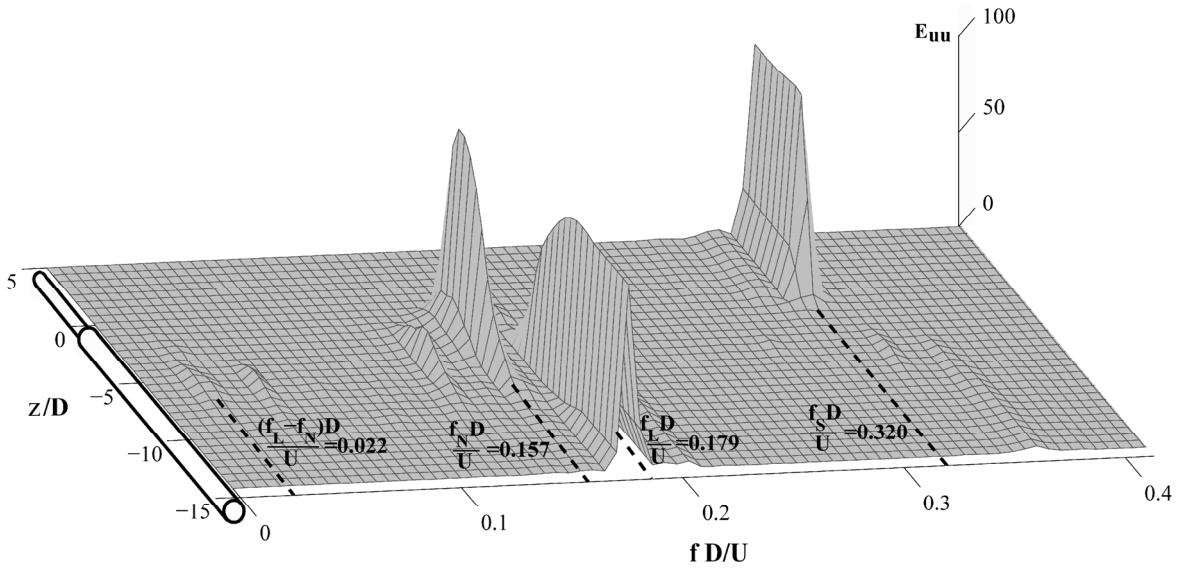

(a) $Re_D = 150$

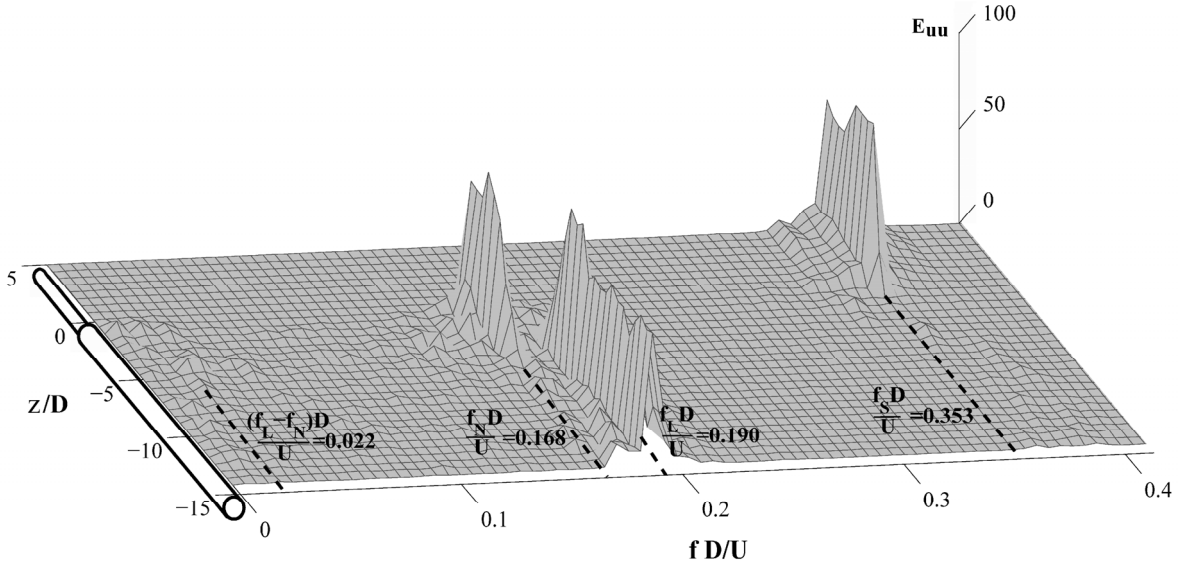

(b) $Re_D = 300$

Figure 5.11 Streamwise velocity spectra for D/d = 2, x/D = 2.5, and y/D = 0.75.

another peak due to L-cell vortex shedding appears in the spectrum at $f_L D/U \approx 0.179$ for $Re_D = 150$ and at $f_L D/U \approx 0.190$ for $Re_D = 300$. The L-cell becomes dominant at and beyond $z/D \approx -4.5$, while the energy of the N-cell peaks gradually diminishes. Finally, away from the step, only peaks attributed to L-cell vortices remain in the spectra for both Reynolds

numbers. Comparing Figs. 5.11a and 5.11b, it can be seen that the dominant spectral peaks are broader for $Re_D = 300$, due to random perturbation in the velocity signal caused by the passage of small-scale vortices. It should be noted that the Strouhal numbers pertaining to the S-cell and the L-cell are slightly lower than those obtained in simulations for a uniform cylinder at the corresponding Reynolds numbers (Table 3). This is due to oblique vortex shedding observed in both the S-Cell and the L-Cell (e.g., Fig. 5.10), agreeing with the results of Williamson (1989).

In addition to the dominant peaks pertaining to the main vortex cells, the results for $Re_D = 150$ (Fig. 5.11a) show smaller magnitude peaks in the spectra at frequencies corresponding to linear combinations and harmonics of the frequencies of the three vortex cells, which is commonly observed in quasi-periodic spectra associated with spanwise vortex cells (e.g., Williamson, 1989; Gerich & Eckelmann, 1982). Among these smaller peaks, one peak of particular interest is centred at the non-dimensional beat frequency $(f_L - f_N)D/U \approx 0.022$ and is located in the region $-4.0 < z/D < -6.5$, where interactions between the N-cell and L-cell vortices take place. The corresponding frequency centered activity can also be seen in the spectra for $Re_D = 300$ at $(f_L - f_N)D/U \approx 0.022$. Thus, the spectral results confirm that, at the N-L cell boundary, vortex dislocations occur periodically at the beat frequency given by $(f_L - f_N)$. The beat frequency associated with vortex dislocations at the N-S cell boundary corresponds to $(f_S - f_N)D/U \approx 0.163$ and $(f_S - f_N)D/U \approx 0.185$ for $Re_D = 150$ and 300, respectively. Being coincidentally close to the dominant peaks at $f_N D/U \approx 0.157$ for $Re_D = 150$ and $f_L D/U \approx 0.190$ for $Re_D = 300$, the corresponding frequency centered activities cannot be clearly identified in the spectra.

Figure 5.12 shows the variation of the dimensionless vortex shedding frequency across the span of the step cylinder for Re_D = 150 and 300. At a given z/D location, each data point in Fig. 5.12 corresponds to the frequency of a spectral peak with the energy content of at least 10% of the largest peak observed in the spectra at this z/D location. For each Reynolds number, two transition regions along the span of the cylinder can be identified: (i) for $-1 \leq z/D \leq -0.5$, S-cell and N-cell vortices may exist and (ii) for $-6.5 \leq z/D \leq -3.5$, N-cell and L-cell vortices may exist. These two regions roughly identify the spanwise extent of variation in the position of the corresponding cell boundaries at this downstream location. Consistent with previous observations, the spanwise extent of the transition region at the N-L cell boundary is significantly larger than that of the region at the N-S cell boundary. Within the N-L transition regions, the corresponding beat frequencies are marked in Fig. 5.12. As was noted earlier, due to their proximity to the dominant shedding frequencies, frequency-centered activity associated with the beat frequency ($f_S - f_N$) could not be clearly distinguished from the peaks attributed to primary vortex shedding and, therefore, is not marked in Fig. 5.12. Nevertheless, based on the analysis of vortex interactions, vortex dislocations are expected to occur at the beat frequency ($f_S - f_N$) within the narrow transition region between the N-cell and the S-cell.

For comparison, the results of Dunn & Tavoularis (2006) and Dunn (2004) are plotted in Figs. 5.12a and 5.12b, respectively (note that the results from Dunn (2004) are equivalent to those shown in Dunn & Tavoularis (2006) but the data could be interpreted more precisely). The numerical results agree well with the experimental data, with the largest discrepancy between the corresponding frequencies not exceeding about 10%. The observed variation is similar to that often seen between data sets obtained in different experimental

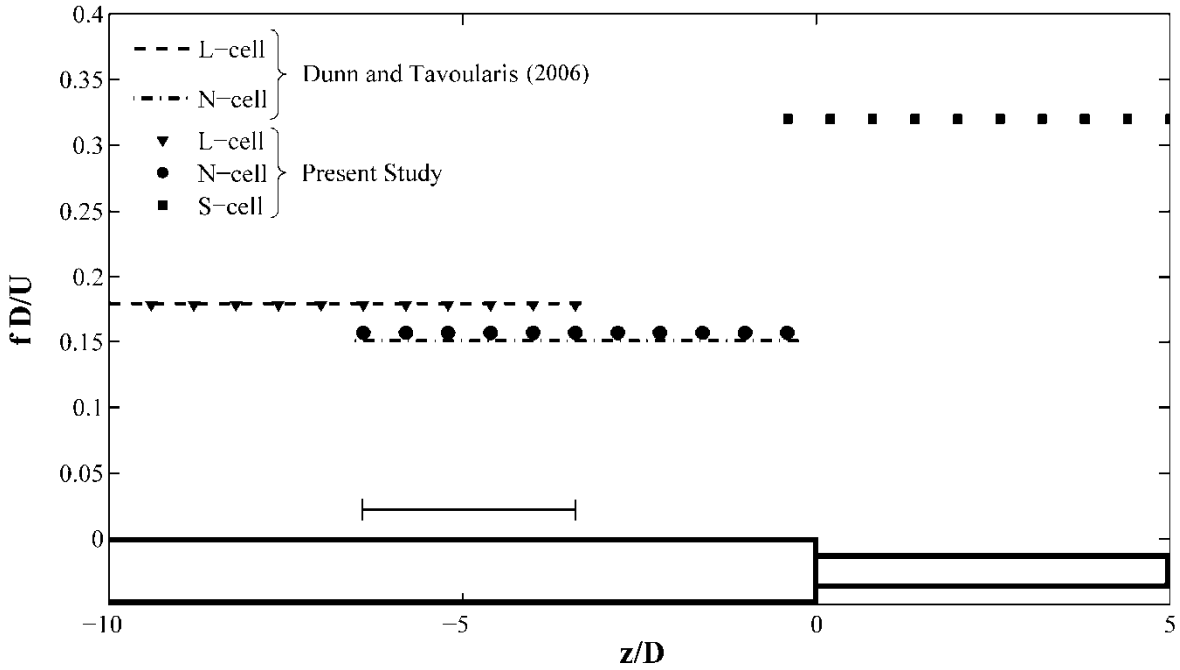

(a) $Re_D = 150$

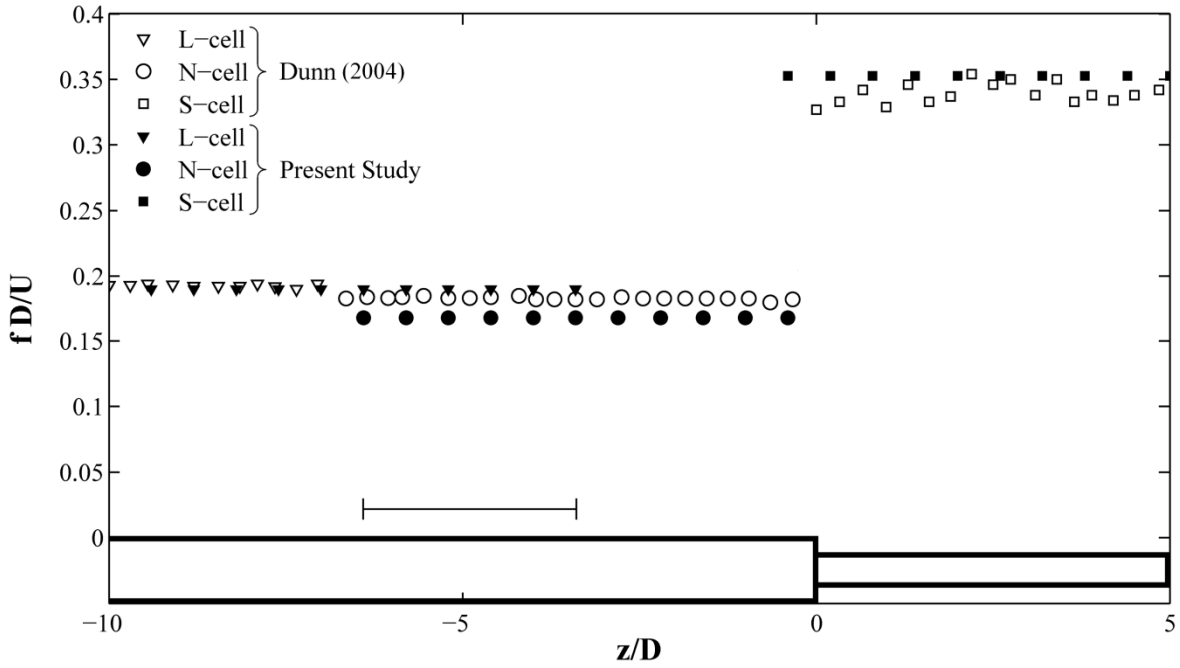

(b) $Re_D = 300$

Figure 5.12 Variation of dimensionless vortex shedding frequency across the span of a step cylinder. (a) Re_D = 150, data from Dunn & Tavoularis (2006) is based on flow visualization results for matching Re_D and D/d, (b) Re_D = 300, data from Dunn (2004) is based on LDV measurements for matching Re_D and D/d. Regions where the corresponding beat frequency is detectable in the spectra are identified by ⊢⊣.

facilities (Norberg, 2003). Indeed, a noticeable variation in cell shedding frequency can be seen comparing different data sets acquired by Dunn (2004) for a step cylinder geometry in the same experimental facility (e.g., by changing the vertical orientation of the step cylinder in the flow). It is interesting to note that the beat frequency ($f_L - f_N$) cannot be identified in the spectral results of Dunn & Tavoularis (2006) despite being detected by them from flow visualization results. This is likely due to high-pass filtering of velocity signals performed in their experiments (Dunn, 2004) to remove surface wave effects, with the wave frequency being coincidentally close to the beat frequency.

It should be noted that for Re_D = 150, Dunn & Tavoularis (2006) estimated the shedding frequencies of the N-cell and L-cell based on their flow visualization results. In contrast, for Re_D = 300, data from Dunn (2004) is based on spectral analysis of velocity measurements. In his analysis, Dunn (2004) identified only the frequency of the most dominant spectral peak at each z/D location; therefore, the presence of the discussed transition regions is not reflected in the plotted experimental data. However, such regions were identified in Dunn's experiments (Dunn & Tavoularis, 2006; Dunn, 2004), with the transition region at the N-L cell boundary spanning at least 2D.

The results shown in Figs. 5.11 and 5.12 suggest that the average spanwise extent of the N-cell does not change appreciably as the Reynolds number is increased from Re_D = 150 to Re_D = 300 despite the attendant change in the vortex shedding regime in the large cylinder wake. This helps explain the difference observed by Dunn & Tavoularis (2006) between the larger N-cell extent in their flow visualization images for Re_D = 150 compared to that estimated based on their velocity measurements for Re_D = 300. Indeed, flow visualization

provides estimates of the instantaneous extent of the N-cell; whereas, spectral results give an estimate of the average extent of the N-cell as seen at a given measurement location.

Vortex dislocations and N-cell shedding

The presented results suggest that there are no well defined boundaries between the three vortex cells. Instead, complex vortex interactions occur within transition regions, whose spanwise extent changes with both the downstream position and time. At a given downstream location, an average extent of such a region between the N-cell and the S-cell is substantially smaller than that of the region between the N-cell and the L-cell. In both regions, cross-boundary vortex connections as well as half-loop connections occur, supporting qualitative observations in Lewis & Gharib (1992) and Dunn & Tavoularis (2006). Within the N-S cell transition region, half-loop vortex connections occur between N-cell vortices and the S-cell vortices, with the latter making vortex dislocations. In contrast, half-loop connections within the N-L cell transition region were observed to occur within vortex dislocations, which were also accompanied by cross-boundary vortex connections. Moreover, the numerical results for $Re_D = 300$ show that the development of small-scale streamwise vortices complicates further vortex connections between spanwise vortex filaments. The presence of both half-loop and cross-boundary vortex connections at cell boundaries agrees with experimental observations for a step cylinder (Lewis & Gharib, 1992; Dunn & Tavoularis, 2006) and previous findings for a tapered cylinder (Narasimhamurthy et al., 2009). This differs from the observation made by Williamson (1989, 1992) that vortex dislocations on a uniform cylinder involve only cross-boundary vortex connections, which are being distorted as the dislocation is convected downstream. In light of the foregoing discussion, however, it seems that, for

various geometries and flow parameters, vortex dislocations at cell boundaries can involve 'a rather contorted tangle of vortices' (Williamson, 1989).

To elucidate temporal changes in vortex dynamics across the span of the cylinder, Figs. 5.13a-e show streamwise velocity fluctuations for Re_D = 150 acquired at five spanwise locations, three of which are within the three identified vortex cells and two are within the transitional regions between the cells. The normalized time scale corresponds to the time stamps in Fig. 5.10, which allows comparison of the results in the two figures for $0.41 < t/T_N < 1.39$. Consistent, periodic velocity fluctuations are observed in Figs. 5.13a, 5.13c, and 5.13e, attributable to vortex shedding in the S-cell, N-cell, and L-cell, respectively. As argued previously, the velocity measurements made in the core of the N-cell reveal no interruptions in the N-cell shedding (Fig. 5.13c). Clear amplitude modulations are observed in the velocity signals pertaining to the N-S cell (Fig. 5.13b) and N-L cell (Fig. 5.13d) transition regions, agreeing with the observations of Williamson (1989) made for end-cell boundaries on uniform cylinders. In Fig. 5.13b, velocity fluctuations at the S-cell shedding frequency are modulated at the beat frequency ($f_S - f_N$). Since in the present investigation the beat frequency for Re_D = 150 corresponds to about $0.5f_S$, frequent amplitude modulations are observed as vortex dislocations occur at the cell boundary (cf. Fig. 5.13b and Fig. 5.10). At the N-L cell boundary (Fig. 5.13d), the velocity signal also displays clear amplitude modulations occurring at the beat frequency ($f_L - f_N$). Since vortex dislocations take place when the vortices in the neighboring cells are shed out of phase, the resulting induced velocity fluctuations at the boundary are expected to diminish. Thus, a reduction in the amplitude of streamwise velocity fluctuations should mark the occurrence of a vortex dislocation (Williamson, 1989). Indeed, the first amplitude modulation, observed in the

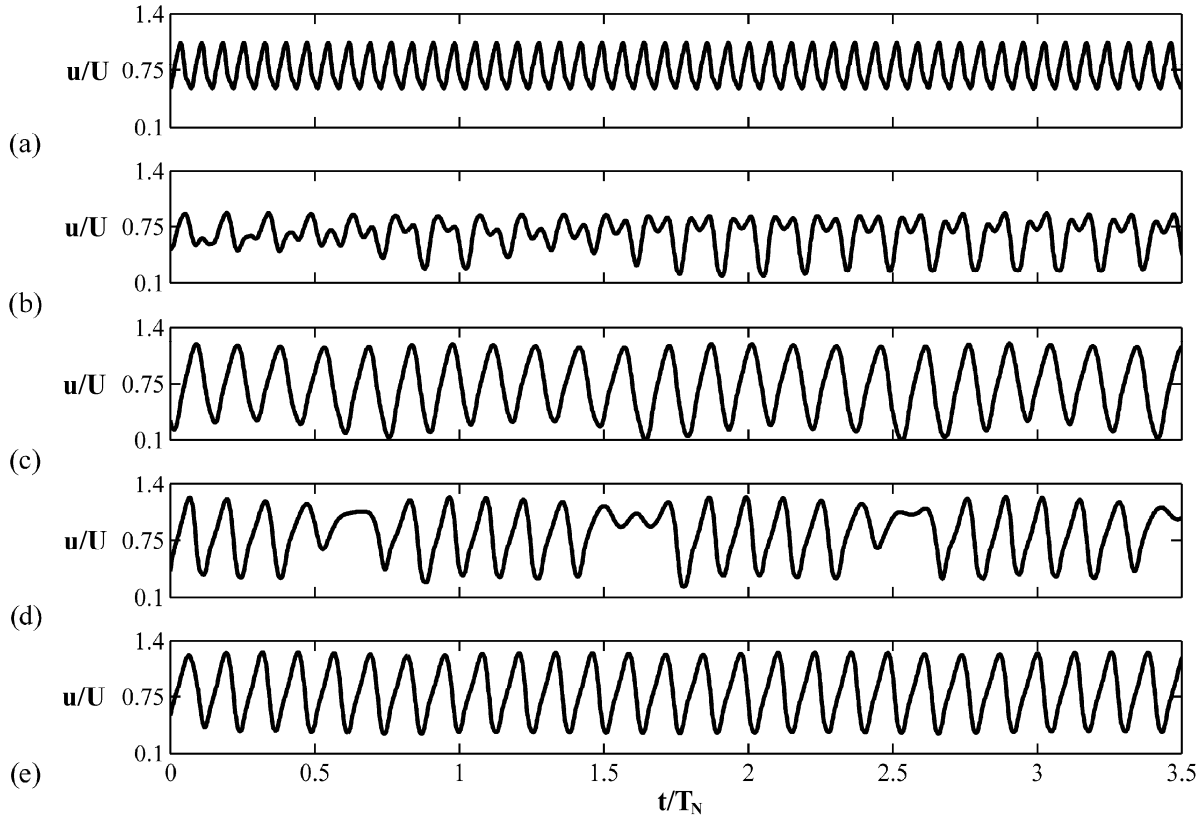

Figure 5.13 Streamwise velocity signals in the wake of a step cylinder for Re_D = 150, D/d = 2, at x/D = 2.5: (a) y/d = 0.75 and z/D = 2.6, (b) y/d = 0.75 and z/D = −0.4, (c) y/D = 0.75 and z/D = −2.2, (d) y/D = 0.75 and z/D = −5.2, and (e) y/D = 0.75 and z/D = −10.0.

signal at about $t/T_N \approx 0.65$ (Fig. 5.13d), corresponds to the passage of a vortex dislocation through the measurement plane x/D = 2.5, when vortices N7 and L7 are shed out of phase (as seen in Fig 5.10c). Subsequently, when vortices N7 and L9 are shed in phase (Fig. 5.10d), velocity fluctuations similar to those observed in the L-cell are seen in Fig. 5.13d beyond $t/T_N \approx 0.75$. Similar trends were observed for Re_D = 300, although the small-scale streamwise vortices developing in the wake of the large cylinder produced small, random perturbations in the velocity signals obtained within the N-cell, L-cell, and at cell boundaries.

The analysis of the results shows that N-cell persists in the wake but its spanwise extent fluctuates, as vortex dislocations occur at the cell boundaries. While the position of the N-S

cell boundary does not fluctuate significantly at a given downstream location, vortex dislocations within the N-L cell transition region cause significant, cyclic fluctuations in the N-cell extent at the beat frequency, $f_L - f_N$ (cf. Fig. 5.10 and Fig. 5.13d). However, the mechanism responsible for the N-cell formation is unclear at this point. Dunn & Tavoularis (2006) speculate that the N-cell formation is associated with the downwash at the step, similar to the formation of a low frequency cell near the tip of a free-end cylinder (Zdravkovich, 1989). To investigate a possible link between the N-cell cycle and the downwash at the step, Figs. 5.14a and 5.14b shows a variation of the spanwise velocity with time, with the results obtained in the vortex formation region at approximately the mid-span of the N-cell. The results reveal that there is indeed a substantial downwash (i.e., negative w) in the N-cell formation region, with the mean velocity $\overline{w}/U \approx -0.17$ for $Re_D = 150$ (Fig. 5.14a) and $\overline{w}/U \approx -0.26$ for $Re_D = 300$ (Fig. 5.14b). The increase in the Reynolds number is accompanied by the increase in the downwash and the increase in amplitude of high frequency fluctuations, likely linked to the development of streamwise vortices (Williamson, 1996b). However, for both Reynolds numbers, the fluctuations of spanwise velocity appear to have a significant low frequency component. The corresponding velocity spectra (Fig. 5.15) show that the low frequency fluctuations produce a dominant peak centered at the beat frequency ($f_L - f_N$), i.e., the frequency of occurrence of vortex dislocations at the N-L cell boundary which causes cyclic fluctuations in the spanwise extent of the N-cell. Indeed, it can be seen from a comparison of Figs. 5.14a and 5.13d that each decrease in downwash velocity, e.g., for $0.4 < t/T_N < 0.8$, corresponds to a vortex dislocation developing at the N-L cell boundary. Similar to the trend observed in the streamwise velocity signals, this is also accompanied by the modulation of the high frequency fluctuations in the spanwise velocity.

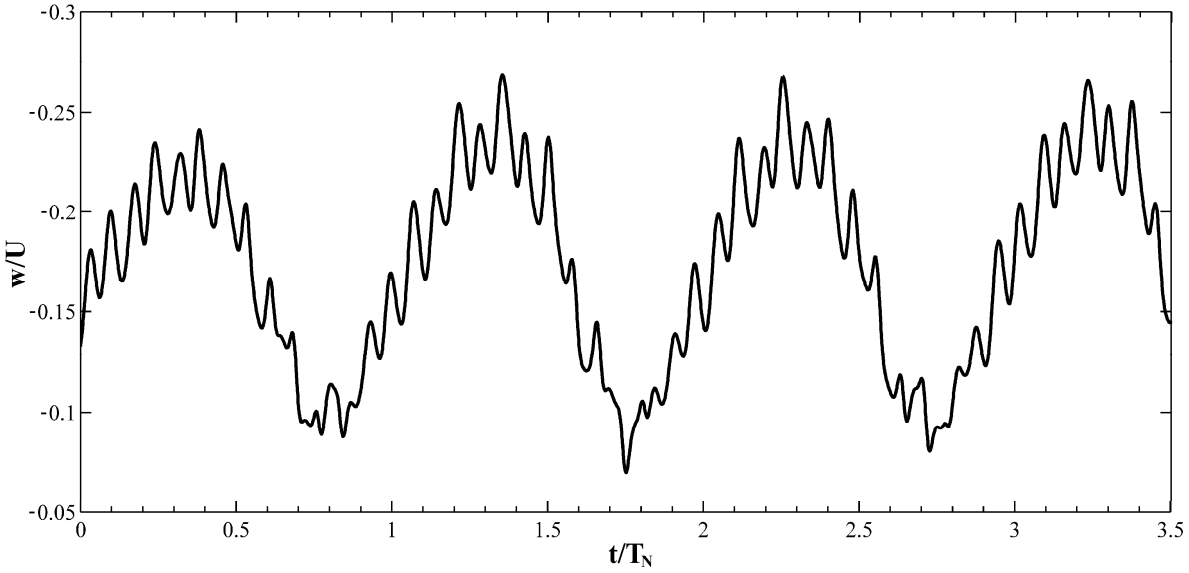

(a) $Re_D = 150$

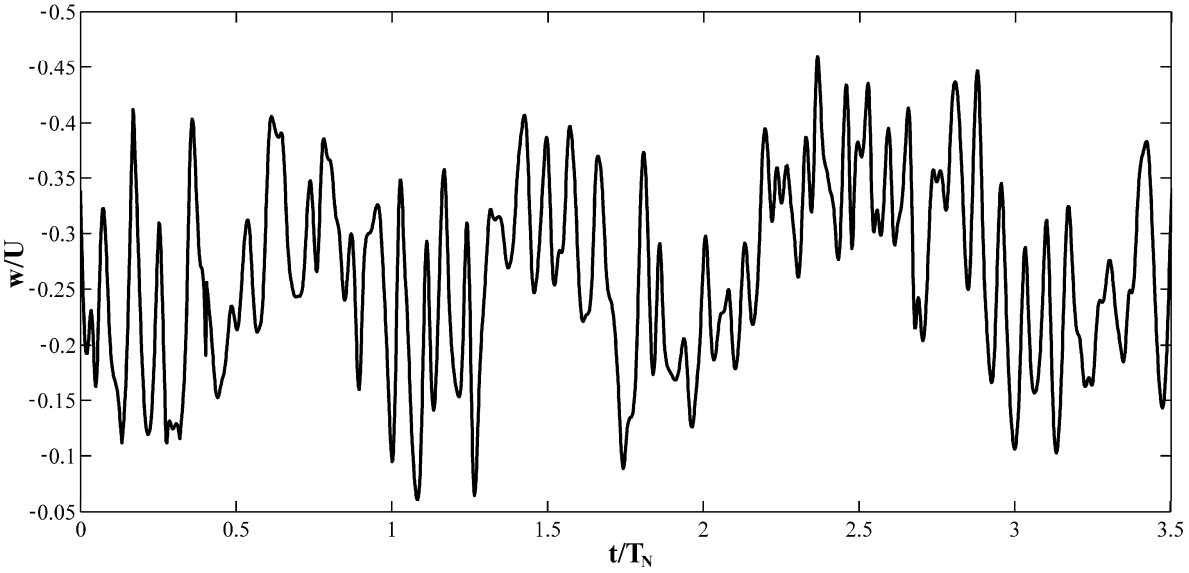

(b) $Re_D = 300$

Figure 5.14 Spanwise velocity component signals within the N-cell formation region at y/D = 0, and z/D = −2.5 for: (a) Re_D = 150 at x/D = 1.0, and (b) Re_D = 300 at x/D = 0.75.

Following a vortex dislocation, the downwash velocity gradually increases (e.g., for $0.8 < t/T_N < 1.4$), as the regular N-cell vortex shedding occurs. The observed trends can be supported further by comparing Figs. 5.14a and 5.10. Thus, the results not only establish the presence of the downwash within the N-cell formation region but also show that the N-cell

vortex dynamics is linked to the fluctuations in the downwash velocity. This quantitatively confirms the speculation of Dunn & Tavoularis (2006) that the downwash velocity may play a significant role in the formation of the N-cell. Similar to the case of a free-end cylinder (Zdravkovich, 1989), the downwash over the step may affect vortex formation near the step on the large cylinder side, causing the formation of a low frequency cell, i.e., the N-cell, in the affected region.

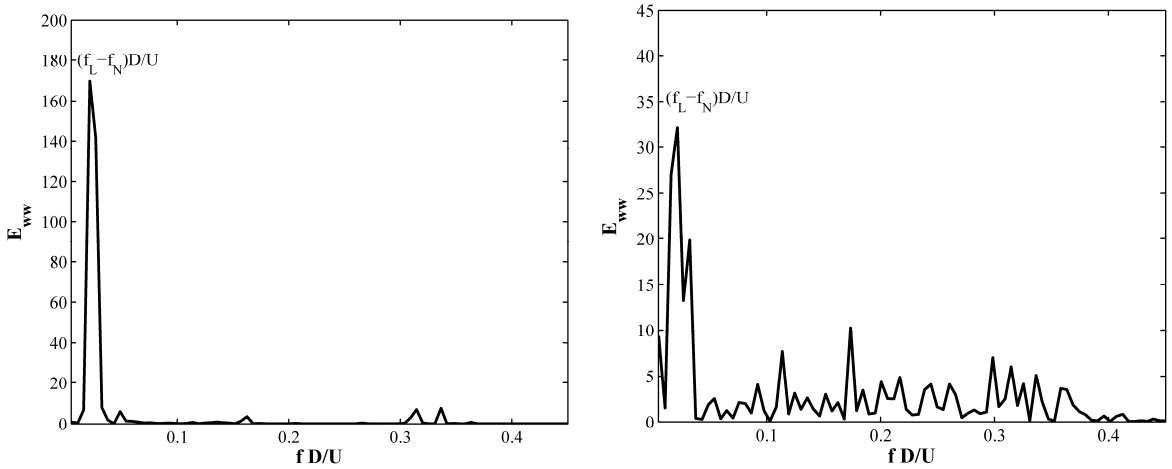

(a) $Re_D = 150$ (b) $Re_D = 300$

Figure 5.15 Spectrum of the fluctuating spanwise velocity component at y/D = 0, and z/D = −2.5 for: (a) $Re_D = 150$ at x/D = 1.0, and (b) $Re_D = 300$ at x/D = 0.75.

5.2.2 Flow past a single step cylinder for $Re_D = 1050$

Experimental results

The flow development over a step cylinder for $Re_D = 1050$ is illustrated in Figs. 5.16a-e with a sequence of hydrogen bubble flow visualization images. Similar to experimental results by Lewis & Gharib (1992), Dunn & Tavoularis (2006), and the numerical results presented in the section 5.2.1, three distinct spanwise vortex shedding cells can be identified in the wake of the step cylinder for $Re_D = 1050$: (i) the S-cell, vortex shedding from the small

cylinder, (ii) the L-cell, vortex shedding from the large cylinder, and (iii) the N-cell, which appears cyclically near the step on the large cylinder side, e.g., $-7 \leq z/D \leq 0$.

To investigate the N-cell development, it is instructive to focus on the wake of the large cylinder. Figure 5.16a shows nearly parallel vortex shedding in the wake of the large cylinder. Over time, vortices in the large cylinder wake become inclined towards the step (Fig. 5.16b). Eventually, a distinct vortex shedding cell (N-cell) can be observed near the step (Fig. 5.16c), which is bordered by the large and small cylinder vortices below and above, respectively. The N-cell vortices continue to move out of phase with the L-cell vortices until a vortex dislocation occurs, for example, the L-cell vortex at $x/D \approx 5$ in Fig. 5.16d maintains a weak connection with its counterpart in the N-cell, while the N-cell vortex connects primarily to the upstream L-cell vortex at $x/D \approx 2.5$. The N-cell vortices re-align in phase with the large cylinder vortices (Fig. 5.16e), and the N-cell becomes difficult to distinguish from the L-cell via flow visualization. In Fig. 5.16e, vortex shedding in the large cylinder wake occurs at an angle away from the step; however, after a few shedding cycles, the spanwise vortices are again shed parallel with the cylinder axis, marking the beginning of the next N-cell cycle. Despite the presence of three-dimensional structures in the step cylinder wake, the results suggest that the N-cell development agrees qualitatively with that observed in the laminar shedding regime (section 5.2.1).

Due to the difference in shedding frequencies between adjacent vortex cells, vortex dislocations occur at the cell boundaries, resulting in intricate vortex connections. It should be noted that vortex dislocations cause the locations of the cell boundaries to fluctuate with time. Near each endplate, a low frequency vortex shedding cell was observed, similar to the end cells observed for uniform cylinders. These cells are referred to as: (i) the ES-cell, vortex

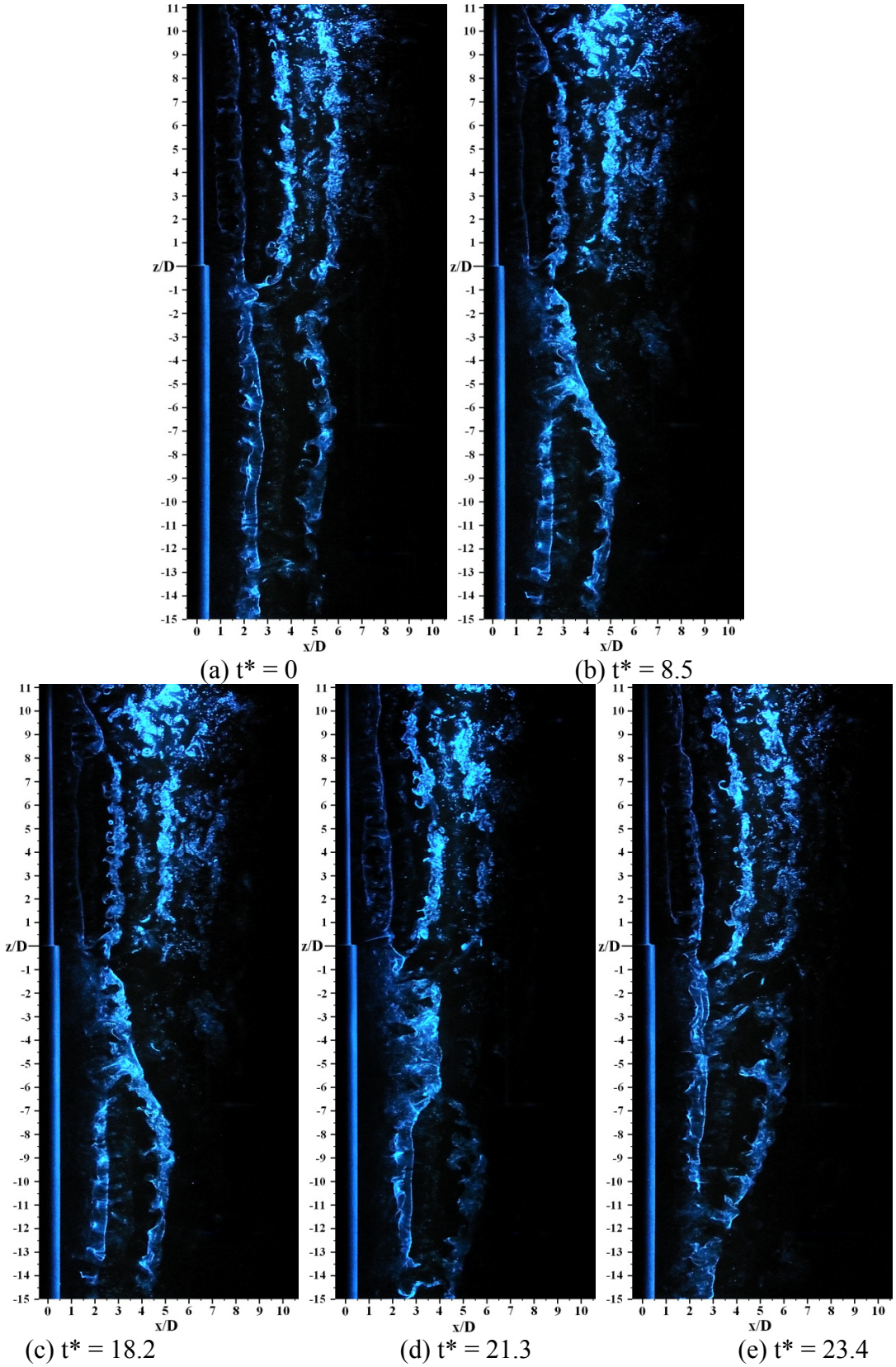

(a) t* = 0 (b) t* = 8.5

(c) t* = 18.2 (d) t* = 21.3 (e) t* = 23.4

Figure 5.16 Vortex shedding in the step cylinder wake.

shedding near the small cylinder boundary, and (ii) the EL-cell, vortex shedding near the large cylinder boundary.

Estimations of the shedding frequency for each vortex shedding cell are shown in Fig. 5.17, where the maximum observed spanwise extent of each cell is identified. The shedding frequencies were estimated based on an analysis of video records capturing over 500 L-cell shedding cycles. Based on the results presented in Fig. 5.17, the following transition regions between distinct cells along the span of the cylinder can be identified at a given downstream location: (i) the S-ES cell boundary, (ii) the N-S cell boundary, (iii) the N-L cell boundary, and (iv) the L-EL cell boundary. Within these transition regions, vortex splitting occurs, resulting in intricate vortex connections. At the N-S cell boundary, S-cell vortices often form direct vortex connections with N-cell vortices (Fig. 5.16a). The analysis of video records revealed that the remaining S-cell vortices form half-loop connections with vortices shed on the opposite side of the wake, agreeing with the results presented in section 5.2.1. Due to this, the S-cell vortices are oriented in the streamwise direction near the step (Fig. 5.16e). At the N-L cell boundary, N-cell vortices frequently form direct connections with L-cell vortices (Fig. 5.16b). However, when N-cell vortices are out of phase with L-cell vortices, they split into at least two vortex filaments, forming vortex connections with two consecutive L-cell vortices on the same side of the wake (Fig. 5.16c and 5.16d).

Changes in the vortex shedding pattern along the span of the step cylinder are depicted in Fig. 5.18. The flow visualization images presented illustrate typical flow patterns seen within the S-cell (Fig. 5.18b), the N-S cell boundary (Fig. 5.18c), the N-cell (Fig. 5.18d), the N-L cell boundary (Fig. 5.18e), and the L-cell (Fig. 5.18f). Periodic vortex shedding, similar to that observed for uniform cylinders, is seen within the S-cell, N-cell, and L-cell (Figs.

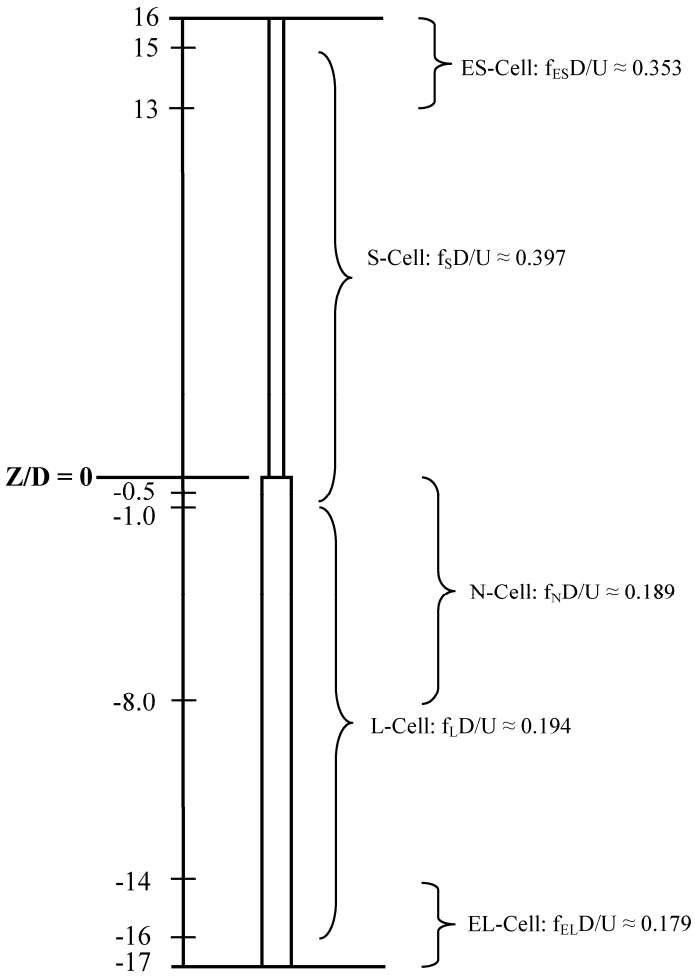

Figure 5.17 Dimensionless vortex shedding frequency across the span.

5.18b, 5.18d, and 5.18f). In contrast, at the cell boundaries, vortex interactions result in a dramatically different pattern (Figs. 5.18c and 5.18e).

Variations in vortex shedding pattern at the N-S cell boundary are illustrated in Figs. 5.19a and 5.19b, showing two images captured at the same spanwise location, z/D = -0.5, but at different instances in the shedding cycle. In Fig. 5.19a and 5.19b, S-cell vortices can be seen for $x/D \geq 2$ and $x/D \geq 4$, respectively. On the other hand, N-cell vortices appear in Fig. 5.19a for $x/D < 2$, while more complex flow structures characteristic of the N-S cell boundary can be seen in Fig. 5.19b for $x/D < 4$. The observed changes in the vortex shedding

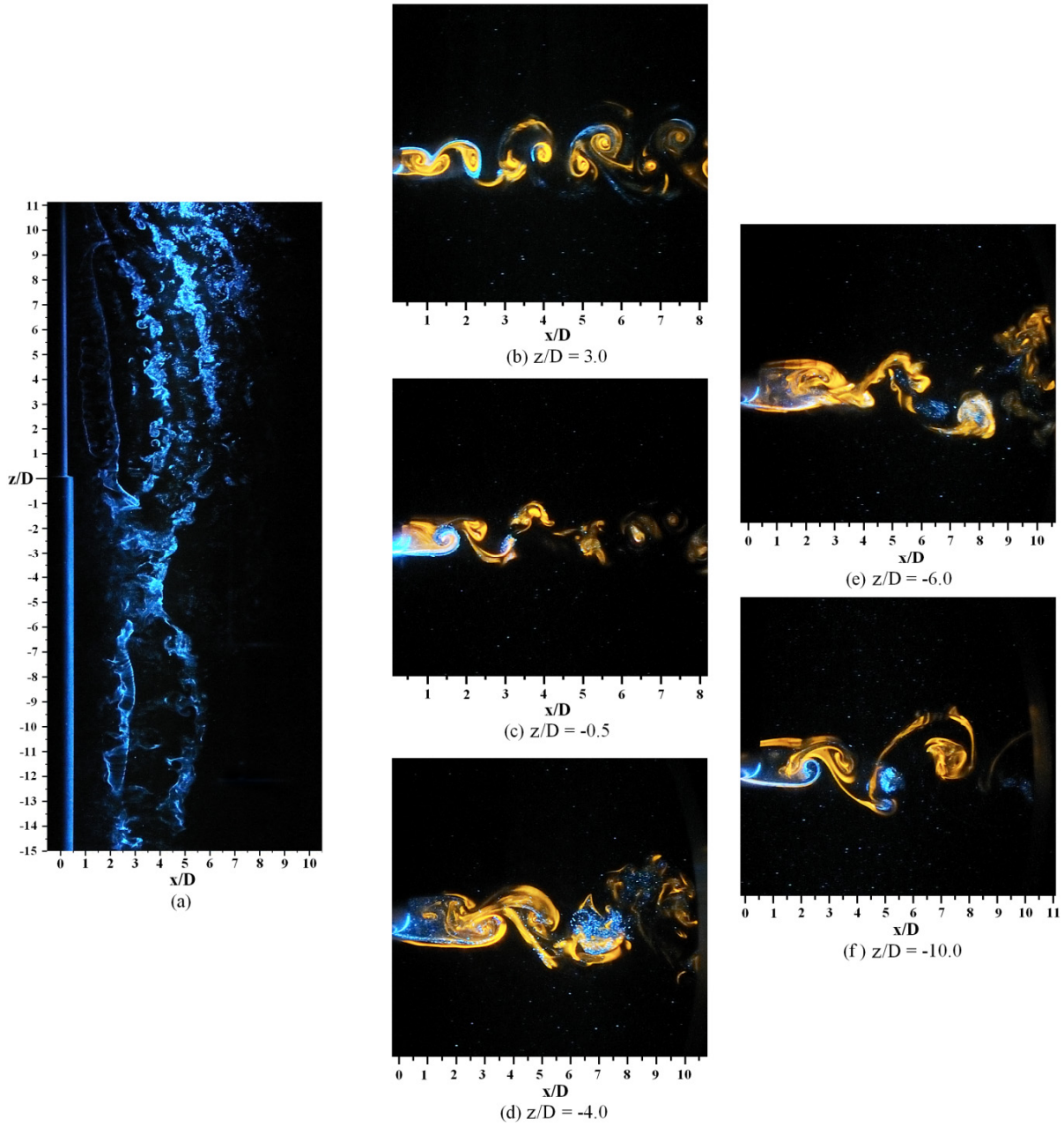

Figure 5.18 Vortex shedding patterns at different locations along the span.

pattern occur frequently, suggesting that the location of the N-S cell boundary fluctuates rapidly. Such fluctuations are attributed to vortex dislocations, which are expected to occur at a frequency of (f_S-f_N) at the N-S cell boundary (section 5.2.1). In addition, low frequency downwash fluctuations, that have been shown to be linked to the N-cell development, may also play a role (section 5.2.1).

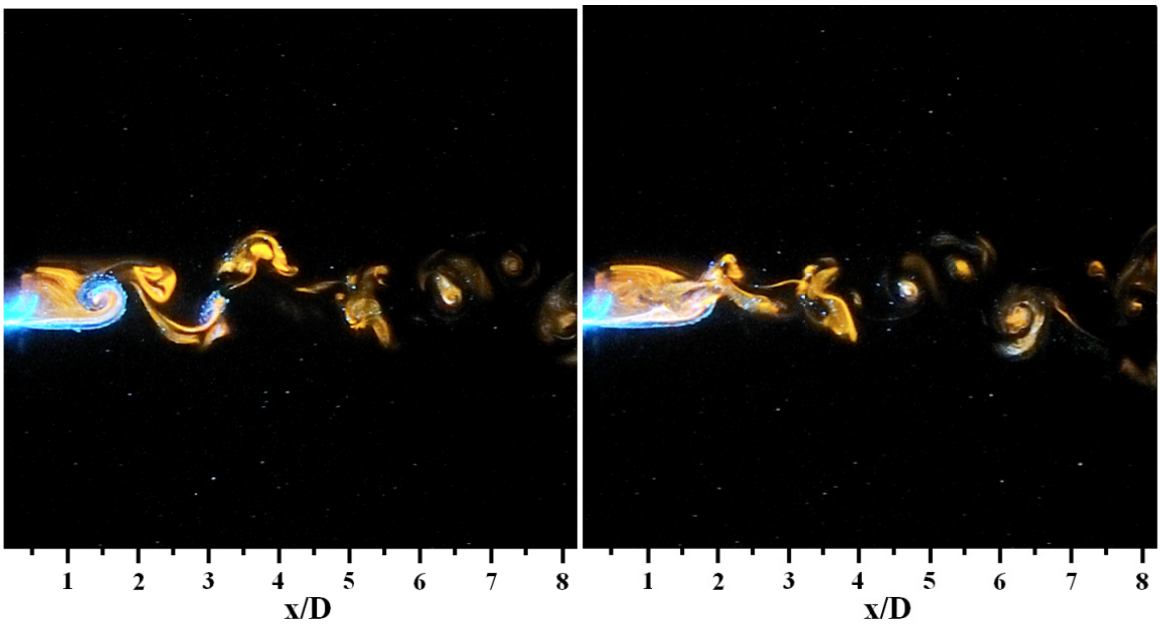

(a) t* = 0 (b) t* = 2.3

Figure 5.19 Changes in the vortex shedding pattern at the N-S cell boundary.

A sequence of images in Fig. 5.20 illustrates the presence of a downwash over the step and a strong three-dimensionality of the flow in this region. Here, dye was illuminated with a laser sheet oriented in the x-z plane near the wake centre line. The images show dye being entrained into the large cylinder wake, visualizing rather intricate small-scale, three-dimensional structures. Such structures are likely forming due to the interaction of streamwise and spanwise vortices downstream of the step.

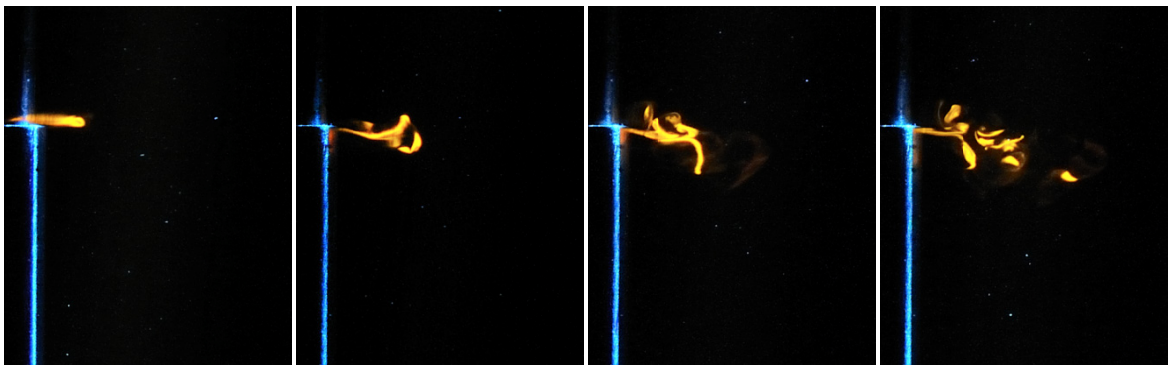

(a) t* = 0 (b) t* = 0.19 (c) t* = 0.37 (d) t* = 0.56

Figure 5.20 Presence of downwash at the step.

SST-DES results for $Re_D = 1050$

SST-DES results have been computed for several L-cell vortex shedding cycles after steady state vortex shedding was established in the simulations. To facilitate a comparison between the numerical and experimental results, Fig. 5.21a shows contours of total vorticity magnitude in the x-z plane whose y/D location matches the position of the laser sheet used in the hydrogen bubble flow visualization experiments (Fig. 5.21b). The instantaneous image in Fig. 5.21a was selected to approximately match the shedding cycle phase of the results in Fig. 5.21b. In agreement with the flow visualization image, three distinct vortex shedding cells can be identified in Fig. 5.21a: the N-cell ($-4.5 \leq z/D \leq 0$), the L-cell ($z/D \leq -5$), and the

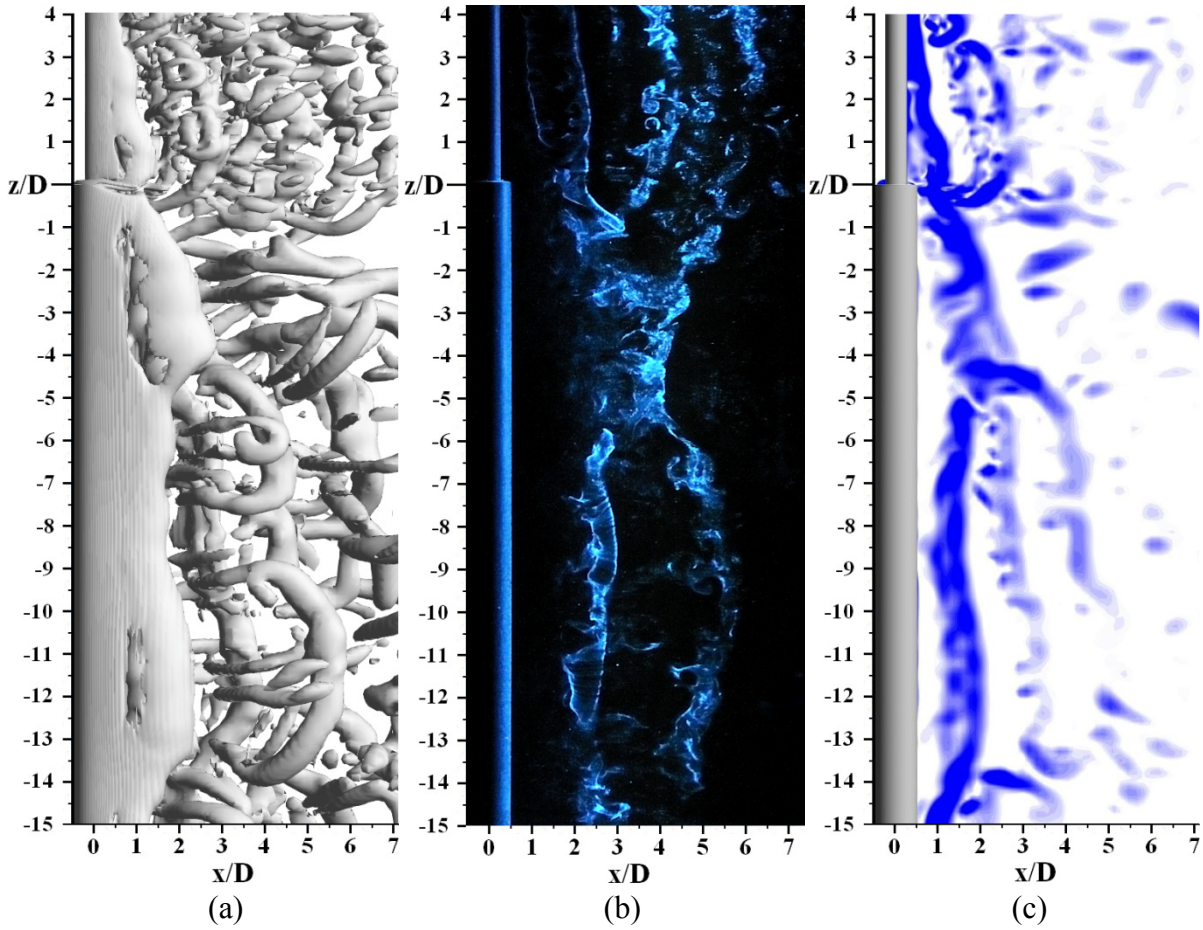

Figure 5.21 Vortex shedding in the wake of a single step cylinder: (a) isosurfaces of Q ≈ $2x10^{-1}$, (b) hydrogen bubble flow visualization image, and (c) contours of total vorticity. The legend for part (c) of the figure can be seen in Fig. 5.22.

S-cell ($z/D \geq 0$). Three L-cell vortices can be identified for $z/D \leq -5$ in the large cylinder wake, with vortices at $x/D \approx 1.5$ and $x/D \approx 4.5$ being of the same sign (Fig. 5.21a). It can be seen that the N-cell vortex, located within $-4.5 \leq z/D \leq 0$ and $x/D \approx 2$, is split into at least two vortex filaments, and forms direct vortex connections with two L-cell vortices of the same sign. The vortex connections and locations of the cell boundaries are in good agreement with the flow visualization results presented in Fig. 5.21b.

A three-dimensional visualization of the flow is shown in Fig. 5.21c. Similar to the experimental results presented in Fig. 5.16, the numerical results reveal the formation of streamwise vortices. In contrast to previous investigations on this geometry performed in the laminar regime (Valles et al., 2002; section 5.2.1) the presence of such structures dramatically changes the flow topology, significantly complicating vortex interactions taking place between the neighboring spanwise vortex cells.

Changes in the vortex shedding pattern along the span of the step cylinder are depicted in Fig. 5.22, which shows contours of total vorticity in several x-y planes. The images were captured at the same time as the results presented in Figs. 5.21a and 5.21c, approximately corresponding to the same phase in the N-cell cycle as that in Fig. 5.18a. Comparing the images in Fig. 5.22 with the corresponding images in Fig. 5.18, there is good agreement between numerical and experimental results within each cell and at the cell boundaries. The presented numerical results suggest that DES can be employed to gain added insight into the 3D flow topology, which is difficult to characterize using experimental methods.

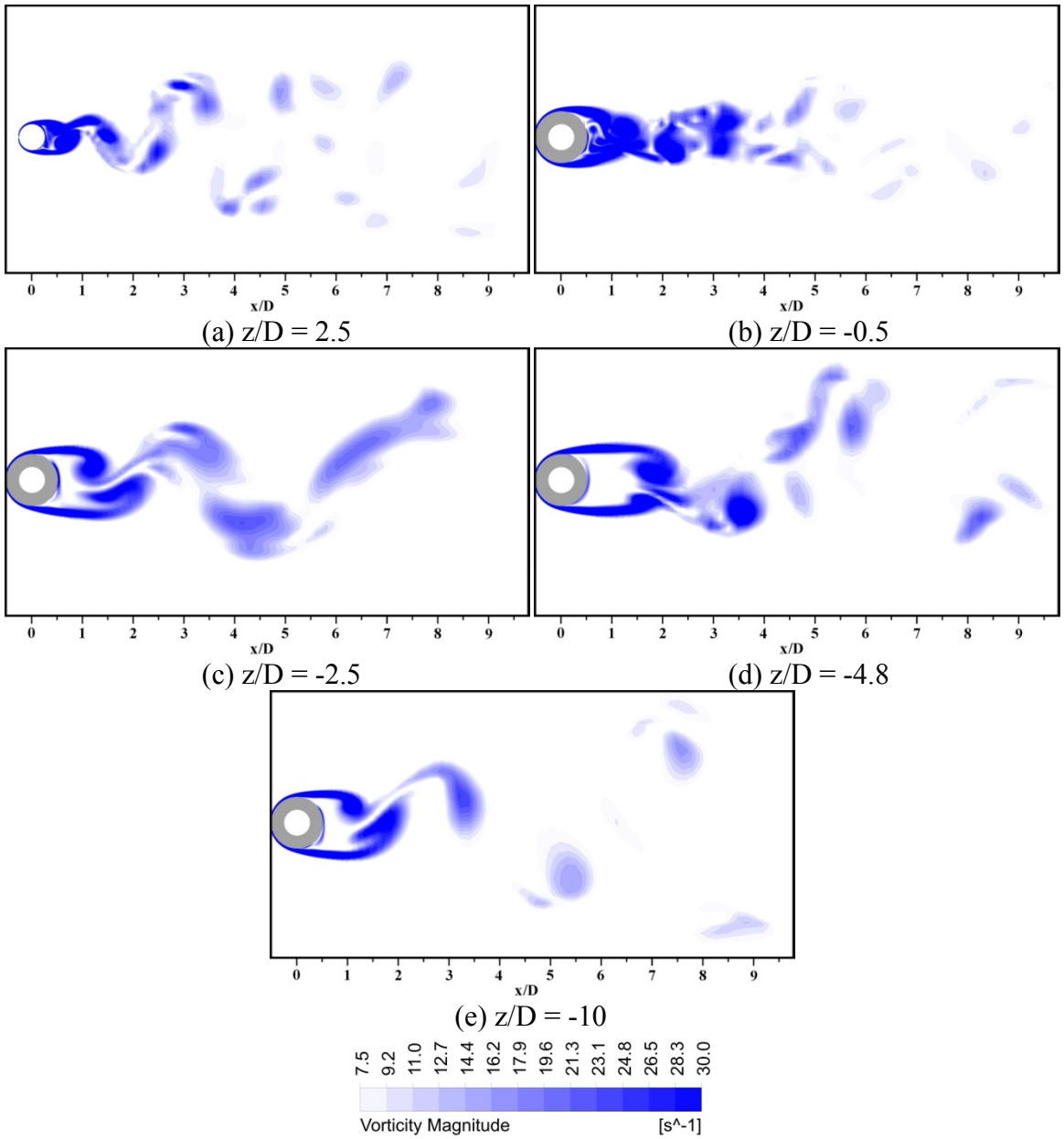

Figure 5.22 Variations in vortex shedding patterns at different spanwise locations in the wake of a single step cylinder.

5.3 Discussion

The flow development in the wake of a single step cylinder has been studied for a fixed diameter ratio, D/d = 2, and three Reynolds numbers, Re_D = 150, 300, and 1050. The results show N-cell formation in the wake of a step cylinder for all Reynolds numbers investigated. For all Reynolds numbers studied, each N-cell vortex forms vortex connections with two other adjacent vortex cells: the S-cell and the L-cell. The vortex connections become more complicated at Re_D = 300 and 1050 due to the presence of streamwise vortices in the wake, but this does not seem to alter the overall N-cell development.

It is of interest to investigate the effect of the Reynolds number on flow characteristics. It can be inferred from Dunn's (2004) results that the average spanwise extent of the N-cell decreases with increasing the Reynolds number for $296 \leq Re_D \leq 621$ and D/d = 1.98. Norberg (1992), reports the same trend for $3x10^3 \leq Re_D \leq 13x10^3$ and D/d = 2. In contrast, the numerical results presented in section 5.2.1 indicate no change in the average spanwise extent of the N-cell. Table 5 facilitates a quantitative analysis between the results from Dunn (2004) and the current study. It should be noted that the extent of the N-cell shown in Fig. 5.17 (approximately 8D) is the maximum observed spanwise extent. The average span of this cell is considerably smaller and was estimated to be 3-5D based on video records (Table 5). The results in Table 5 indicate that the increase in the Reynolds number is generally accompanied by an increase in f_N/f_L. The one exception is the numerical results for Re_D = 150 and 300 which yield the same f_N/f_L ratio, indicating that this trend needs further investigation.

Table 5 N-cell experimental data.

Experimental Study	Re_D	D/d	Average N-cell extent	f_N/f_L
Current Study	150	2	5.0D	0.88
Dunn (2004)	296	1.98	6.8D	0.94
Current Study	300	2	5.0D	0.88
Dunn (2004)	621	1.98	5.6D	0.96
Current Study	1050	2	3-5D	0.97

5.4 Experiments on the flow past Dual Step Cylinders

In this section, the results and analysis of a detailed flow visualization study on a dual step cylinder (Fig. 1.2b) are presented. The flow was investigated for $Re_D = 1050$, $D/d = 2$, and $0.2 \leq L/D \leq 17$. The aspect ratio (L/D) has been found to have a profound effect on wake vortex shedding. Four distinct flow regimes have been identified and are discussed in detail in this section. It should be noted that the bounds of L/D values associated with the identified regimes provide an approximate measure of the corresponding L/D ranges. Unless specified otherwise, the main vortex shedding cells in the wake of the large and small cylinders will be referred to as the L-cell and the S-cell, respectively.

L/D = 17

The flow development over a dual step cylinder for L/D = 17 is illustrated in Fig. 5.23. Cellular vortex shedding is observed in the wake (Fig. 5.23a), with three vortex cells forming along the large cylinder span and a single vortex cell along the small cylinder. Evidently, the formation of the two distinct vortex shedding cells near the steps on the large cylinder side is similar to the N-cell formation in the wake of a single step cylinder (section 5.2). Adopting the terminology introduced for a single step cylinder by Dunn & Tavoularis (2006), the observed shedding pattern in the wake of a dual step cylinder can be classified as follows: (i)

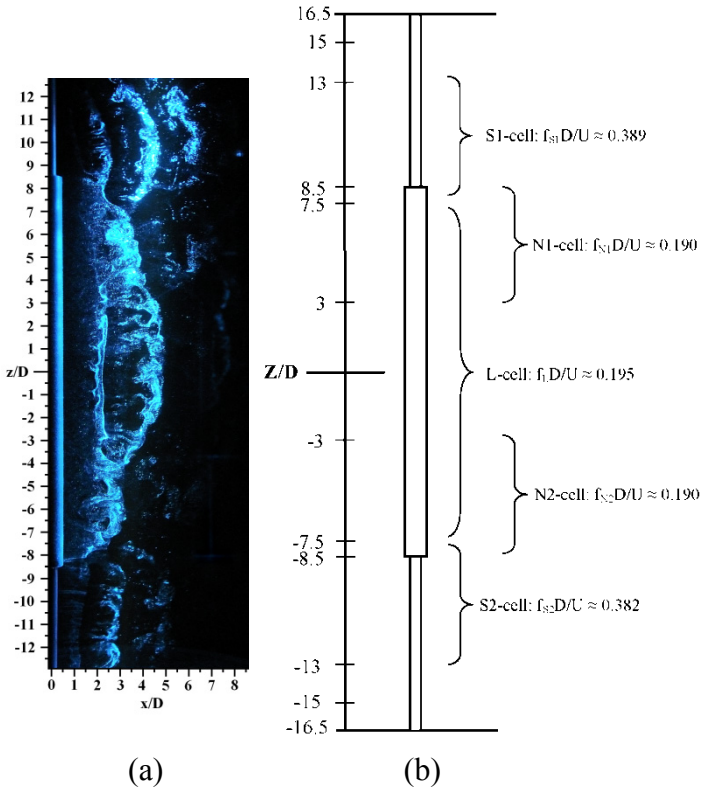

(a) (b)

Figure 5.23 Vortex shedding in the wake of a dual step cylinder for L/D = 17.

the S1-cell, vortex shedding from the small cylinder in the region $8 \leq z/D \leq 13$, (ii) the N1-cell, vortex shedding from the large cylinder in the region $3 \leq z/D \leq 8.5$, (iii) the L-cell, vortex shedding from the large cylinder in the region $-7.5 \leq z/D \leq 7.5$, (iv) the N2-cell, vortex shedding from the large cylinder in the region $-8.5 \leq z/D \leq -3$, and (v) the S2-cell, vortex shedding from the small cylinder in the region $-13 \leq z/D \leq -8$. Figure 5.23b shows an approximate maximum extent of the identified cells as well as the corresponding shedding frequencies, estimated based on an analysis of video records. It should be noted that similar to the case of a uniform cylinder, end cells were observed near the end plates but are not shown in Fig. 5.23b.

The development of vortex shedding cells in the wake of the large cylinder is illustrated by sequences of flow visualization images shown in Figs. 5.24-5.26. Figures 5.24a, 5.25a,

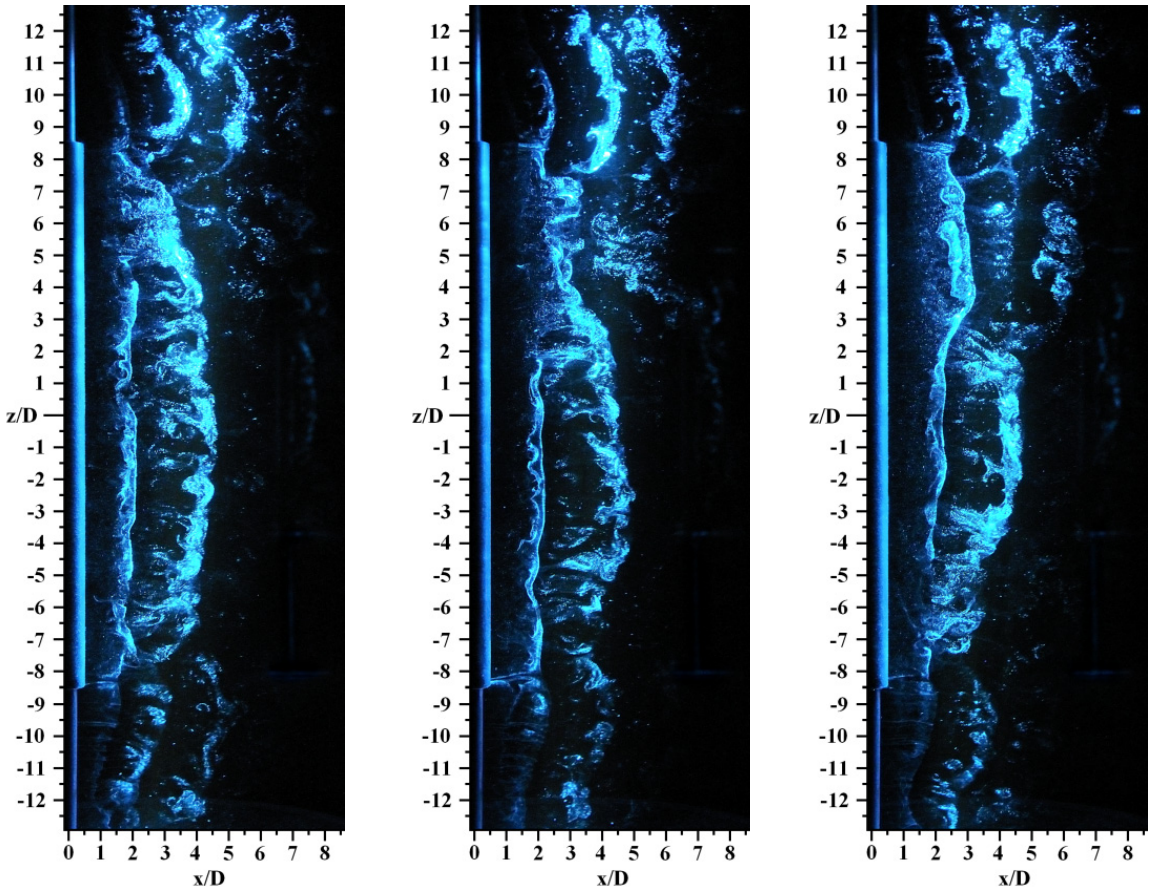

(a) t* = 0 (b) t* = 21 (c) t* = 35

Figure 5.24 N1-cell development in the wake of a dual step cylinder for L/D = 17.

and 5.26a show nearly parallel vortex shedding in the wake of the large cylinder. Over time, vortices in the large cylinder wake become inclined towards the step at z/D = 8.5 (Fig. 5.24b), at z/D = -8.5 (Fig. 5.25b), or both steps (Fig. 5.26b). Eventually, a distinct vortex shedding cell, the N1-cell and/or N2-cell (Figs. 5.24c, 5.25c, 5.26c), appears near either of the two steps. The N-cell vortices move out of phase with the L-cell vortices until a vortex dislocation occurs (e.g., z/D = 2 and x/D = 3 in Fig. 5.24c). Eventually, the N-cell vortices re-align in phase with the large cylinder vortices, and after a few L-cell shedding cycles, vortices are again shed parallel to the large cylinder axis, marking the beginning of the next N-cell cycle. An analysis of video records revealed that the cyclic development of the N1-

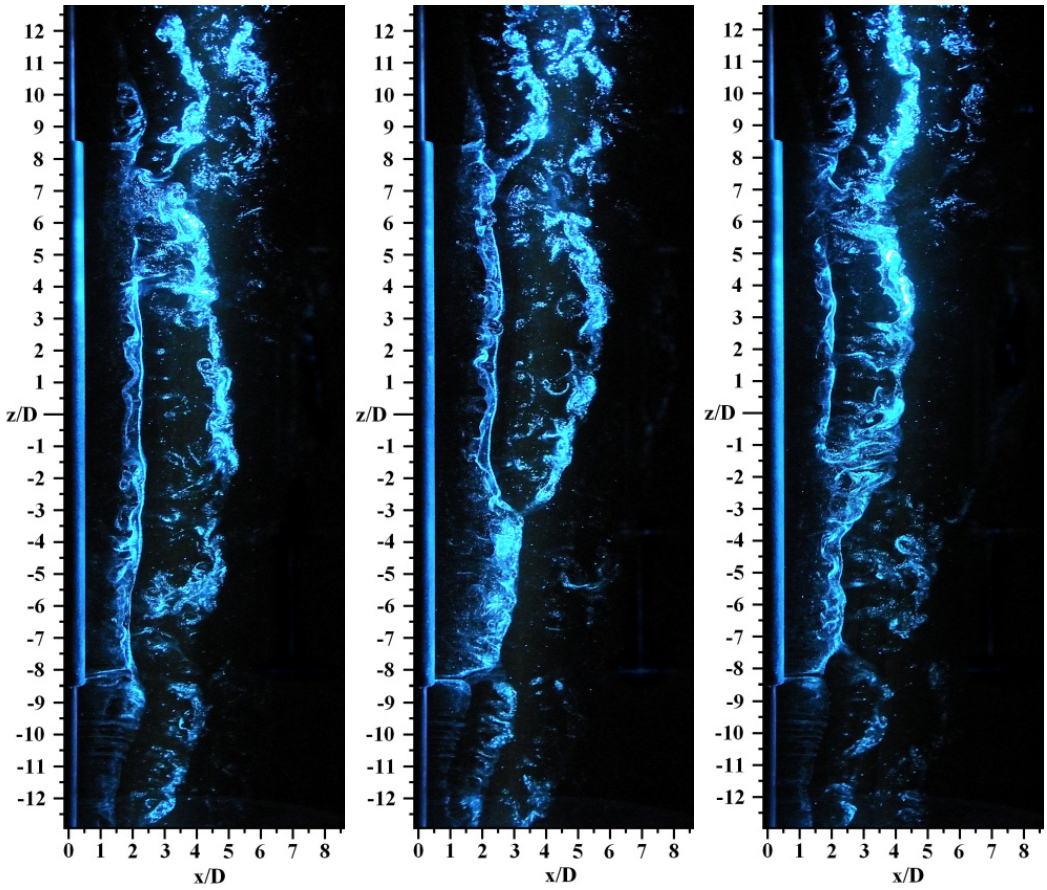

(a) t* = 0 (b) t* = 26.4 (c) t* = 37

Figure 5.25 N2-cell development in the wake of a dual step cylinder for L/D = 17.

cell (Fig. 5.24) and the N2-cell (Fig. 5.25) occurs typically in an alternating fashion. That is, an N1-cell cycle is followed by an N2-cell cycle. However, occasionally, N1 and N2 cells form simultaneously, as illustrated in Fig. 5.26. The results suggest that the flow topology in the wake of a dual step cylinder observed for L/D = 17 within z/D > 0 and z/D < 0 is similar to that observed for a single step cylinder. Moreover, for cylinders with two free ends, the numerical results of Inoue & Sakuragi (2008) show similar cellular shedding, with lower frequency cells observed near the free ends for L/D > 20. Thus, it can be speculated that the observed wake development will persist for L/D ≥ 17.

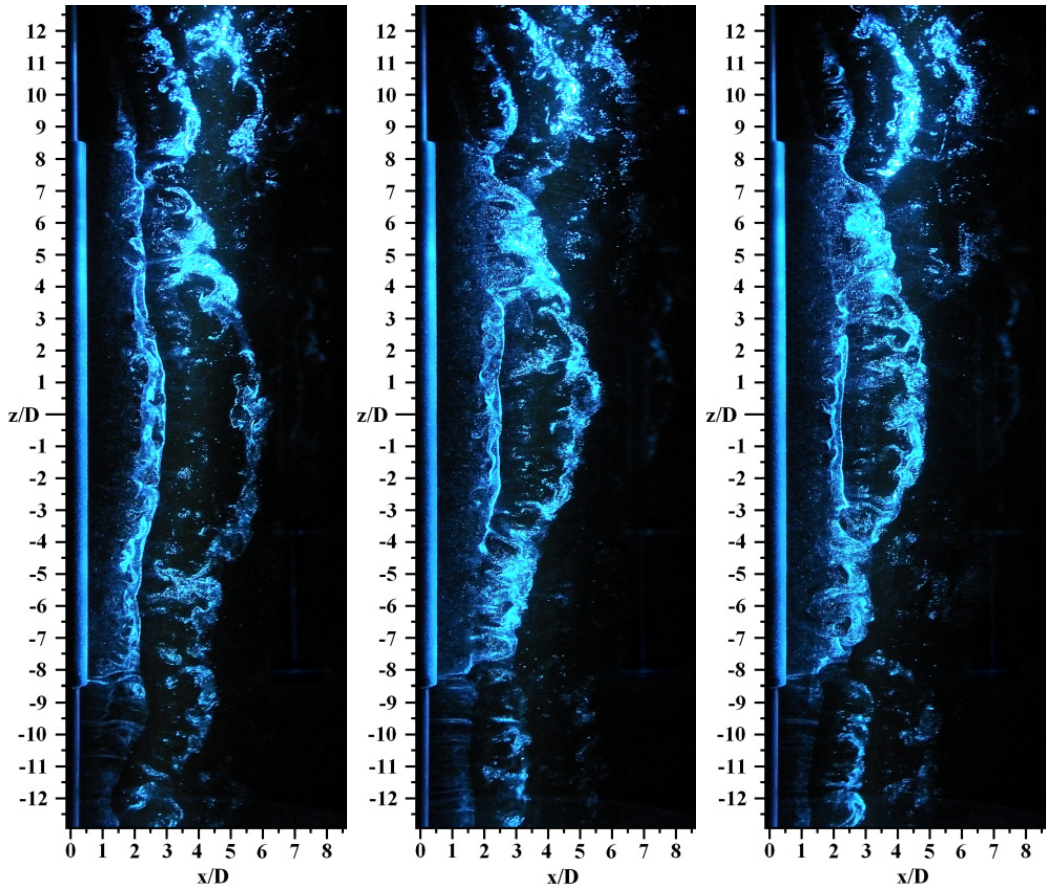

(a) t* = 0 (b) t* = 32.4 (c) t* = 39

Figure 5.26 N1 and N2-cell development in the wake of a dual step cylinder for L/D = 17.

Due to the difference in vortex shedding frequencies between adjacent vortex cells, vortex dislocations occur at cell boundaries. Based on the results presented in Fig. 5.24b, the following transition regions between distinct cells along the span of the cylinder can be identified: (i) the S1-N1 cell boundary, $7.5 \leq z/D \leq 8.5$, (ii) the N1-L cell boundary, $3 \leq z/D \leq 7.5$, (iii) the N2-L cell boundary, $-7.5 \leq z/D \leq -3.0$, and (iv) the S2-N2 cell boundary, $-8.5 \leq z/D \leq -7.5$. Within these transition regions, vortex splitting occurs, resulting in intricate vortex connections. At the S1-N1 cell boundary, S1-cell vortices often form direct vortex connections with N1-cell vortices (Fig. 5.24b). At the N1-L cell boundary, N1-cell vortices frequently form direct connections with L-cell vortices (Fig. 5.24b and 5.24c). When N1-cell

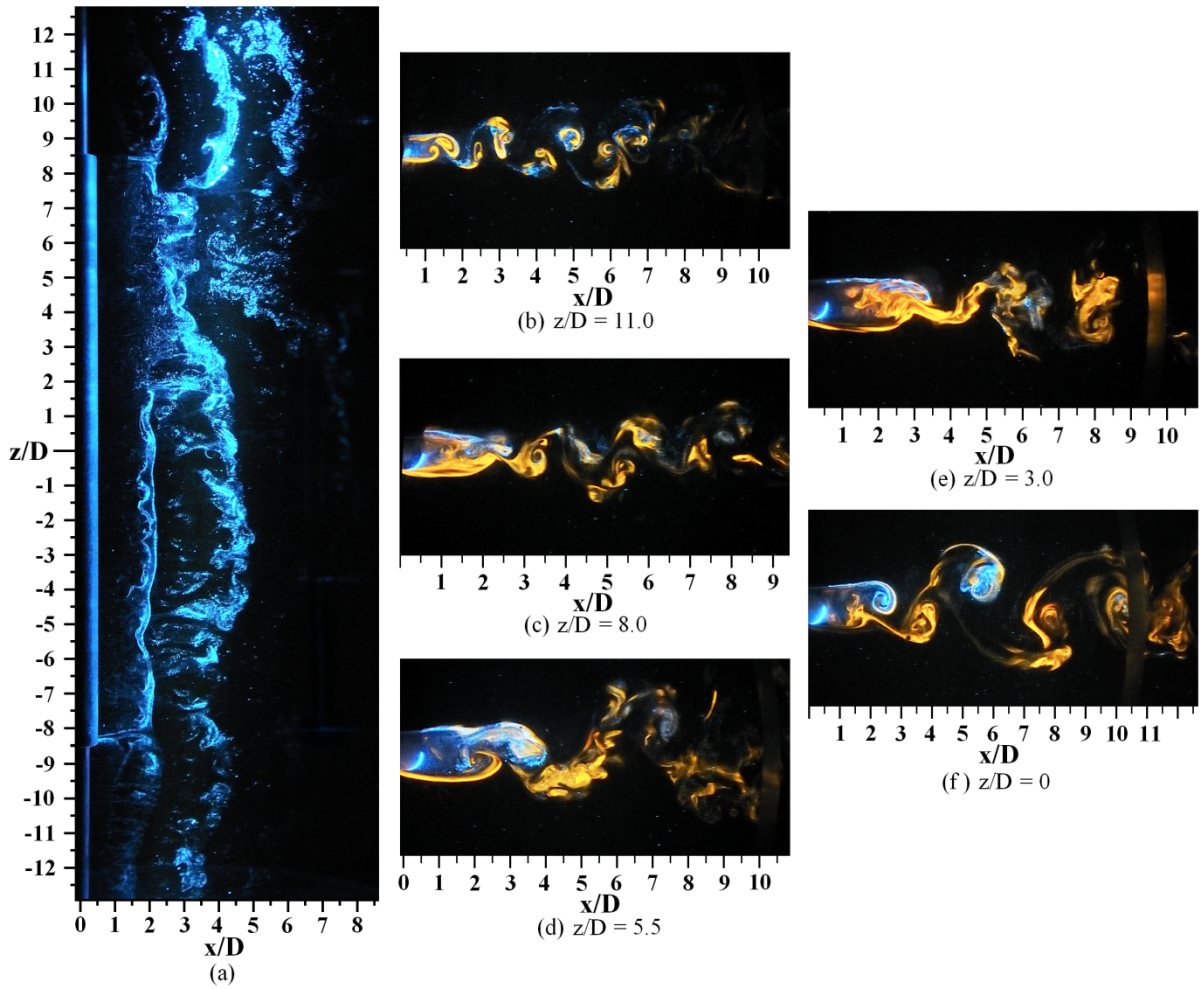

Figure 5.27 Changes in the vortex shedding pattern along the span of a dual step cylinder for L/D = 17.

vortices are out of phase with L-cell vortices, they split into at least two vortex filaments, forming vortex connections with two consecutive L-cell vortices on the same side of the wake (Fig. 5.24b and 5.24c). Similar types of vortex interactions can be seen in Figs. 5.25a-c within the N2-L and S2-N2 cell boundaries.

Changes in the vortex shedding pattern along the span of the dual step cylinder at L/D = 17 are depicted in Fig. 5.27. The flow visualization images presented for $z/D \geq 0$ illustrate typical flow patterns seen within the S1-cell (Fig. 5.27b), the S1-N1 cell boundary (Fig. 5.27c), the N1-cell (Fig. 5.27d), the N1-L cell boundary (Fig. 5.27e), and the L-cell (Fig.

5.27f). Periodic vortex shedding, similar to that observed for uniform cylinders, is seen within the S1-cell, N1-cell, and L-cell (Figs. 5.27b, 5.27d, and 5.27f). In contrast, within the cell transition regions, vortex interactions result in a dramatically different pattern (Figs. 5.27c and 5.27e). The results presented in Fig. 5.27 are representative of the corresponding regions located at $z/D \leq 0$.

$7 < L/D \leq 14$

In this flow regime, vortex shedding from the large cylinder occurs in a single cell across the entire span. As shown in Fig. 5.28a, vortices in the large cylinder wake are shed parallel to the cylinder axis, and continue to form vortex connections with small cylinder vortices similar to those found for L/D = 17. For uniform flow past a cylinder with two free ends, Inoue & Sakuragi (2008) observed a comparable flow regime for $10 < L/D < 20$.

Estimates of the shedding frequency of the three vortex shedding cells (S1-cell, L-cell, and S2-cell) were obtained based on the analysis of video record capturing over 100 L-cell shedding cycles. The S1 and S2-cell shedding frequencies were found to match the corresponding frequencies for L/D = 17 (Fig. 5.23b), while the L-cell shedding frequency decreases with decreasing L/D ratio: (i) L/D = 14, $f_L D/U = 0.193$, (ii) L/D = 10, $f_L D/U = 0.186$, and (iii) L/D = 7, $f_L D/U = 0.175$. Inoue & Sakuragi (2008) report a similar trend for cylinders with two free ends.

Changes in the vortex shedding pattern along the span can be seen in Fig. 5.28, which shows three flow visualization images for L/D = 10. The images represent typical flow patterns seen within the S1-cell (Fig. 5.28b), the S1-L cell boundary (Fig. 5.28c), and the L-cell (Fig. 5.28d). Within the transition region between the S1 and L-cell, a distorted shedding

pattern is observed (Fig. 5.28c). Vortex dislocations occur within the S1-L and S2-L cell boundaries, located within $4 \leq z/D \leq 5$ and $-4 \leq z/D \leq -5$, respectively. However, as the aspect ratio is decreased to L/D = 7, the S1-L and S2-L cell boundaries no longer remain in fixed z/D ranges, marking the onset of another flow regime.

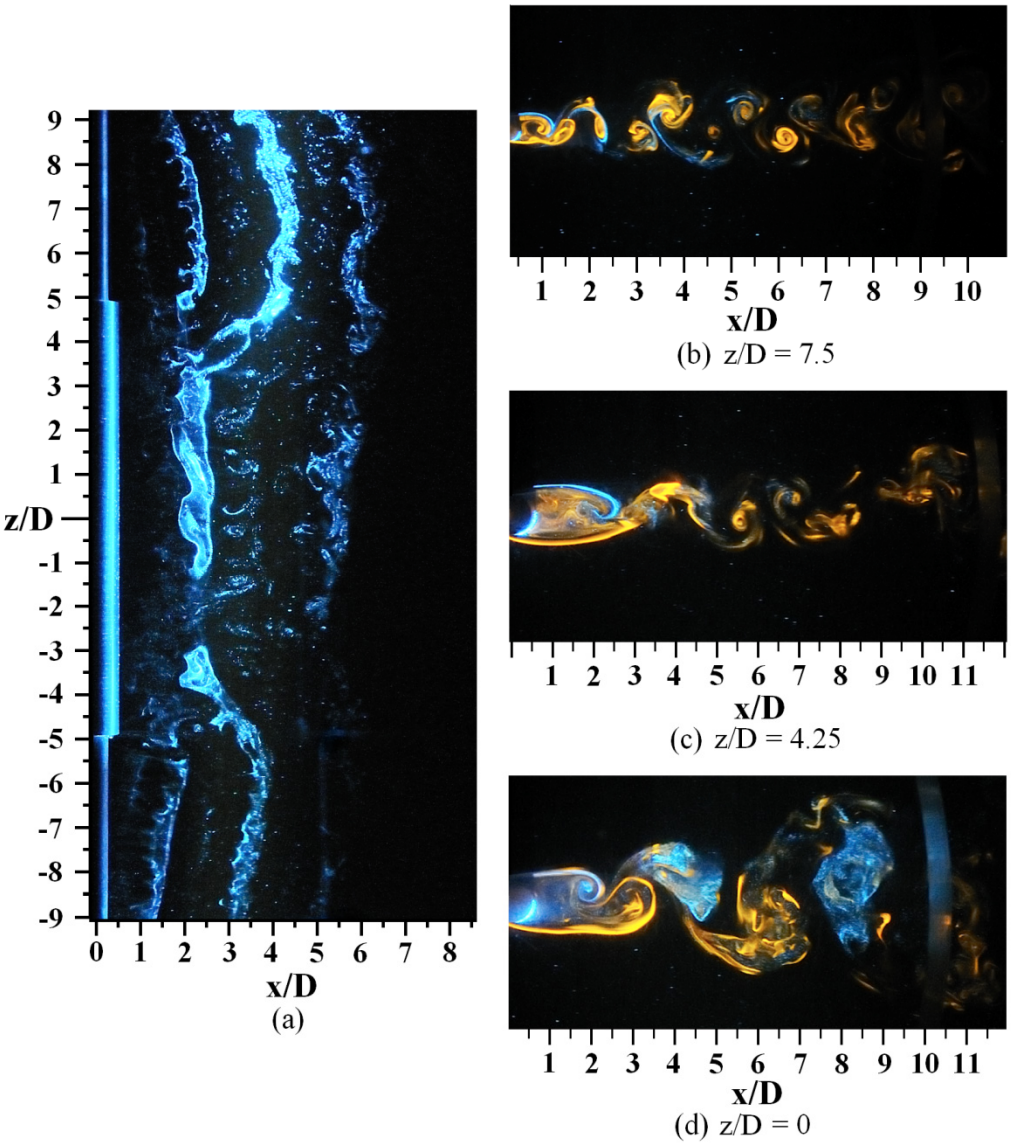

Figure 5.28 Changes in the vortex shedding pattern along the span of a dual step cylinder for L/D = 10.

2 ≤ L/D ≤ 7

In this regime, vortex shedding persists in the wakes of the small cylinders but becomes difficult to identify in the wake of the large cylinder. The S1-L and S2-L cell boundaries are deflected towards the small cylinder near the steps. As can be seen in Fig. 5.29a, vortex shedding in the large cylinder wake cannot be adequately visualized with a laser sheet positioned at y/D = 0.375, but its presence is evident in planar images (Figs. 5.29d-f). The visualization image in Fig. 5.29a was captured after the hydrogen bubble system had been activated for several S-cell shedding cycles. Changes in the vortex shedding pattern along the span of a dual step cylinder can be seen in Figs. 5.29b-f, which show flow visualization images for L/D = 5. The images represent typical flow patterns seen within the S1-cell (Fig. 5.29b), the S1-L cell boundary (Fig. 5.29c), and the L-cell (Fig. 5.29d-f). In contrast with flow regimes observed for higher L/D, Figs. 5.29d-f illustrate the intermittent shedding patterns within the L-cell. Figure 5.29d shows a planar shedding pattern similar to that observed in the wake of a uniform cylinder. Such a pattern is no longer observed in Figs. 5.29e and 5.29f, although these figures still show evidence of large scale vortices forming in the wake. Zdravkovich et al. (1989) found a similar intermittent vortex shedding behaviour in the wake of a cylinder with two free ends for $2 < L/D < 8$, which was accompanied by large variations in vortex shedding frequency (Zdravkovich et al., 1989).

In order to visualize the initial formation of L-cell vortices which can be seen in Fig. 5.29d-f, a sequence of images was captured immediately after activation of the hydrogen bubble system. The obtained images are presented in Figs. 5.30a-h. In Figs. 5.30a and 5.30b, a developing vortex in the wake of the large cylinder can be seen. In Fig. 5.30b, the vortex at $x/D \approx 2.75$ is visible in the ranges $-2 < z/D < -1$ and $1 < z/D < 2$. Since no hydrogen bubbles

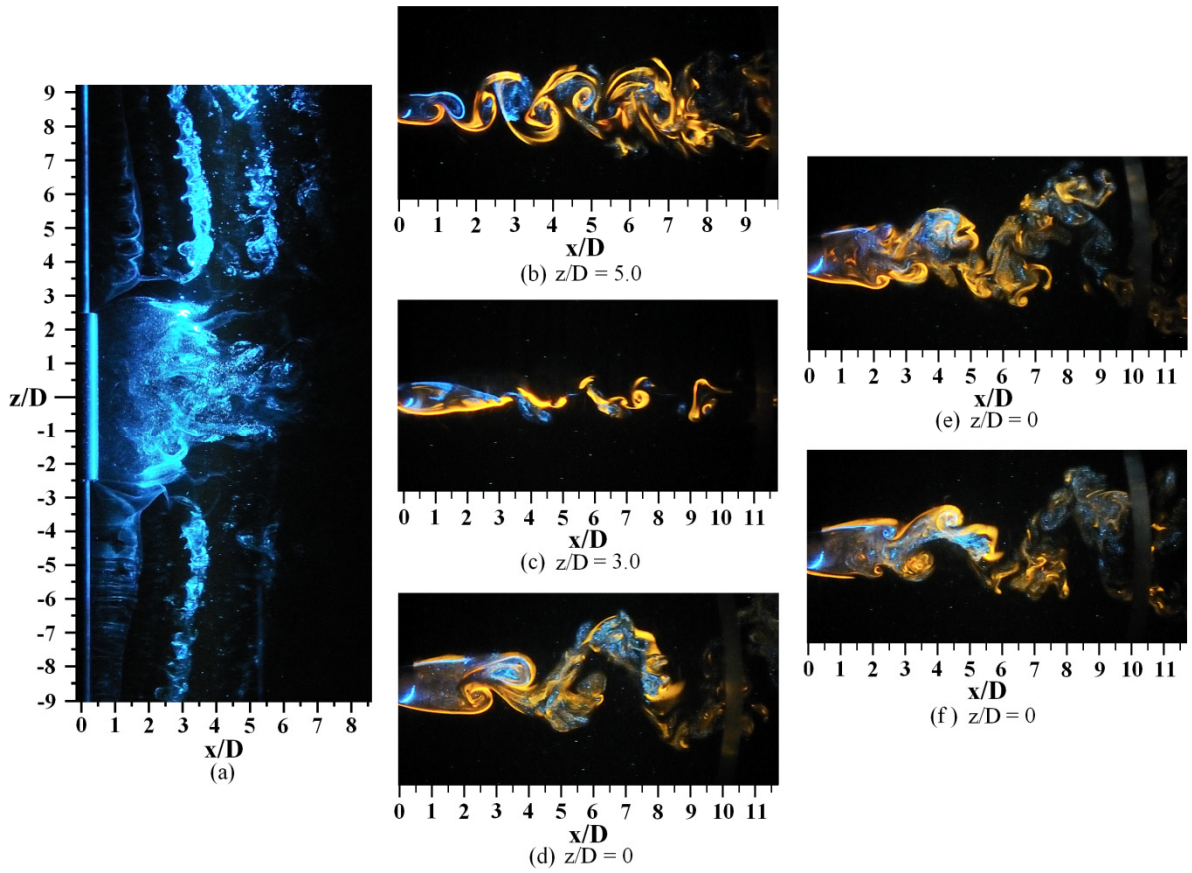

Figure 5.29 Changes in the vortex shedding pattern along the span of a dual step cylinder for L/D = 5.

appear in the range -1 < z/D < 1, it is speculated that the vortex is undergoing spanwise deformation, hence part of the vortex is out of the plane of visualization. In Fig. 5.30c, the vortex is convected downstream to x/D ≈ 3.25. Comparing Figs. 5.30b and 5.30c, it can be conjectured that the vortex is no longer oriented parallel to the cylinder axis. It is speculated that the vortex, which initially forms parallel to the cylinder axis (Figs. 5.30a and 5.30b), deforms in the near wake and becomes oriented out of the plane of visualization. Hence, visualization in Fig. 5.30c, and more clearly in 5.30d, shows the core of the same vortex labeled by white arrows in each figure. Figures 5.30e-h illustrates a similar deformation of the next vortex shed from the same side of the large cylinder. Although the accumulation of

hydrogen bubbles in the large cylinder masks the initial formation of the next vortex, Figs. 5.30g and 5.30h show the vortex core much like Figs. 5.30c and 5.30d.

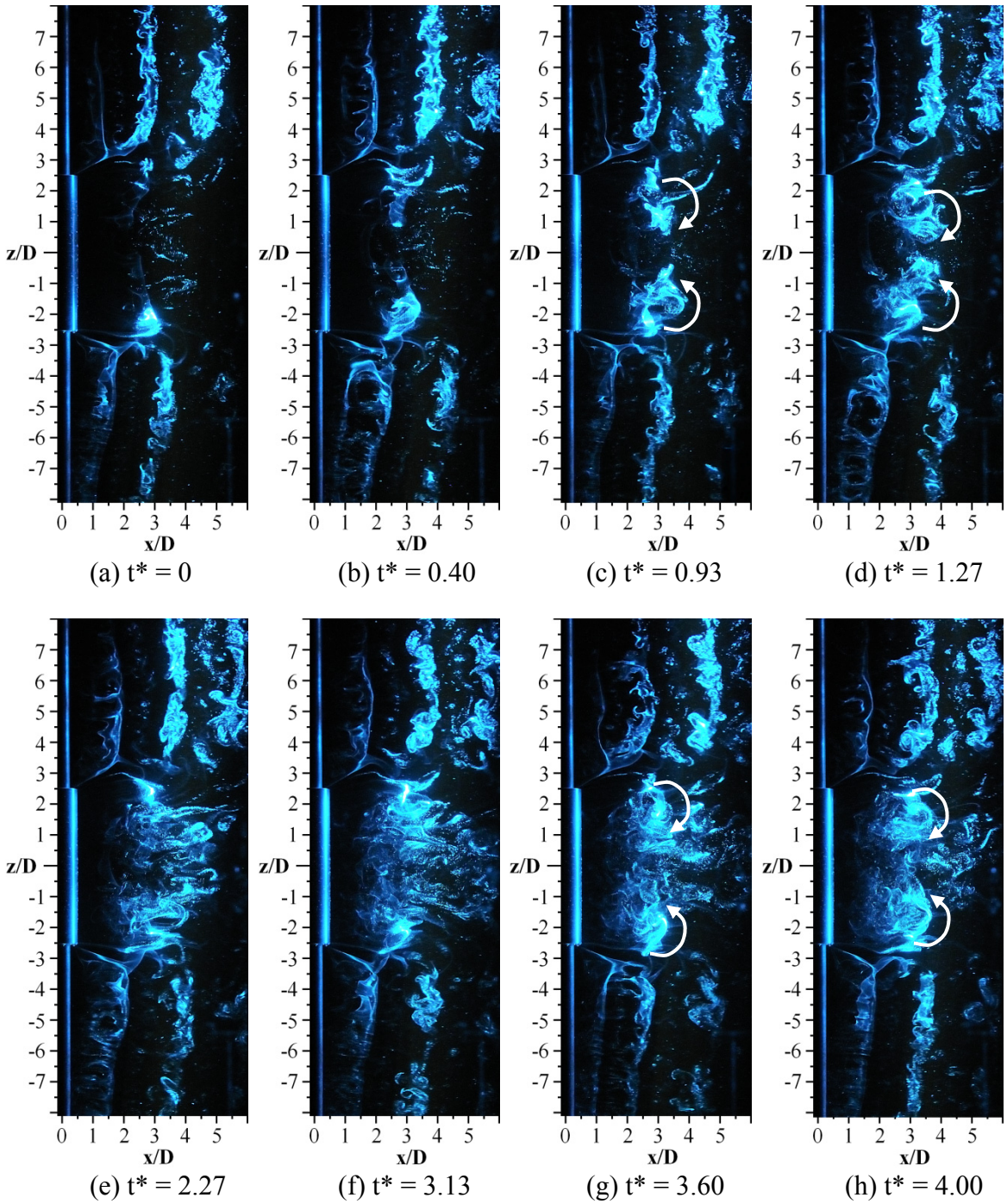

Figure 5.30 Initial vortex formation and development in the wake of a dual step cylinder for L/D = 5.

To visualize more clearly the spanwise development of large cylinder vortices (L-cell vortices) the laser sheet was repositioned to y/D = 0.75. The flow visualization image sequence shown in Figs. 5.31a-c depicts large cylinder vortex shedding. In Fig. 5.31a, a large cylinder vortex can be seen at x/D ≈ 3.0, -2.5 < z/D < 2.5. In Fig. 5.31b, the same vortex has moved downstream to x/D ≈ 4, -1.5 < z/D < 1.5. The spanwise extent of the vortex in the plane of visualization decreases with x/D, supporting the earlier speculation that the vortex undergoes three-dimensional deformation. In Fig. 5.31c, this vortex can no longer be clearly identified at its expected downstream location x/D ≈ 5. For laminar shedding from a cylinder with two free ends, similar three-dimensional deformation of the shed vortices was observed by Inoue & Sakuragi (2008) for aspect ratios less than about 10. Inoue & Sakuragi (2008) refer to this type of shedding as a hairpin shedding, as vortices attain a hairpin-like shape in the wake.

0.2 ≤ L/D ≤ 1

Figure 5.32 illustrates the flow development in this regime. As was confirmed by the analysis of video records, vortices are no longer detectable in the large cylinder wake. In Fig. 5.32a, S1 and S2-cell vortices can be seen in the wake at x/D ≈ 1 and 3. The S-cell vortices in the region surrounding the large cylinder appear to form direct connections across the wake of the large cylinder. In Fig. 5.32b, the same vortex connection between S1 and S2-cell vortices can be seen farther downstream at x/D ≈ 4. However, a dislocation occurs in Fig. 5.32c, where subsequent S-cell vortices at x/D ≈ 2.5 do not connect across the large cylinder wake. A detailed analysis of video records revealed that S1 and S2 cell vortices form vortex connections across the large cylinder wake in an alternating fashion. It can be speculated that

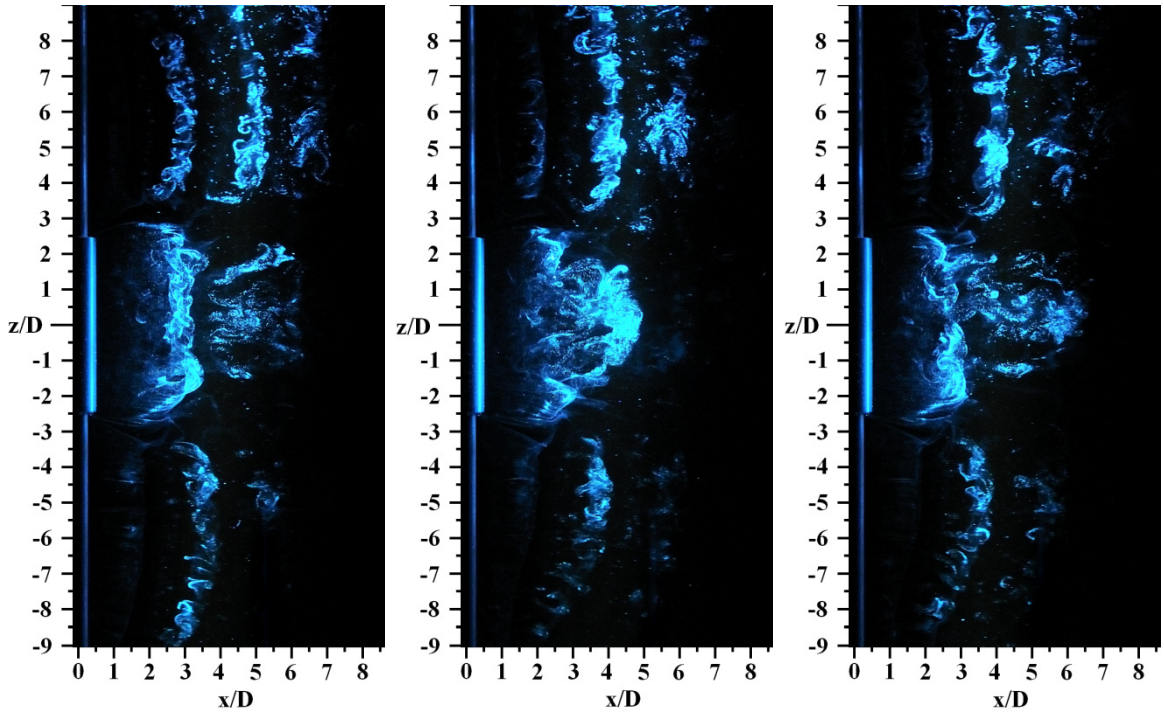

(a) t* = 0 (b) t* = 0.85 (c) t* = 1.28

Figure 5.31 Three-dimensional shedding in the wake of a dual step cylinder for L/D = 5. In contrast to other flow images, positioning the laser sheet at y/D = 0.75 allows visualizing vortex shedding in the large cylinder wake.

the observed vortex dislocations are linked to some periodic flow phenomenon. In comparison, Inoue & Sakuragi (2008) found alternate shedding of counter-rotating vortex pairs for a cylinder with two free ends at $L/D \approx 1$ and $200 \leq Re_D \leq 300$.

Changes in the vortex shedding pattern along the span of the dual step cylinder at L/D = 1 are depicted in Fig. 5.33. The images represent typical flow patterns seen within the S1 and S2-cells (Fig. 5.33b), and in the wake of the large cylinder (Fig. 5.33c). Although a shear layer roll-up can be seen in Fig. 5.33c, no clear vortex shedding pattern is visible in the near wake.

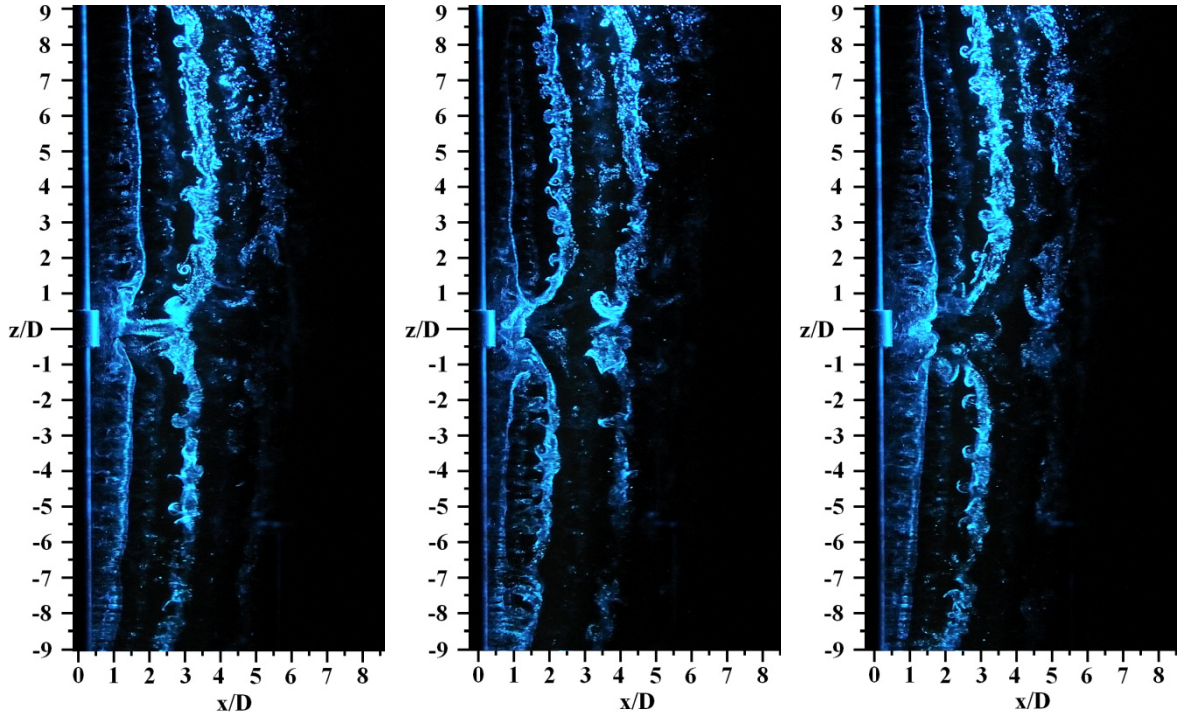

(a) t* = 0 (b) t* = 0.55 (c) t* = 1.1

Figure 5.32 Vortex shedding in the wake of a dual step cylinder for L/D = 1.

Flow Separation

The process of electrolysis in the hydrogen bubble flow visualization experiments causes small charged particles to deposit on the large cylinder surface, located about 0.2D downstream of the hydrogen bubble wire. If the hydrogen bubble system remains active for longer than about 10 minutes, a significant number of particles collect on the cylinder surface, allowing the identification of a separation line along the cylinder span. Figure 5.34a-d shows images of the large cylinders after intentionally allowing particles to collect on the cylinder surface. The results show that, in agreement with experimental observations on free end cylinders (e.g., Zdravkovich et al., 1989), flow separation is delayed near the large cylinder ends for all aspect ratios investigated. It can be seen that for L/D = 2, 3, and 5 (Figs. 5.34b-d), the majority of the separation line is uniform, which is an indication of two-

dimensional vortex shedding in this region. For L/D = 1 (Fig. 5.34a), the separation line is non-uniform across the entire large cylinder span. This supports earlier observations that vortices are no longer shed from the large cylinder for $0.2 \leq L/D \leq 1$.

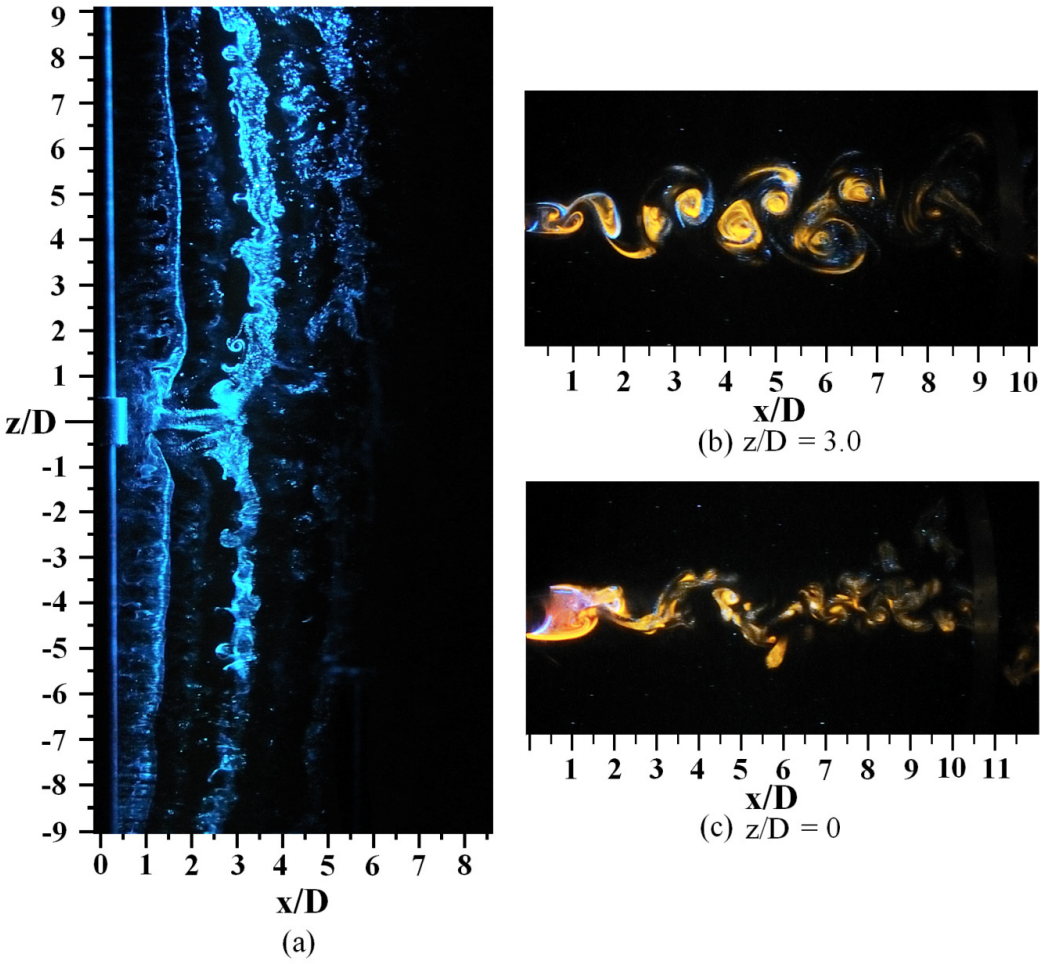

Figure 5.33 Changes in the vortex shedding pattern along the span of a dual step cylinder for L/D = 1.

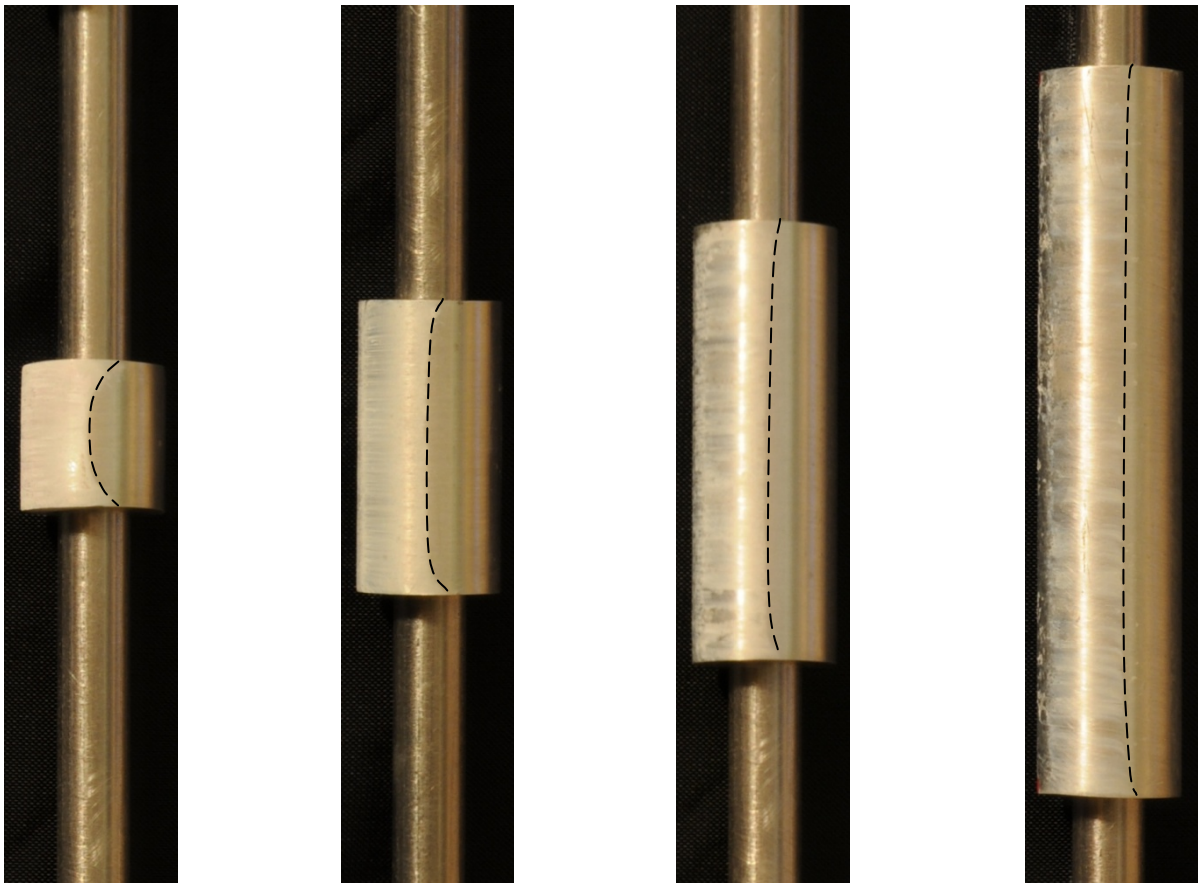

(a) L/D = 1 (b) L/D = 2 (c) L/D = 3 (d) L/D = 5

Figure 5.34 Flow separation line for: (a) L/D = 1, (b) L/D = 2, (c) L/D = 3, and (d) L/D = 5.

6 Concluding Remarks

Flow development over a single step cylinder and dual step cylinder has been investigated both experimentally and numerically. The main objective was to investigate vortex shedding occurring in the wake. The investigations were performed for Reynolds numbers of 150, 300, and 1050 and the diameter ratio of 2.

Vortex shedding in the wake of a single step cylinder

Laminar Navier-Stokes simulations were used to model the flow past a single step cylinder for Re_D = 150 and 300. Experimental flow visualization and SST-DES based computations were completed for Re_D = 1050.

Experimental and numerical results show that three distinct spanwise vortex shedding cells form in the step cylinder wake, namely, the S-cell, N-cell, and L-cell. The N-cell, which forms in a region downstream of the step on the large cylinder side, has the lowest shedding frequency of the three cells. Due to the difference in shedding frequencies of the N-cell, L-cell, and S-cell, vortex dislocations occur at the boundaries between the adjacent cells.

The laminar simulation results provide new insight into vortex dynamics in the step cylinder wake. In particular, complex vortex interactions, involving vortex dislocations and vortex splitting, occur within two regions located at the cell boundaries, referred to as transition regions, whose location and spanwise extent fluctuates with time. In a relatively narrow transition region at the N-S cell boundary, N-cell vortices split into at least two vortex filaments, with one of these filaments connecting directly with an S-cell vortex and the other connecting with a subsequent N-cell vortex. In this region, vortex dislocations occurring at the beat frequency ($f_S - f_N$) are manifested as half-loop connections between two S-cell

vortices of the opposite sign. In contrast, the transition region at the N-L cell boundary is significantly wider and its extent fluctuates substantially with time. Within this region, L-cell vortices form direct cross-boundary connections with N-cell vortices. However, as the N-cell and L-cell vortices move out of phase, a vortex dislocation occurs, during which a few consecutive L-cell and N-cell vortices connect through both cross-boundary and half-loop connections. Vortex dislocations at the N-L cell boundary occur at the beat frequency ($f_L - f_N$) and cause significant, periodic fluctuations in the spanwise extent of the N-cell at the matching frequency.

The development of spanwise vortex cells for $Re_D = 1050$ is similar to that for $Re_D = 150$ and 300. However, the formation of small-scale streamwise vortices in the large cylinder wake for $Re_D = 300$ and 1050, complicates the vortex dynamics in the step-cylinder wake. The DES results illustrate the complexity of the turbulent wake structures forming for $Re_D = 1050$. The presence of three-dimensional structures in the wake is expected to influence wake vortex shedding characteristics, and such influence should be investigated further.

Spectral analysis of velocity data has been used to estimate vortex shedding frequencies of the S-cell, N-cell, and L-cell for $Re_D = 150$ and 300, while flow visualization videos have been used to quantify shedding frequencies for $Re_D = 1050$. The ratio of the N-cell and L-cell shedding frequencies and N-cell and S-cell shedding frequencies has been documented for all the Reynolds numbers investigated. A quantitative comparison of the results obtained in the present investigation and those from previous experimental studies suggests that in general, the ratio of the N-cell and L-cell shedding frequencies, f_N/f_L, increases with increasing Reynolds number.

The numerical results for Re_D = 150 and 300 show that downwash from the step affects the N-cell vortex formation region. In particular, the observed fluctuations in the downwash velocity are linked to the cyclic variation of the N-cell size at the beat frequency ($f_L - f_N$). This supports the speculation made by Dunn and Tavoularis (2006) that the N-cell formation may be attributed to the presence of the downwash, similar to the case of a free-end cylinder. Experimental flow visualization at Re_D = 1050 has also confirmed the existence of downwash past the step and illustrated the three-dimensionality of the flow in this region.

Vortex shedding in the wake of a dual step cylinder

Vortex shedding in the wake of a dual step cylinder was investigated experimentally for Re_D = 1050 and $0.2 \leq L/D \leq 17$. The flow development in the large cylinder wake was found to depend significantly on L/D. For the cases investigated, four distinct vortex shedding regimes were identified.

For L/D = 17, the flow development near each of the two steps is similar to that found for a single step cylinder. Five distinct vortex shedding cells form in the wake: the S1-cell, the N1-cell, the L-cell, the N2-cell, and the S2-cell. The N1 and N2-cells have the lowest of the five shedding frequencies and form in a region downstream of each step change in diameter on the large cylinder side. Due to the difference in shedding frequencies between the five cells, vortex connections and dislocations take place at cell boundaries. The vortex connections are similar to those observed for a single step cylinder.

For $7 < L/D \leq 14$, vortex shedding from the large cylinder occurs in a single cell across the entire span. Vortices in the large cylinder wake are shed nearly parallel to the cylinder axis and continue to form vortex connections with small cylinder vortices, similar to the

vortex connections seen for higher aspect ratios. The shedding frequency of the L-cell in this flow regime decreases with decreasing L/D.

For $2 \leq L/D \leq 7$, vortex shedding is highly three-dimensional, as shed vortices deform in the near wake. Moreover, vortex shedding occurs intermittently in the wake of the large cylinder. It is speculated that this type of intermittency is similar to that observed by Zdravkovich et al. (1989) in the wake of a cylinder with two free ends for $2 < L/D < 8$.

For $0.2 \leq L/D \leq 1$, the results suggest that spanwise vortices are no longer shed from the large cylinder. Downstream of the large cylinder dislocations occur between the two S-cells. It is speculated that these dislocations may be linked to a quasi-periodic phenomenon taking place in the large cylinder wake.

7 Recommendations

The main objective of this research, the investigation of vortex shedding in the wake of circular cylinders with single step and dual step discontinuities in diameter, have been accomplished. Recommendations for future investigations are provided in this section.

1. In the experimental studies, velocity measurements have not been performed for the single step or dual step cylinder geometries. Such measurements can be used to provide further insight into the wake flow development.

2. Using flow visualization tools, the hydrogen bubble wire and support, as well as the dye injection probe has been shown to have no significant influence on the flow development. This conclusion should be substantiated with velocity measurements.

3. The laminar Navier-Stokes equations were used to model the flow past a single step cylinder for Re_D = 150 and 300 and D/d = 2. It is recommended that additional investigations be completed on the single step cylinder geometry in the laminar vortex shedding regime. Such studies will provide insight into the N-cell formation, and vortex shedding interactions at cell boundaries.

a) For the diameter ratio of 2, additional investigations should be completed for Re_D = 75, 200, and 400. Table 6 below summaries the flow regimes in the wake of the large and small cylinders for these Reynolds numbers.

Table 6 Recommended future investigations for flow past a single step cylinder

Re_D	D/d	Small Cylinder Flow regime	Large Cylinder Flow regime
75	2	Steady Wake	Laminar Vortex Shedding
200	2	Laminar Vortex Shedding	Mode A Vortex Shedding
400	2	Mode A Vortex Shedding	Mode B Vortex Shedding

b) For Re_D = 75, 150, 200, 300 and 400, the diameter ratio range 1.1 < D/d < 3 should be investigated. The recommended range of parameters will complement the investigations completed by Lewis and Gharib (1992) and will allow investigating the transition between the indirect and direct mode vortex shedding through several flow regimes (Table 6).

4. Flow over a single step cylinder was investigated in the turbulent shedding regime for a single Reynolds number, Re_D = 1050. To determine whether the N-cell persists indefinitely in the turbulent shedding regime, higher Reynolds numbers should be investigated experimentally. Such an experimental study can verify the observed trend of a checked increase in f_N/f_L with increasing Reynolds number.

5. Numerical modeling of the flow past a single step cylinder has provided added insight into the vortex dynamics and cellular shedding features. To the best of the author's knowledge, there have been no numerical investigations completed for flow past a dual step cylinder. It is recommended that numerical investigations on the flow past a dual step cylinder be completed for a range of aspect ratios (L/D), diameter ratios (D/d), and Reynolds numbers. The range of Reynolds numbers and diameter ratios should be similar to that recommended for the future numerical studies for a single step cylinder.

6. Flow over a dual step cylinder was investigated in the turbulent shedding regime for a single Reynolds number, $Re_D = 1050$. Additional experiments should be completed for larger Reynolds numbers to determine whether the observed transitions between vortex shedding regimes based on L/D depends solely on geometry.

References

Adrian, R.J., and Yao, C.S., (1987) "Power spectra of fluid velocities measured by laser Doppler velocimetry," Experiments in Fluids, Vol. 5, pp. 17-28.

Afgan, I., Moulinec, C., Prosser, R., and Laurence, D. (2007) "Large eddy simulation of turbulent flow for wall mounted cantilever cylinders of aspect ratio 6 and 10," International Journal of Heat and Fluid Flow, Vol. 28, pp.561-574.

Ayoub, A., and Karamecheti, K. (1982) "An experiment on the flow past a finite circular cylinder at high subcritical and supercritical Reynolds numbers," Journal of Fluid Mechanics, Vol. 118, pp. 1-26.

Balasubramanian, S., Haan Jr., F.L., Szewczyk, A.A., and Skop, R.A. (1998) "On the Existence of a Critical Shear Parameter for Cellular Vortex Shedding from Cylinders in Non-Uniform Flow," Journal of Fluids and Structures, Vol. 12, pp. 3-15.

Barth, T., and Jespersen, D. (1989) "The design and application of upwind schemes on unstructured meshes," 27th Aerospace Sciences Meeting, 9-12 Jan., Reno, Nevada.

Benedict, L.H., and Gould, R.D. (1996) "Towards better uncertainty estimates for turbulence statistics," Experiments in Fluids, Vol. 22, pp. 129-136.

Berger, E., and Willie, R. (1972) "Periodic Flow Phenomena," Annual Review of Fluid Mechanics, Vol. 4, pp. 313-340.

Breuer, M. (1998) "Large eddy simulation of the subcritical flow past a circular cylinder: numerical and modeling aspects," International Journal for Numerical Methods in Fluids, Vol. 28, pp.1281-1302.

Boutilier, M.S.H. (2009) "Assessment of the 2008 Flow Conditioning Upgrades to the University of Waterloo Adjustable Wall Wind Tunnel and Fluid Mechanics Research Laboratory Water Flume," Department of Mechanical Engineering, University of Waterloo, Ontario.

Chua, L.P., Liu, C.Y. and Chan, W.K. (1998) "Measurements of a step cylinder," International Communicatons in Heat Mass Transfer, Vol. 25, pp. 205–215.

Dunn, W., and Tavoularis, S. (2006) "Experimental studies of vortices shed from cylinders with a step-change in diameter," Journal of Fluid Mechanics, Vol. 555, pp. 409-437.

Dunn, W. (2004) "Vortex shedding from cylinders with step-changes in diameter in uniform and shear flows," PhD Thesis, Department of Mechanical Engineering, University of Ottawa, Canada.

Eisenlohr, H., and Eckelmann, H. (1989) “Vortex splitting and its consequences in the vortex street wake of cylinders at low Reynolds number,” Physics of Fluids A, Vol. 1, pp. 189-192.

Farivar, D. (1981) “Turbulent uniform flow over cylinders of finite length,” AIAA Journal, Vol. 19, pp. 275-281.

Frohlich, J., and Rodi, W. (2004) “LES of flow around a circular cylinder of finite height,” International Journal of Heat and Fluid Flow, Vol. 25, pp. 537-548.

Gaster, M. (1969) “Vortex shedding from slender cones at low Reynolds numbers,” Journal of Fluid Mechanics, Vol. 38, pp. 565-576.

Gerich, D., and Eckelmann, H. (1982) “Influence of end plates and free ends on the shedding frequency of circular cylinders,” Journal of Fluid Mechanics, Vol. 122, pp. 109-121.

Gerrard, J.H. (1978) “The Wakes of Cylindrical Bluff Bodies at low Reynolds Number,” Philosophical Transactions of the Royal Society of London, Vol. 288, pp. 351-382.

Groth, J., and Johansson, A. (1988) “Turbulence Reduction by Screens,” Journal of Fluid Mechanics, Vol. 197, pp. 139-155.

Henderson, R.D. (1995) “Details of the drag curve near the onset of vortex shedding,” Physics of Fluids, Vol. **7**, pp. 2102-2104**.**

Henderson, R.D. (1997) “Non-linear dynamics and pattern formation in turbulent wake transition,” Journal of Fluid Mechanics, Vol. 352, pp. 65-112.

Hunt, J.C.R., Wray, A.A., and Moin, P. (1988) “Eddies, stream, and convergence zones in turbulent flows,” Center for Turbulent Research Report No. CTR-S88-193.

Inoue, O., and Sakuragi, A. (2008) “Vortex shedding from a circular cylinder of finite length at low Reynolds numbers,” Physics of Fluids, Vol. 20, 033601.

Jeong, J., and Hussain, F.M. (1995) “On the identification of a vortex,” Journal of Fluid Mechanics, Vol. 285, pp. 69-94.

Kappler, M., Rodi, W., Szepessy, S., and Badran, O. (2005) “Experiments on the flow past long circular cylinders in a shear flow,” Experiments in Fluids, Vol. 38, pp. 269-284.

Karniadakis, G.E., and Triantafyllou, G.S. (1992) “Three-dimensional dynamics and transition to turbulence in the wake of bluff objects,” Journal of Fluid Mechanics, Vol. 238, pp. 1-30.

Ko, N.W.M., and Chan, A.S.K. (1984) “Pressure distributions on circular cylinders with stepwise change of diameter,” ASME Paper 84-WA/FE-13.

Ko, N.W.M., and Chan, A.S.K. (1990) “In the intermixing region behind circular cylinders with stepwise change of the diameter,” Experiments in Fluids, Vol. 9, pp. 213-221.

Ko, N.W.M., and Chan, A.S.K. (1992), “Wakes behind circular cylinders with stepwise change of diameter,” Experimental Thermal and Fluid Science, Vol. 5, pp. 182-187.

Ko, N.W.M., Leung, W.L., and Au, H. (1982) “Flow behind two coaxial circular cylinders,” ASME Journal of Fluids Engineering, Vol. 104, pp. 223-227.

Lian, Q.X., and Su, T.C., (1996) “The Application of Hydrogen Bubble Method in the Investigation of Complex Flows,” Atlas of Flow Visualization II, CRC Press, Chap. 6.

Lewis, C.G., and Gharib, M. (1992) “An exploration of the wake three dimensionalities caused by a local discontinuity in cylinder diameter,” Physics of Fluids A, Vol. 4, pp. 104-117.

Macdonald, R.W., Strom, R.K., and Slawson, P.R. (2002) “Water flume study of the enhancement of buoyant rise in pairs merging plumes,” Atmospheric Environment, Vol. 36, pp. 4603-4615.

Mair, W.A., and Stansby, P.K. (1975) “Vortex Wakes of Bluff Cylinders in Shear Flow,” Journal of Applied Mathematics, Vol. 28, pp. 519-540.

Mehta, R.D., and Bradshaw, P. (1979) “Design Rules for Small Low Speed Wind Tunnels,” Aeronautical Journal, pp. 443-449.

Menter, F. R., and Kuntz, M., “Development and application of a zonal DES turbulence model for CFX-5,” CFX-validation report, CFX-VAL17/0503.

Mittal, S. (2001) “Computation of three-dimensional flows past circular cylinder of low aspect ratio,” Physics of Fluids, Vol. 13, pp. 177-191.

Mockett, C., Perrin, R., Reimann, T., Braza, M., and Thiele, F. (2009) “Analysis of Detached-Eddy Simulation for the Flow around a Circular Cylinder with Reference to PIV Data,” IUTAM Symposium on Unsteady Separated Flows and their Control, IUTAM Bookseries, Vol. 14, pp. 417-427.

Morse, T.L., Williamson, C.H.K., (2006) “Employing controlled vibrations to predict fluid forces on a cylinder undergoing vortex-induced vibration,” Journal of Fluids and Structures, Vol. 22, pp. 877–884.

Nakamura, H., Igarashi, T. (2008) “Omnidirectional reductions in drag and fluctuating forces for a circular cylinder by attaching rings,” Journal of Wind Engineering and Industrial Aerodynamics, Vol. 96, pp. 887-899.

Narasimhamurthy, V.D., Andersson, H. I., and Pettersen, B. (2009) "Cellular vortex shedding behind a linearly tapered circular cylinder," Physics of Fluids, Vol. 21, 044106.

Nishino, T., Roberts, G.T., and Zhang, X. (2008) "Unsteady RANS and detached-eddy simulations of flow around a circular cylinder in ground effect," Journal of Fluids and Structures, Vol. 24, pp. 18-33.

Noack, B. R., Ohle F., and Eckelmann, H. (1991) "On cell formation in vortex streets," Journal of Fluid Mechanics, Vol. 227, pp. 293-308.

Norberg, C. (1987) "Effect of Reynolds Number and a Low-Intensity Freestream Turbulence on the Flow Around a Circular Cylinder," Dept. Applied Thermodynamics and Fluid Mechanics, Chalmers University of Technology.

Norberg, C. (1992) "An experimental study of the flow around cylinders joined with a step in diameter," 11th Australasian Fluid Mechanics Conference, 14-18 Dec., Hobart, Australia.

Norberg, C. (1994) "An Experimental Investigation of the Flow Around a Circular Cylinder: Influence of Aspect Ratio," Journal of Fluid Mechanics, Vol. 258, pp. 287-316.

Norberg, C. (2001) "Flow around a circular cylinder: Aspects of fluctuating lift," Journal of Fluids and Structures, Vol. 15, pp. 459-469.

Norberg, C. (2003) "Fluctuating Lift on a Circular Cylinder: Review and New Measurements," Journal of Fluids and Structures, Vol. 17, pp. 57-96.

Okamoto, T., and Takeuchi, M. (1975) "Effect of Side Walls of Wind Tunnel on Flow Around Two-Dimensional Circular Cylinder and its Wake," Bull. JSME, Vol. 18, pp. 1011-1017.

Okamoto, T., and Yagita, M. (1973) "The experimental investigation on the flow past a circular cylinder of finite length placed normal to the plane surface in a uniform stream," Bulletin JSME, Vol. 18, pp. 1011-1017.

Pattenden, R.J., Bressloff, N.W., Turnock, S.R. and Zhang, X. (2007) "Unsteady simulations of the flow around a short surface-mounted cylinder," International Journal for Numerical Methods in Fluids, Vol. 53, pp. 895-914.

Persillon, H., and Braza, M. (1998) "Physical analysis of the transition to turbulence in the wake of a circular cylinder by three-dimensional Navier-Stokes simulation," Journal of Fluid Mechanics, Vol. 365, pp. 23-88.

Piccirillo, P.S., and Van Atta, C.W. (1993) "An experimental study of vortex shedding behind linearly tapered cylinders at low Reynolds number," Journal of Fluid Mechanics, Vol. 246, pp. 163-195.

Pope, S.B. (2000) “Turbulent Flows,” Cambridge University Press, 1st Edition.

Prasad, A., and Williamson, C.H.K. (1997) “The Instability of the Shear Layer Separating from a Bluff Body,” Journal of Fluid Mechanics, Vol. 333, pp. 375-402.

Rastogi, P. K. (2000) “Photomechanics,” Topics Appl. Phys., Vol. 77, pp. 373–412.

Revell, A., Craft, T., and Laurence, D. (2008) “Turbulence Modelling of Strongly Detached Unsteady Flows: The Circular Cylinder,” Advances in Hybrid RANS-LES Modelling, NNFM 97, pp. 279-288.

Roache, P.J., “Verification and Validation in Computational Science and Engineering”, Hermosa Publishers, Albuquerque, New Mexico, 1998.

Roh, S.C., and Park, S.O. (2003) “Vortical flow over the free end surface of a finite circular cylinder mounted on a flat plate,” Experiments in Fluids, Vol. 34, pp. 63-67.

Roshko, A. (1993) “Perspectives on Bluff Body Aerodynamics”, Journal of Wind Engineering and Industrial Aerodynamics, Vol. 49, pp. 79-100.

Roshko, A. (1954) “On the development of turbulent wakes from vortex streets,” NACA Report 1191, National Advisory Committee for Aeronautics, Washington D.C.

Sakamoto, H., and Arie, M. (1983) “Vortex shedding from a rectangular prism and a circular cylinder placed vertically in a turbulent boundary layer,” Journal of Fluid Mechanics, Vol. 126, pp. 147-165.

Scheiman., J., and Brooks, J.D. (1981) “A Comparison of Experimental and Theoretical Turbulence Reduction from Screens and Honeycomb-Screen Combinations,” Journal of Aircraft, Vol. 18, pp. 638-643.

Singh, S.P., and Mittal, S. (2005) “Flow past a cylinder: shear layer instability and drag crisis,” International Journal for Numerical Methods in Fluids, Vol. 47, pp. 75-98.

Spalart, P. R. (2009) “Detached Eddy Simulation,” Annual Review of Fluid Mechanics, Vol. 41, pp. 181-202.

Srikantaiah, D.V., and Coleman, H.W. (1985) “Turbulence spectra from individual realization Laser Velocimetry data,” Experiments in Fluids, Vol. 3, pp. 35-44.

Stansby, P.K. (1974) “The effects of end plates on the base pressure coefficient of a circular cylinder,” Aeronautical Journal, Vol. 78, pp. 36-37.

Tan-Atichat, J., and Najib, H.M. (1982) “Interaction of Free-Stream Turbulence with Screens and Grids: A Balance Between Turbulence Scales,” Journal of Fluid Mechanics, Vol. 114, pp. 501-528.

Tavoularis, S. (2005) “Measurement in Fluid Mechanics,” Cambridge University Press.

Unal, M.F., and Rockwell, D. (1988) “On vortex formation from a cylinder. Part 1. The initial instability,” Journal of Fluid Mechanics, Vol. 190, pp. 491–512.

Valles, B., Andersson, H.I., and Jenssen, C.B. (2002) “Oblique vortex shedding behind tapered cylinders,” Journal of Fluids and Structures, Vol. 16, pp. 453-463.

Van Atta, C.W., and Piccirillo, P. (1990) “Topological defects in vortex streets behind tapered circular cylinders at low Reynolds numbers,” New Trends in Nonlinear Dynamics and Patterning Phenomena: The Geometry of Non Equilibrium (ed. P. Coullet and P. Huerre), pp. 243-250.

Wieselberger, C. (1921) “New data on the law of hydro- and aerodynamic resistance,” Physikalische Zeitschrift, Vol. 22 (in German), pp. 321-382.

West, G.H., and Fox, T.A. (1990) “On the use of end plates with circular cylinders,” Experiments in Fluids, Vol. 9, pp. 237-239.

Williamson, C.H.K. (1989) “Oblique and parallel modes of vortex shedding in the wake of a cylinder,” Journal of Fluid Mechanics, Vol. 206, pp. 579-627.

Williamson, C.H.K. (1992) “The natural and forced formation of spot-like ‘vortex dislocations’ in the transition of a wake,” Journal of Fluid Mechanics, Vol. 243, pp. 393-441.

Williamson, C.H.K. (1996) “Vortex Dynamics in the Cylinder Wake,” Annual Review of Fluid Mechanics, Vol. 28, pp. 477-539.

Williamson, C.H.K. (1996b) “Three-dimensional wake transition,” Journal of Fluid Mechanics, Vol. 328, pp. 345-407.

Wissink, J.G., Rodi, W. (2008) “Numerical study of the near wake of a circular cylinder,” International Journal of Heat and Fluid Flow, Vol. 29, pp. 1060-1070.

Wu, J., Sheridan, J., Hourigan, K., and Soria, J. (1996) “Shear Layer Vortices and Longitudinal Vortices in the Near Wake of a Circular Cylinder,” Experimental and Thermal Fluid Science, Vol. 12, pp. 169-174.

Xiyun, L., and Guocan, L. (2002) “A large eddy simulation of the near wake of a circular cylinder,” Acta Mechanica Sinica, Vol. 18, pp. 18-30.

Yagita, M., Kojima, Y., and Matsuzaki, K. (1984) “On vortex shedding from circular cylinder with step,” Bulletin of JSME, Vol. 27, pp. 426-431.

You, D., and Moin, P. (2006) “A dynamic global-coefficient subgrid-scale eddy viscosity model for large eddy simulation in complex geometries,” Center for Turbulence Research Annual Briefs, pp. 41-53.

Zdravkovich, M. M., Brand, V. P., Mathew, G., and Weston, A. (1989) “Flow past short circular cylinders with two free ends”, Journal of Fluid Mechanics, Vol. 203, pp. 557-575.

Zdravkovich, M.M. (1997a) “Flow Around Circular Cylinders, Vol 1: Fundamentals,” Oxford University Press, Vol.1.

Zhang, H.Q., Fey, U., Noack, B.R., Konig, M., and Eckelmann, H. (1995) “On the transition of the cylinder wake,” Physics of Fluids, Vol. **7**, pp. 779-794.

Appendix A: Flume Modifications and Free Stream Characteristics

The most recent information on the water flume construction, operation, and flow characteristics prior to the work completed for the current investigation was published by Macdonald et al. (2002). A diagram of the original design of the water flume settling chamber and flow conditioning upstream of the test section is shown in Fig. A.1. To verify the reported flow characteristics (Macdonald et al., 2002) and to design and implement improvements, LDV-based velocity measurements were conducted in the test section. The LDV measurements at each location in the test section were acquired for at least 120 s (at least 2048 samples).

Water supply

Two pipes of different diameter are used to transport water from an elevated head tank to the settling chamber of the flume (Fig. A.1). A gate valve installed on the larger pipe is used for coarse adjustments of the flow rate. The smaller pipe contains a valve for fine adjustments of the flow rate. For the purposes of this discussion, the valve on the larger pipe will be referred to as the primary valve, and the valve on the smaller pipe will be referred to as the secondary valve. The effect of the position of the secondary valve on the flow uniformity in the test section was identified through three experiments using LDV measurements in the test section. During these experiments, the original flow conditioning elements E1 and E3 remained in place, while E2 was removed (Fig. A.2). The water depth through all experiments was maintained at 0.8 m. The positions of the valves in the experiments were as follows: (a) the primary valve position was 5.75 revolutions opened, and the secondary valve position was closed (0 revolutions), (b) the primary valve position was 5.5 revolutions opened, and the secondary valve position was 2 revolutions opened, and (c)

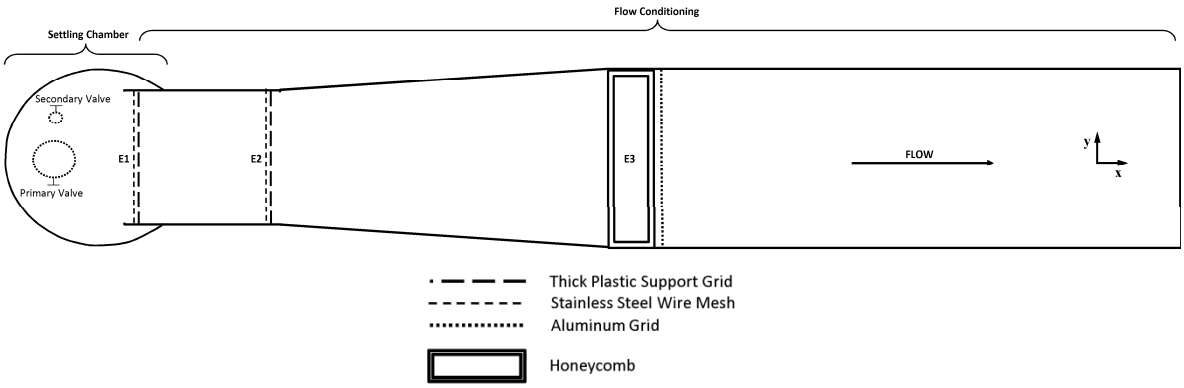

Figure A.1 Original settling chamber and flow conditioning. E1 and E2 are both a combination of a stainless steel wire mesh and plastic support grid, E3 is a combination of a honeycomb and an aluminum grid.

the primary valve position was 5.25 revolutions opened, and the secondary valve position was 4 revolutions opened. Figure A.2 shows the velocity profiles obtained at three different transverse (y) locations. With the secondary valve closed (Fig. A.2a), the velocity profiles acquired at the three transverse locations are in reasonable agreement. Comparing Figs. A.2a with A.2b and A.2c, it can be seen that opening the secondary valve has a detrimental effect on the flow uniformity in the transverse direction. Due to this, it was decided to keep the secondary valve closed through all subsequent testing.

Flow Conditioning Modifications:

It can be seen in Fig. A.2a that there is a vertical velocity gradient of 17% in the range of z from -200 to 200 [mm]. Such a velocity gradient may be rectified with flow conditioning by replacing the original flow conditioning elements and/or adding new elements at specific positions downstream of the settling chamber (Fig. A.1). The characteristics of the original flow conditioning elements are summarized in Table A.1. The objective of the settling chamber and flow conditioning modifications was to reduce the mean turbulence intensity to 1% and improve flow uniformity to within 3% in the range of z from -200 to 200 [mm].

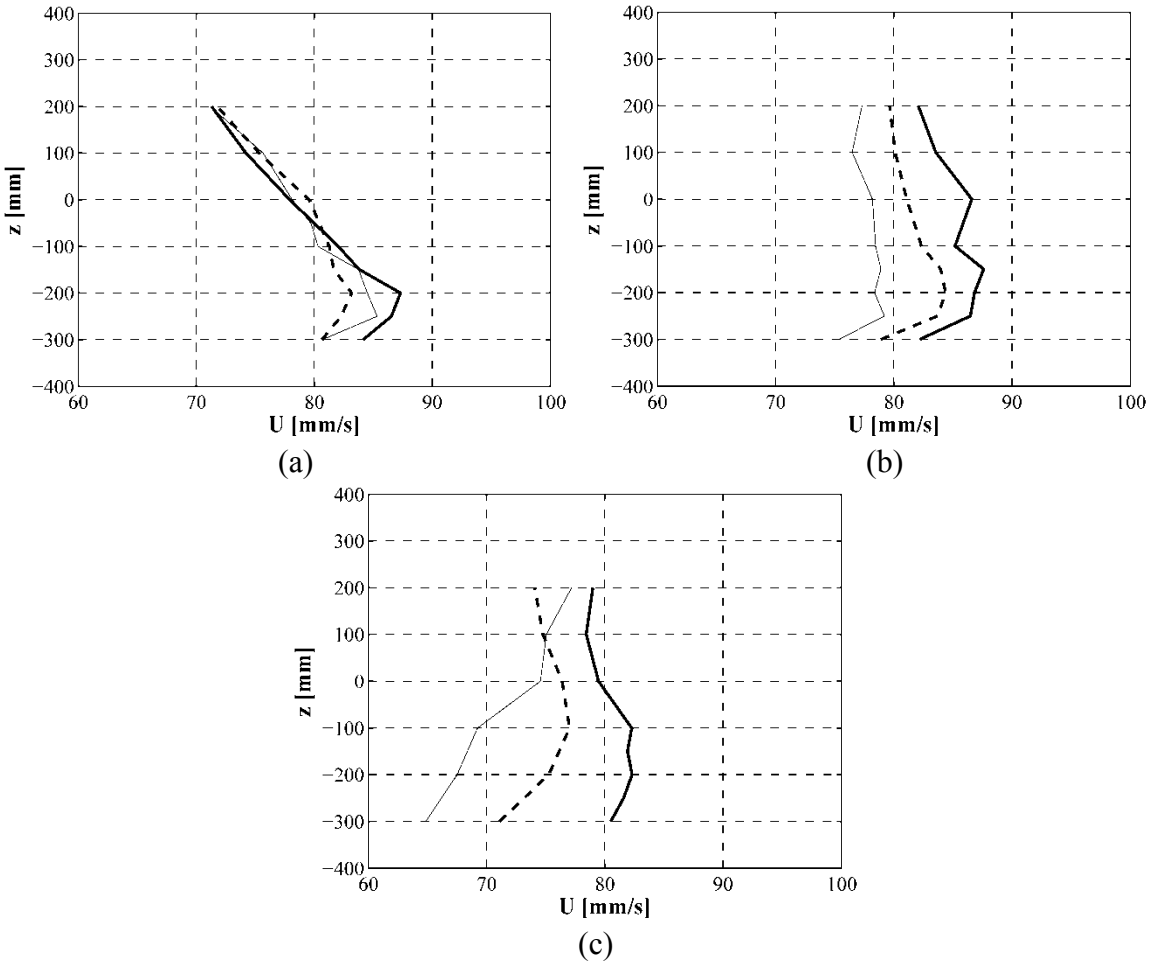

Figure A.2 Velocity profiles for three different secondary valve positions: (a) secondary valve closed, (b) secondary valve open 2 turns, and (c) secondary valve open 4 turns. —, y = −120 [mm]; - - - , y = 0 [mm]; ——, y = 120mm. The origin of the coordinate system is shown in Fig. 3.2b.

The new configuration of flow conditioning elements (Fig. A.3) and characteristics of the elements were selected based on a detailed analysis performed by Boutilier (2009). The final design also incorporated recommendations by Mehta & Bradshaw (1979), Scheiman (1981), Burley & Harrington (1982), and Loehrke & Nagib (1976). The characteristics of the flow conditioning elements in Fig. A.3 are summarized in Table A.2. Figure A.4 shows vertical velocity profiles and turbulence intensity profiles acquired in the upgraded flume. The results show that the flow uniformity is within 3% in the range of z from −200 to 250

[mm], and the corresponding mean turbulence intensity is less than 1%. Thus, the resulting free-stream characteristics meet the design objectives. Based on the results shown in Fig. A.4, a uniform flow region is defined as the flow in the range of z from -200 to 250 [mm]. All cylinder models under investigation were positioned vertically within the uniform flow region.

Table A.1 Characteristics of screens in original settling chamber.

	Spacing between Elements [mm]	Type of Flow Conditioning Element	Wire diameter, Grid thickness, or Cell size [mm]	Depth [mm]	Open Area β [%]
E1 & E2	0.1	Stainless Steel Screen	1.7-2.8	1.7	0.51
		Plastic Support Grid	40	3	0.5
E3	12.7	Honeycomb	9.5	95	-
		Aluminum Grid	12.7	12.7	0.56

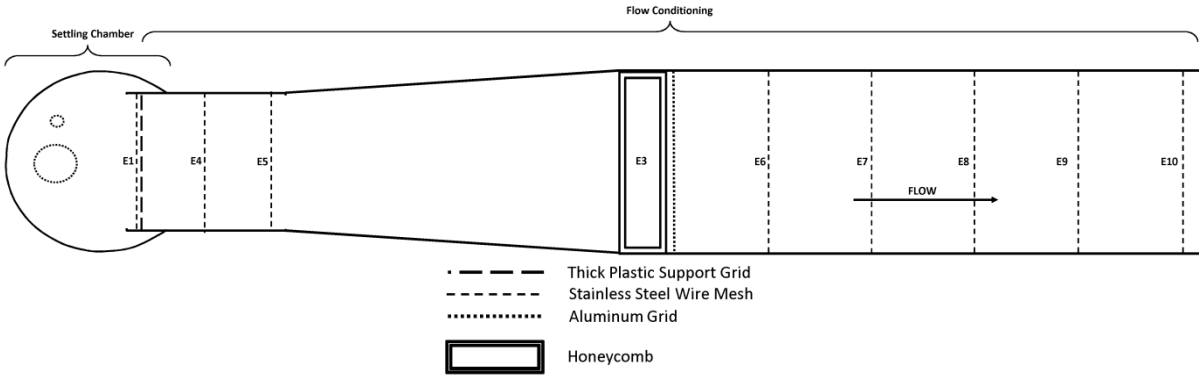

Figure A.3 New settling chamber and flow conditioning.

Table A.2 Characteristics of screens in new settling chamber.

	Spacing between Elements [mm]	Type of Flow Conditioning Element	Wire diameter, Grid thickness, or Cell size [mm]	Depth [mm]	Open Area β [%]
E1	0.1	Stainless Steel Screen	1.7-2.8	1.7	0.51
		Plastic Support Grid	40	3	0.5
E4	-	Stainless Steel Screen	0.58	0.58	0.59
E5	-	Stainless Steel Screen	0.58	0.58	0.59
E6	12.7	Honeycomb	12.7	100	-
		Aluminum Grid	12.7	12.7	0.56
E7	-	Stainless Steel Screen	0.58	0.58	0.59
E8	-	Stainless Steel Screen	0.58	0.58	0.59
E9	-	Stainless Steel Screen	0.58	0.58	0.59
E10	-	Stainless Steel Screen	0.58	0.58	0.59
E11	-	Aluminum Screen	0.48	0.48	0.64

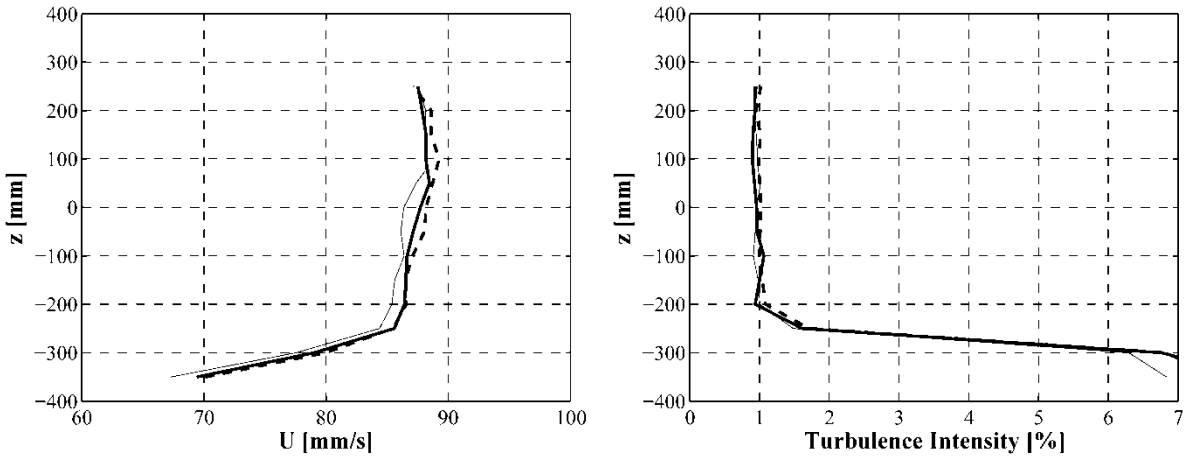

Figure A.4 Velocity profiles with all flume modifications in place: (a) mean velocity, (b) Turbulence Intensity. —, y = −120 [mm]; - - - , y = 0 [mm]; ——, y = 120mm.

Appendix B: Hydrogen bubble flow visualization

Preliminary studies aimed at optimizing hydrogen bubble flow visualization were completed with a basic hydrogen bubble wire support. Fig. B.1a shows the stainless steel wire and wire support placed about 5D upstream of a uniform cylinder of diameter D. The hydrogen bubble setup and cylinder are immersed in a uniform water flow from left to right. Hydrogen bubbles are generated on the wire by applying a DC voltage to the wire. The bubbles travel downstream, past the uniform cylinder, forming a visible white streak which can be seen in Fig. B.1a. The size of the hydrogen bubbles, and hence, their buoyancy depends on the applied voltage. Several voltages were tested with the setup shown in Fig. B.1a in order to find a voltage range for which buoyancy effects would be negligible. Flow visualization images with an applied DC voltage of 40V, 70V, and 100V are shown in Figs. B.1a-c, respectively. Figures B.1b and B.1c show hydrogen bubbles rising with downstream distance. Figure B.1a, on the other hand, shows the hydrogen bubbles traveling nearly horizontally with the water flow. Based on the results presented in Fig. B.1, buoyancy effects can be considered negligible for DC voltages less than or equal to 40 V.

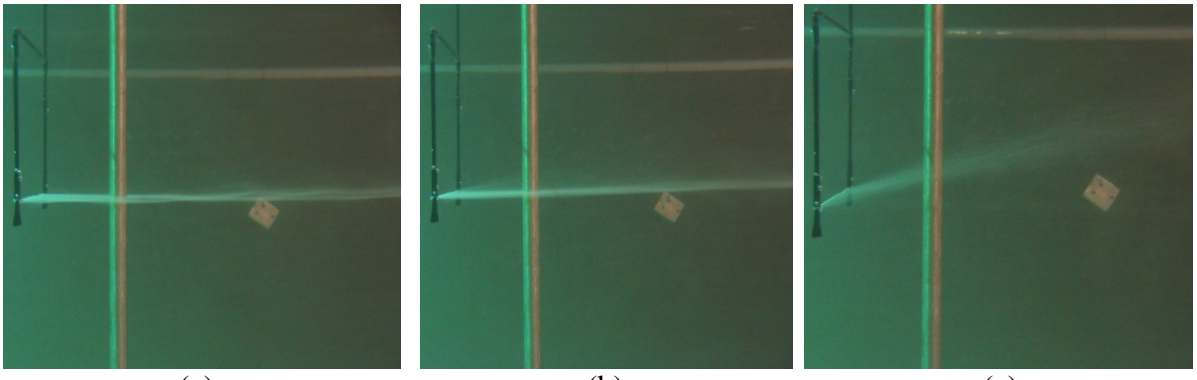

(a) (b) (c)

Figure B.1 Hydrogen bubble flow visualization for different DC voltages on a 0.09mm diameter stainless steel wire: (a) 40V, (b) 70V, (c) 100V.

Appendix C: Uncertainty

This section aims to provide an overall uncertainty estimate for the numerical simulation results and the experiments. For the experiments, repeatability tests are completed to estimate the first order, variable uncertainty (Moffat, 1988). In addition, the total uncertainty associated with all known fixed error sources is estimated. The fixed and variable errors are added using a root-sum-square combination to compute the overall uncertainty.

Numerical Uncertainty

An estimate of the uncertainty in the numerical results was completed through mesh independence studies, temporal independence studies, and direct comparison with experimental results. The uniform circular cylinder geometry was used as a test case, with numerical results for several Reynolds numbers and mesh configurations presented in Tables 3 and 4. Using the approach by Roache (1998), the bias error associated with the selected mesh and time step size was estimated to be less than 1%. Moreover, the bias error associated with the employed numerical model can be estimated by comparing the numerical and experimental results in Tables 3 and 4 for the matching Reynolds number. For the laminar Navier-Stokes and SST-DES results, the discrepancy in the reported drag coefficient and Strouhal number values is about 10%. This includes the error associated with the mesh and time step size, since a direct comparison is being made with the experimental values (assumed to be the true value).

A statistical precision error is introduced in the numerical results due to the frequency resolution in the computed velocity spectra. In particular, for a dimensionless shedding frequency of about $fD/U = 0.2$ and a frequency resolution of $\Delta fD/U \approx \pm 0.0045$, the precision

error in reported Strouhal number values is ±2.25%. This error is also embedded in the comparison with experimental results; therefore, the total uncertainty in the numerical results is about 10%.

Experimental Uncertainty

LDV-based velocity measurement: One of the most significant sources of uncertainty in LDV measurements is the velocity bias (Tavoularis, 2005). This error arises from the random data acquisition rate inherent in LDV. Higher speed particles will cross the measurement volume more frequently than slower ones, which results in a higher average velocity than the true average. An estimate of the significance of this bias for the computed mean velocities is given by the following equation (Tavoularis, 2005)

$$\frac{U}{U_T} \approx 1 + \frac{(\bar{u'})^2}{(U_T)^2} \tag{C.2}$$

where u' is the true RMS of the velocity, U_T is the true mean velocity, and U is the mean velocity measured with LDV. For the experiments conducted in this investigation, all velocity data are re-sampled at a constant frequency, which reduces the bias in the velocity measurements (Adrian and Yao, 1987). This is illustrated in Table C.1, where velocity measurements in the free stream flow, small cylinder wake, and large cylinder wake are presented. The results show that, in the free stream flow, there is no change in the mean velocity after data re-sampling, in agreement with the estimate based on Equation C.2. However, there is a significant reduction in the mean velocity in the small and large cylinder wake, in reasonable agreement with the estimates provided based on Equation C.2. Equation C.2 can be used to estimate the true value of the mean velocity for every LDV measurement location. Following this, an estimation of the bias error for each of these locations can be

Table C.1 Summary of velocity bias correction completed with data re-sampling.

LDV Measurement Location	Turbulence (%)	U (Raw Data)	U (Resampled Data)	% Reduction of U	Estimated % Reduction based on Eq. (C.2)
Free Stream Flow (x,y,z) = (0,0,50)	0.96	88.2 mm/s	88.2 mm/s	0	0.01
Small Cylinder Wake (x,y,z) = (2.5d,0.75d,50)	29.1	80.0 mm/s	76.4 mm/s	4.5	8.5
Large Cylinder Wake (2.5D, 0.75D, 50)	20.3	88.4 mm/s	85.7 mm/s	3.2	4.1

made. In particular, the bias error in the free stream flow is negligible, and the bias error in the cylinder wake is at most 4.0%.

It should be noted that there are other factors which can influence the accuracy of the velocity measurements, including the alignment of each laser beam, the variation in laser power being supplied to each beam, and the alignment of the laser probe for receiving Doppler signals (Tavoularis, 2005). These sources of error are minimized through carefully controlled alignment procedures and power optimization. Random errors in the LDV measurement may be introduced through variations in the seeding particle shape and size (e.g., Tavoularis, 2005; Rastogi, 2000). These errors may influence the measured RMS velocity and are not expected to significantly alter the mean velocity.

Repeatability: In order to estimate the random error introduced by the experimental facility and changes in experimental conditions, repeatability experiments were completed in the free stream flow. Figure C.1 shows five plots of the progressive average of velocity data as a function of sample time for LDV data obtained at (x, y, z) = (0, 0, -25). Hence, each data point plotted in Fig. C.1 is the average velocity from the time the data point was acquired. Based on the time average of 2 minute signal segments, the estimates of the mean velocity from the five measurements are within 0.2%. Computing averages over a longer period of

time did not reduce this difference between the results from the five tests. This precision error may be caused by low frequency fluctuation in the flow speed, and other factors. Day-to-day repeatability experiments were conducted to estimate the combined effect of the precision error discussed above, and the precision error introduced through variation in ambient and experimental conditions between different testing days.

Based on data acquired on five different days at the same location, (x,y,z) = (0, 0, -25), the average free stream velocity varied by less than 0.4%. For wake velocity measurements this small variation is neglected, being an order of magnitude lower than the bias error.

Statistical precision error: The statistical precision error in the velocity measurement is estimated with the BSAFlow software by Dantec Dynamics. In addition to acquiring all LDV data, this software completes an estimation of the 95% confidence limit of the mean velocity using the equation provided below from Benedict and Gould (1996).

$$MeanConf = 1.96 \times \sqrt{\frac{\overline{u'^2}}{N}} \tag{C.3}$$

For the velocity data used for Fig. C.1, the mean velocity has a 95% confidence level that is less than 0.2% of the computed mean. For all LDV measurements completed in the free stream flow, this confidence level was always maintained.

The total uncertainty in the reported mean velocity, calculated based on a root-sum-square combination of all fixed and variable error sources, is about 4.0% in the wake and 0.45% in the free stream.

The Stouhal number (St) and Reynolds number (Re_D): Uncertainty in the velocity measurement discussed previously directly influences the estimated Strouhal number and the Reynolds number. There are a few additional sources of error which do not influence the

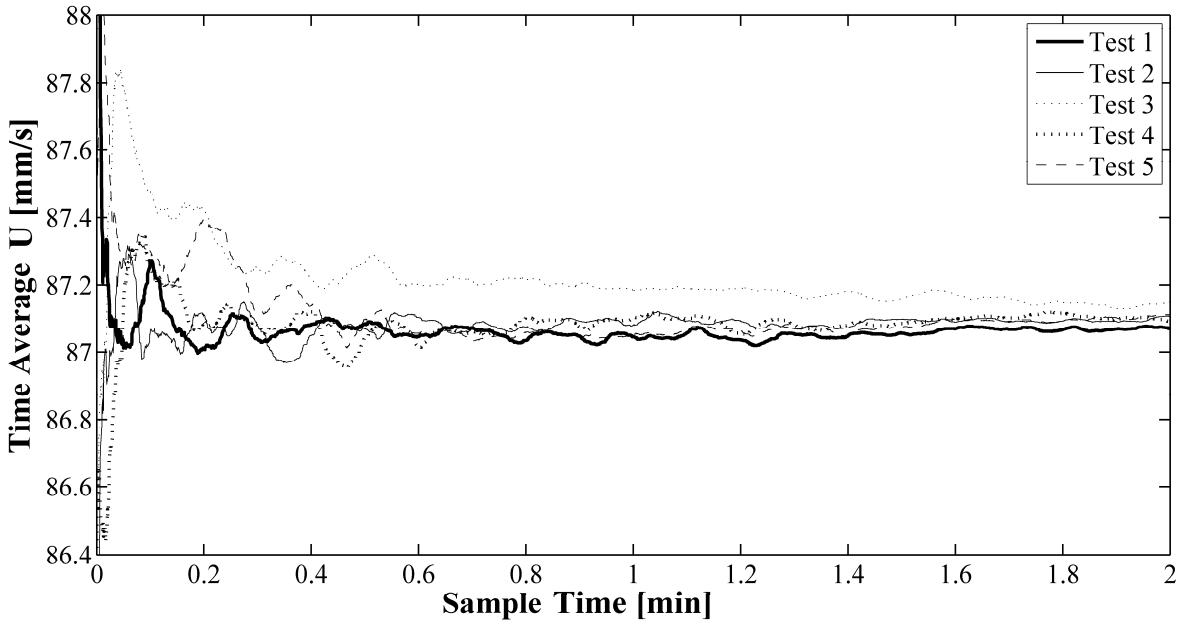

Figure C.1 Progressive average of the streamwise velocity component in the free stream flow.

velocity measurement, but can influence the estimated Reynolds number of the flow, and the Strouhal number.

The velocity over the full cross-sectional area of the test section is not uniform. In particular, there is a gradual increase in velocity with z. All of the reported Reynolds and Strouhal number values for the cylinders used in the experiments are based on the mean free-stream velocity at (x,y,z) = (0,0,0). Thus, the local Reynolds number and the Strouhal number change along the model span by ±1.5% due to the velocity gradient in the z direction.

For experimental tests conducted on different days, the temperature of the water in the flume was recorded. The temperature variations were within ±0.5 degrees Fahrenheit. This results in an uncertainty of ±0.75% in the Reynolds number.

The cylinder models were verified to be mounted vertically to within about 0.4° using a laser mounted to a 3-axis traverse. This model angle does not introduce a significant

uncertainty in the Reynolds number or Strouhal number in comparison to the other sources of uncertainty discussed previously.

Analysis of flow visualization videos was used to estimate the Strouhal number in the wake of uniform cylinders, single step cylinders, and dual step cylinders. To complete these estimations, videos were recorded for over 3 minutes, resulting in the total number of shed vortices on one side of the wake being in the range of 250 to 500. To validate this method of determining the Strouhal number, velocity measurements were acquired in the wake of uniform circular cylinders for $Re_D = 525$ and $Re_D = 1050$. Velocity data were obtained at 7 spanwise positions corresponding to z/D = -15, -10, -5, 0, 5, 10, and 15, and y/D = 0.75. The Strouhal numbers, determined based on the spectral analysis of velocity measurements and those obtained from the analysis of video records are shown in Table C.2.

It should be noted that the velocity measurements at z/D = 15 and -15 are within the end cells located near the cylinder boundaries. Since flow visualizations estimates of the Strouhal number within the end cells are likely affected by the hydrogen bubble wire supports, these estimates are not presented. The results obtained from video records match the results based on the spectral analysis in the z/D range of -10 to 10, with minor discrepancies being within the frequency resolution of the velocity spectra. For a dimensionless shedding frequency of $fD/U \approx 0.2$, and a frequency resolution of $\Delta fD/U \approx \pm 0.0025$, the statistical precision error in the Strouhal number is ±1.25%. Consistent with the increase in free stream velocity, the results in Table C.2 show that the Strouhal number increases slightly with z.

The total uncertainty in the Reynolds number and the Strouhal number is ±1.75%, and ±2.0%, respectively (Table C.3).

Table C.2 Variation of vortex shedding frequency along the span of a uniform cylinder for Re_D = 525 and 1050.

z/D	Estimates from Videos (fD/U)		Dominant spectral peak (fD/U)	
	Re_D = 525	Re_D = 1050	Re_D = 525	Re_D = 1050
15	-	-	0.178	0.197
10	0.198	0.203	0.201	0.201
5	0.198	0.203	0.199	0.203
0	0.198	0.203	0.199	0.203
-5	0.198	0.203	0.197	0.201
-10	0.196	0.201	0.195	0.201
-15	0.174	0.193	0.170	0.190

Table C.3 Total uncertainty in the free stream velocity, Reynolds number, and Strouhal number.

Total Uncertainty		
Mean Velocity, U	Reynolds Number, Re_D	Strouhal Number, St
±0.23%	±2.0%	±1.75%

Appendix D: Wake and Free stream velocity measurements

Free Stream and Wake characteristics

Figure D.1a shows a segment of the free stream velocity signal for the location (x, y, z) = (0, 0, 0). Low frequency fluctuations can be seen in the raw velocity signal for t < 15[s]. These fluctuations are speculated to be due to surface wave effects. A velocity spectrum of the signal is plotted in Fig. D.2a. Broad peaks in the spectrum can be seen at dimensionless fD/U = 0.017, 0.030, 0.064, and 0.090. It is of interest to determine if these fluctuations influence the vortex shedding in the wake of the investigated cylindrical geometries. Figure D.1b and D.1c show segments of a velocity signal acquired in the wake of a uniform circular cylinder at Re_D = 1050, and Re_D = 525, respectively. The amplitude of the fluctuations in the velocity signals in Figs. D.1b and D.1c is an order of magnitude larger than the amplitude of the low frequency fluctuations visible in Fig. D.1a. In addition, corresponding wake velocity spectra plotted in Figs. D.2b and D.2c show no considerable peaks at low frequencies. Hence, it is concluded that the low frequency free stream velocity fluctuations do not have a significant effect on the vortex shedding.

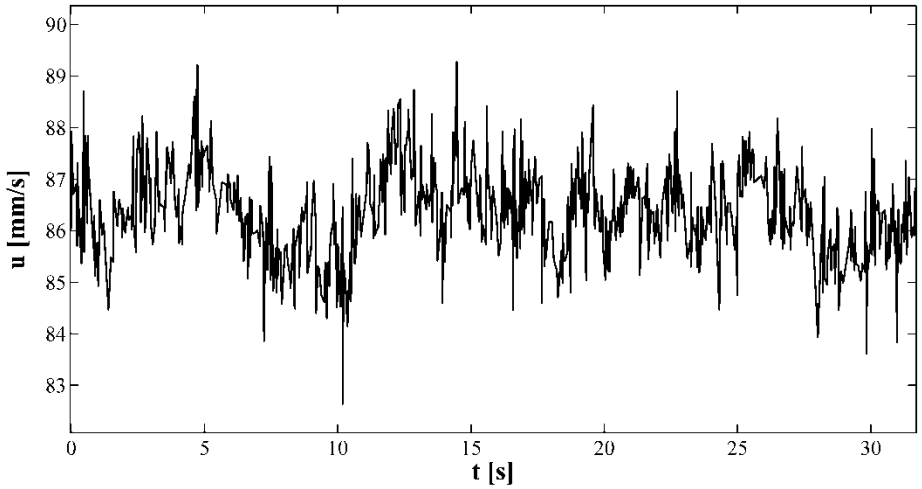

(a)

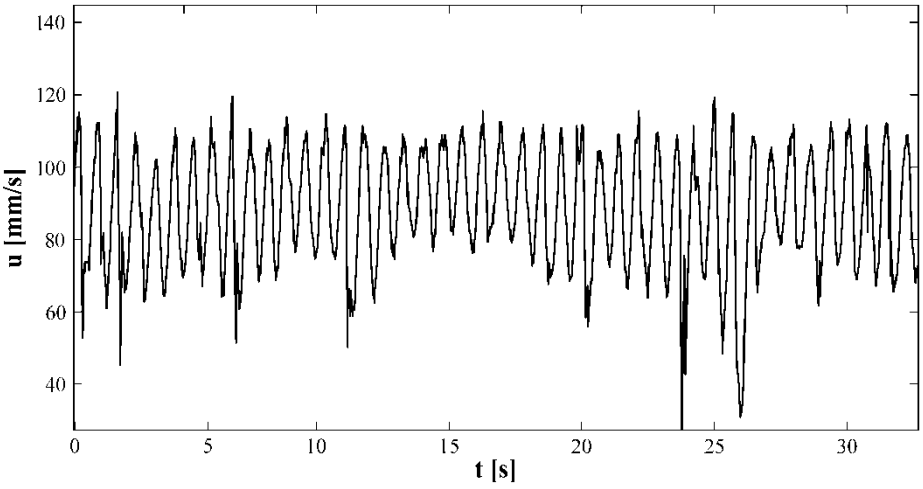

(b)

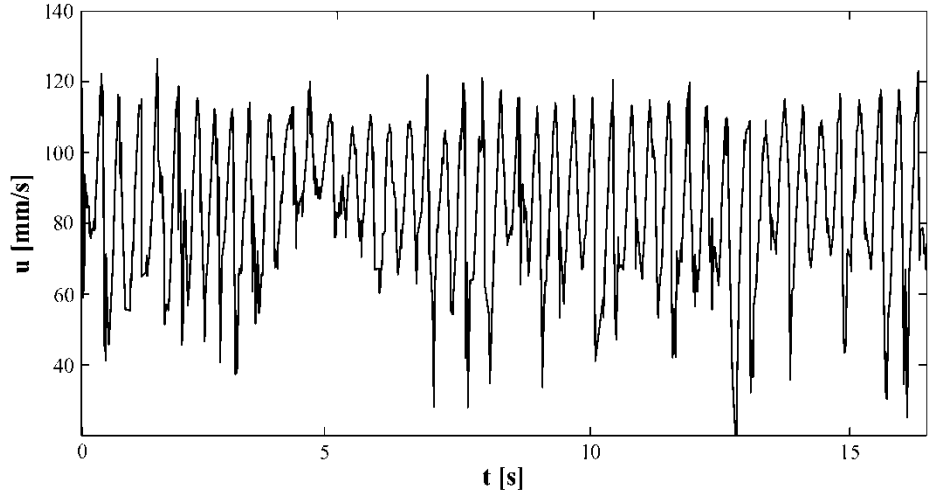

(c)

Figure D.1 Raw velocity signals: (a) free stream velocity, (b) wake velocity at Re_D = 1050, (c) wake velocity at Re_D = 525.

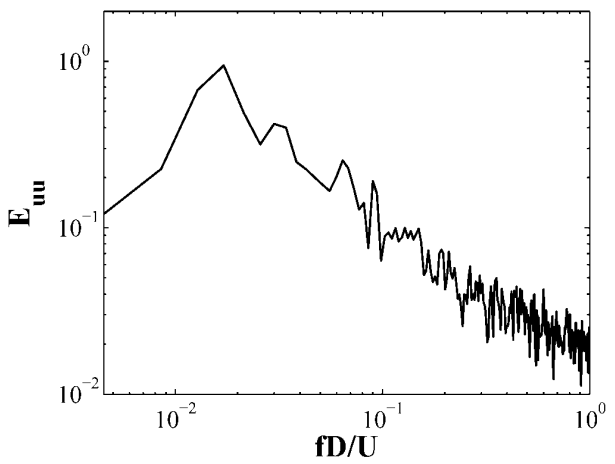

(a)

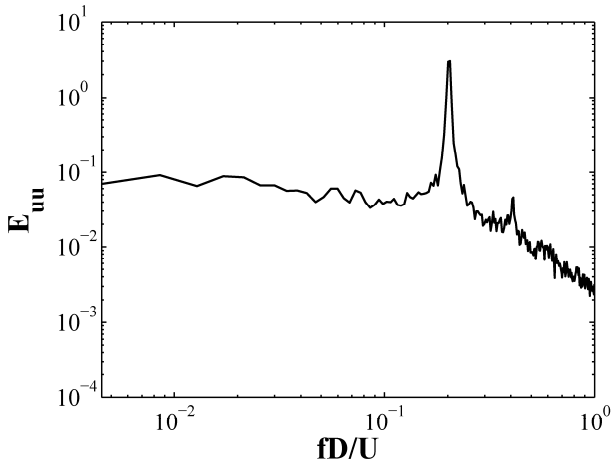

(b)

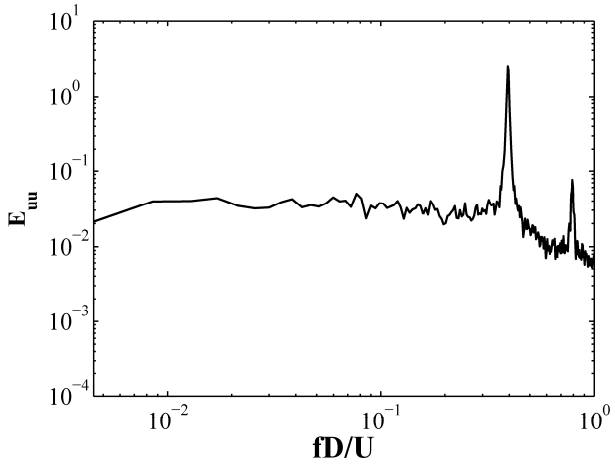

(c)

Figure D.2 Free stream and wake velocity spectra: (a) free stream spectrum, (b) spectrum in the cylinder wake for Re_D = 1050, (c) spectrum in the cylinder wake for Re_D = 525.

RMS profiles

RMS velocity profiles were obtained in the wake of the large (diameter D) and small (diameter d) uniform cylinders and are shown in Fig. D.3. The dashed vertical lines in the Figs. D.3a and D.3b, located at y/D = -0.75 and y/d = -0.75, respectively, show the location where velocity measurements were taken for spectral analysis. It should be noted that this location matches that used for spectral analysis of velocity data in the numerical simulations.

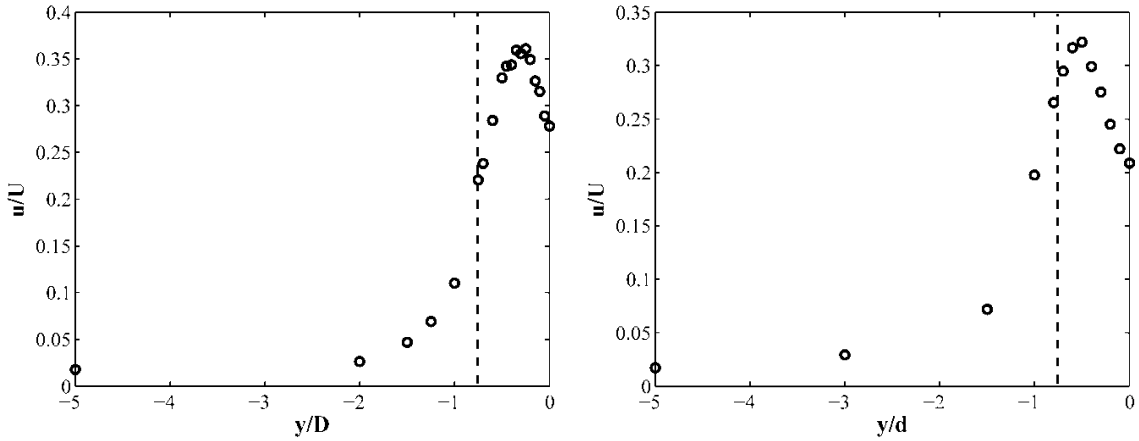

(a) $Re_D = 1050$ (b) $Re_d = 525$

Figure D.3 RMS velocity profiles for half of the wake of a uniform circular cylinder. (a) $Re_D = 1050$, (b) $Re_d = 525$. Each profiles was taken 2.5 diameters downstream of the cylinder, at z/D = 0. - - - measurement location for velocity spectra.

Appendix E: Comparison of Laminar and URANS results on the flow development past a single step cylinder

Numerical studies conducted here pertain to Re_D = 150 and 300, matching conditions investigated by Dunn and Tavoularis (2006). The work by Dunn & Tavoularis (2006) forms the main basis for much of the numerical studies completed for the step cylinder configuration in the present investigation. Their work has provided unique insight into vortex dynamics supported by flow visualizations and quantitative velocity measurements. However, in their study, the analysis of wake vortex shedding and vortex interactions is carried out based primarily on the flow visualization results pertaining to Re_D = 150. This corresponds to the laminar vortex shedding regime in the wakes of both the small and the large cylinders forming the step cylinder.

Based on the results available for uniform cylinders, Re_D = 300 corresponds to the transition vortex shedding regime in the wake of the large cylinder and laminar shedding in the wake of the small cylinder. It is known that for about $200 < Re_D < 1000$ cylinder wake undergoes transition to turbulence (e.g., Williamson, 1996; and Zdravkovich, 1997) and the transition "point" moves upstream to the near wake as the Reynolds number increases. However, there does not seem to be a general agreement among researchers so as to the critical Reynolds number for which transition reaches the vortex formation region. Considering a possibility that transition to turbulence may be occurring close to the vortex formation region for Re_D = 300, URANS as well as laminar Navier-Stokes equations were employed to model the flow over a step cylinder. URANS inherently does not model transition and does not resolve small scale streamwise wake vortices expected to form in the wake of the large cylinder for Re_D = 300. However, this method is expected to be a

reasonable model for the dynamics of the large scale spanwise vortices in the case of transition occurring within the vortex formation region. The URANS results shown in Fig. F.1 below illustrate that measurable Reynolds stresses in the computational domain occur only in the wake of the large cylinder, with the ratios of eddy viscosity and molecular viscosity being similar to those observed in numerical simulations on uniform cylinders at higher Reynolds numbers (e.g., You & Moin, 2006).

A comparative analysis of the URANS and laminar Navier-Stokes results showed marginal differences as far as the interactions of the large scale spanwise vortices in the identified vortex cells are concerned. Specifically, as depicted Fig. F.2, both types of simulations resolved the main three spanwise shedding cells and the interactions between the large scale vortices within the cells. The main difference is the small-scale streamwise structures being resolved in laminar Navier-Stokes results, which act to reduce the circulation of the spanwise vortices and, hence, lower the strength of vortex connections. However, within numerical uncertainty, the two sets of results showed no deviation between the corresponding frequencies of the spanwise cells as well as their spanwise distributions (Fig. F.3).

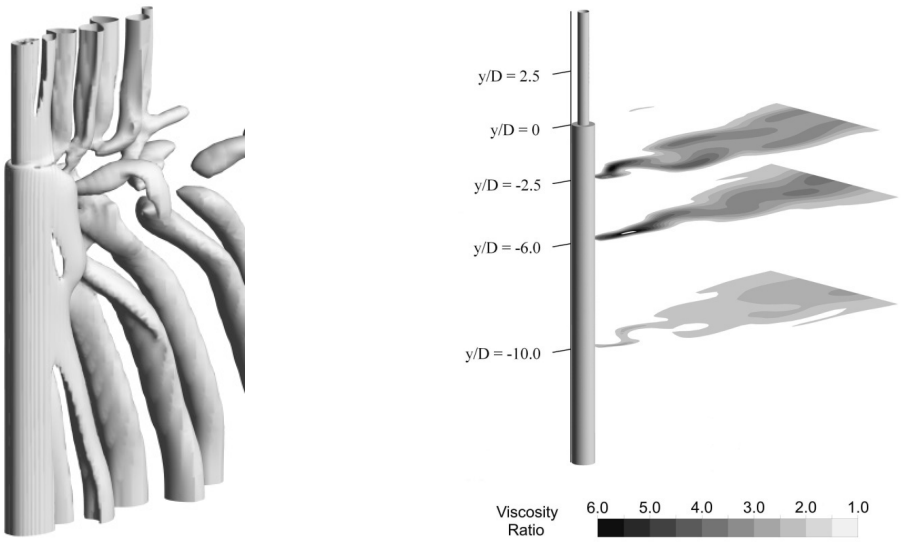

(a) (b)

Figure E.1 URANS-based results for Re_D = 300 and D/d = 2: (a) isosurfaces of Q ≈ $2x10^{-3}$, and (b) ratio of eddy viscosity to molecular viscosity at five planes along the span of the step cylinder. Note that the results show no significant Reynolds stresses in the wake of the small cylinder, as would be expected for the laminar shedding regime.

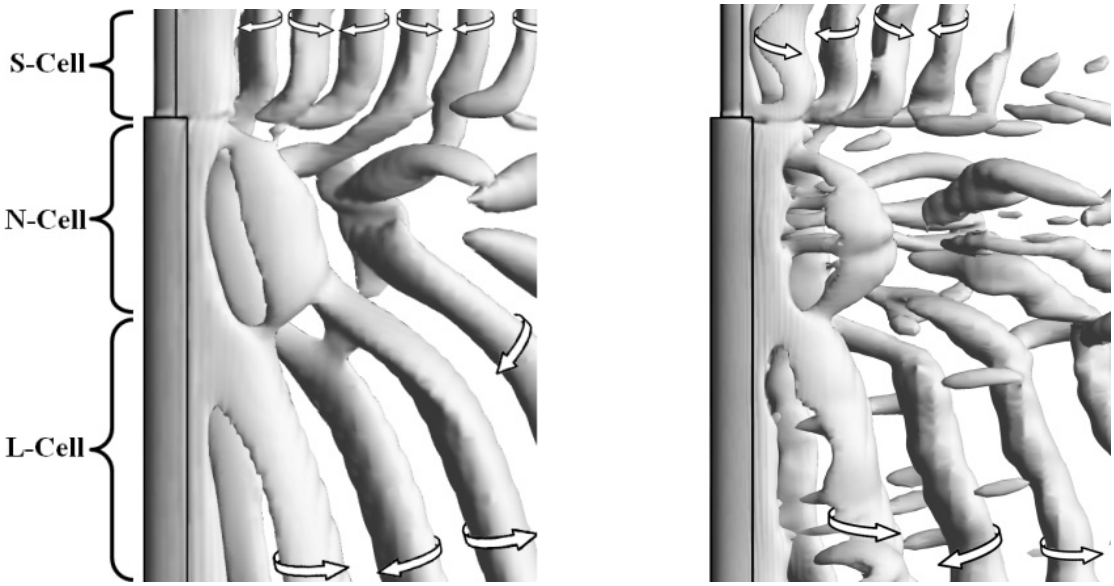

(a) URANS (b) laminar N-S

Figure E.2 Vortex shedding in the wake of a step cylinder for Re_D = 300 and D/d = 2 visualised using isosurfaces of Q ≈ $2x10^{-3}$: (a) URANS results (b) laminar Navier-Stokes results.

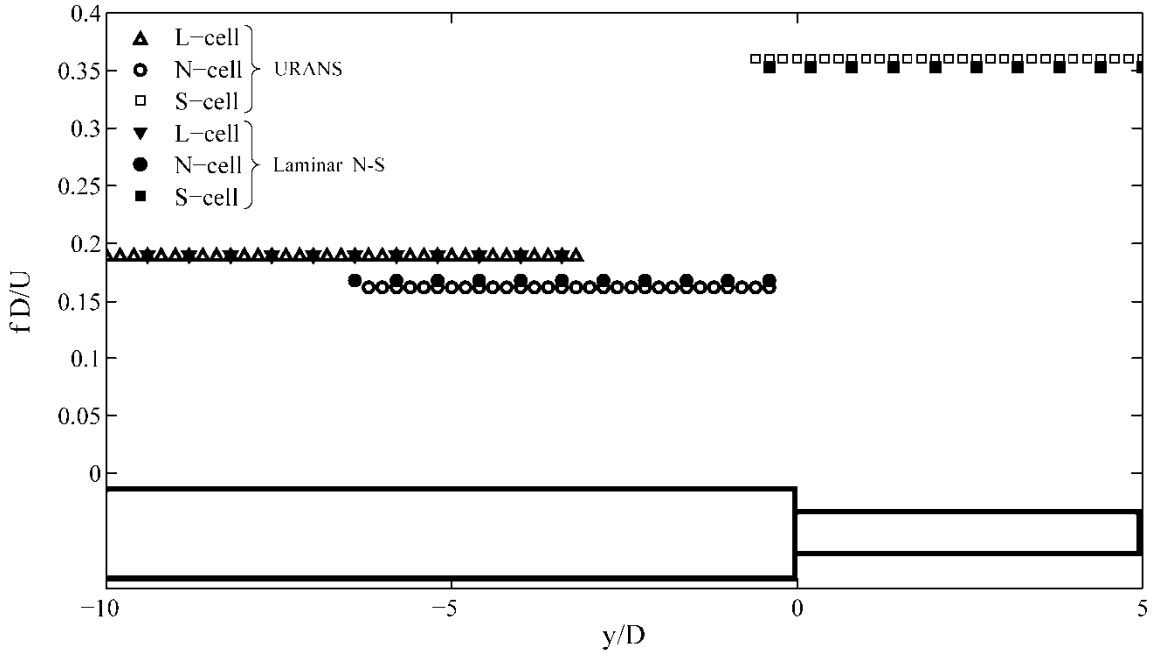

Figure E.3 Variation of dimensionless vortex shedding frequency across the span of a step cylinder for $Re_D = 300$ and D/d = 2.